

THESIS FOR THE DEGREE OF DOCTOR OF PHILOSOPHY

Slow propagation line-based superconducting
devices for quantum technology

Astghik Adamyanyan



CHALMERS

Department of Microtechnology and Nanoscience-MC2

CHALMERS UNIVERSITY OF TECHNOLOGY

Göteborg, Sweden 2016

Slow propagation line-based superconducting devices for quantum technology

Astghik Adamyan

ISBN 978-91-7597-413-2

©Astghik Adamyan, 2016

Doktorsavhandlingar vid Chalmers tekniska högskola

Ny serie nr 4094

ISSN 0346-718X

Chalmers University of Technology

Department of Microtechnology and Nanoscience, MC2

Quantum Device Physics Laboratory

Experimental Mesoscopic Physics Group

SE-412 96 Göteborg, Sweden

Telephone: +46 31 772 1000

ISSN 1652-0769

Technical Report MC2-343

Cover: Scanning Electron Microscope image of a fractal slow propagation line.

Chalmers Reproservice

Göteborg, Sweden 2016

Abstract

In the field of circuit quantum electrodynamics (c-QED), the coherent interaction of two-level systems (TLSs) with photons, confined in a superconducting microwave resonator, opens up new possibilities for quantum computing experiments.

This thesis contributes to the expansion of c-QED tool-box with slow propagation line-based solutions for ubiquitous techniques, such as cryogenic Near Field Scanning Microwave Microscopy (NSMM), Electron Spin Resonance (ESR) spectroscopy and Traveling Wave Parametric Amplifier (TWPA). For NSMM, novel compact superconducting fractal resonators have been developed to be directly integrated on a scanning probe. We report NSMM operation based on a microwave high-Q resonator populated with less than 10^3 photons and demonstrate a capacitive sensitivity of $0.38 \text{ aF}/\sqrt{\text{Hz}}$.

The unique properties and the design flexibility of fractal resonators also boost their resiliency to strong magnetic fields for ESR studies. The reported high Q-factors above 10^5 in a magnetic field up to 0.4 T translate into ESR sensitivity of $5 \cdot 10^5 \text{ spins}/\sqrt{\text{Hz}}$.

Furthermore, we demonstrate the operation of a practical TWPA based on a slow propagation fractal line. We achieve per unit length gain of $> 0.5 \text{ dB/cm}$ and total gain of $\sim 6 \text{ dB}$ for a 10 cm long line. Due to a radically shortened line, the amplifier is less vulnerable to fabrication defects. Moreover, due to a successful impedance matching between the amplifier line and in/out terminals, the obtained gain vs frequency characteristic has only moderate ripples. To mitigate a common TWPA problem of coupling to parasitic ground plane resonances, we deploy a novel multilayer fabrication technology, which combines high and low kinetic inductance (KI) elements.

Finally, we present an alternative implementation of a slow propagation line: a microstrip line with a thin film Atomic Layer Deposition (ALD) Al_2O_3 oxide. The resonator, based on a segment of a microstrip line, has a Q-factor on the order of 10^4 at single photon powers, reaching up to 10^5 at higher powers. As an additional functionality, we incorporate dc current control over KI so that the resonance frequency is tuned by 62 MHz range, which corresponds to a KI-related nonlinearity of 3%.

Keywords: near field scanning microwave microscopy, electron spin resonance, parametric amplifier, superconducting transmission line, tunable microstrip resonator

Dedicated to Anahit Yeritsyan

List of Publications

This thesis is based on the following papers:

I: A near-field scanning microwave microscope based on a superconducting resonator for low power measurements

S. E. de Graaf, A. V. Danilov, **A. Adamyan**, S. E. Kubatkin
Review of Scientific Instruments, 84, 023706, (2013).

II: Magnetic field resilient superconducting fractal resonators for coupling to free spins

S. E. de Graaf, A. V. Danilov, **A. Adamyan**, T. Bauch, and S. E. Kubatkin
Journal of Applied Physics, 112, 123905, (2012).

III: Kinetic inductance as a microwave circuit design variable by multilayer fabrication

A. A. Adamyan, S. E. de Graaf, S. E. Kubatkin and A. V. Danilov
Superconductor Science and Technology, 28, 085007, (2015).

IV: Superconducting microwave parametric amplifier based on a quasi-fractal slow propagation line

A. A. Adamyan, S. E. de Graaf, S. E. Kubatkin and A. V. Danilov
Journal of Applied Physics, 119, 083901, (2016).

V: Tunable superconducting microstrip resonators

A. A. Adamyan, S. E. Kubatkin and A. V. Danilov
Applied Physics Letters, 108, 172601, (2016).

List of Publications

Other publications not covered in this thesis:

VI: Charge Qubit Coupled to an Intense Microwave Electromagnetic Field in a Superconducting Nb Device: Evidence for Photon-Assisted Quasiparticle Tunneling

S. E. de Graaf, J. Leppäkangas, **A. Adamyman**, A. V. Danilov, T. Lindström, M. Fogelström, T. Bauch, G. Johansson, S. E. Kubatkin
Physical Review Letters, 111, 137002, (2013).

VII: Effects of quasiparticle tunneling in a circuit-QED realization of a strongly driven two-level system

J. Leppäkangas, S. E. de Graaf, **A. Adamyman**, M. Fogelström, A. V. Danilov, T. Lindström, S. E. Kubatkin, G. Johansson
Journal of Physics B: Atomic, Molecular and Optical Physics, 46, 224019, (2013).

VIII: PC2: Identifying noise processes in superconducting resonators

J. Burnett, T. Lindström, I. Wisby, S. de. Graaf, **A. Adamyman**, A. V. Danilov, S. Kubatkin, P. J. Meeson and A.Ya.Tzalenchuk
Superconductive Electronics Conference (ISEC), 1-3, (2013).

IX: Galvanically split superconducting microwave resonators for introducing internal voltage bias

S. E. de Graaf, D. Davidovikj, **A. Adamyman**, S. E. Kubatkin, A. V. Danilov
Applied Physics Letters, 104, 052601, (2014).

X: Coupling of a locally implanted rare-earth ion ensemble to a superconducting micro-resonator

I. Wisby, S. E. de Graaf, R. Gwilliam, **A. Adamyman**, S. Kubatkin, P. J. Meeson, A. Ya. Tzalenchuk, T. Lindström
Applied Physics Letters, 105, 102601, (2014).

XI: Angular dependant micro-ESR characterization of a locally doped Gd³⁺: Al₂O₃ hybrid system for quantum applications

I. S. Wisby, S. E. de Graaf, R. Gwilliam, **A. Adamyman**, S. E. Kubatkin, P. J. Meeson, A. Ya. Tzalenchuk, T. Lindström
Submitted to *Physical Review Applied*, under review, (2015).

XII: On the nature of spin fluctuators on Al₂O₃: Implications for environmental noise in quantum circuits

S. E. de Graaf, **A. A. Adamyman**, T. Lindström, D. Erts, S. E. Kubatkin, A. Ya. Tzalenchuk, A. V. Danilov
Submitted, manuscript under consideration, (2016).

Abbreviations

AFM	Atomic Force Microscopy
ALD	Atomic Layer Deposition
AM	Amplitude Modulation
BOE	Buffered Oxide Etch
CMP	Chemical Mechanical Polishing
CPW	Coplanar Waveguide
c-QED	circuit Quantum Electrodynamics
DPPH	2,2-diphenyl-1-picrylhydrazyl
DRIE	Deep Reactive Ion Etching
Ebeam	Electron Beam Lithography
EPR	Electron Paramagnetic Resonance
ESR	Electron Spin Resonance
FIB	Focused Ion Beam
FWM	Four-Wave Mixing
HBR	Hydrogen Bromide
HEMT	High Electron Mobility Transistor
HF	HydroFluoric acid
ICP	Inductively Coupled Plasma
IPA	Isopropanol
JPA	Josephson Parametric Amplifier
JPL	Jet Propulsion Laboratory
JTWPA	Josephson Traveling Wave Parametric Amplifier
KI	Kinetic Inductance
KI-TWPA	Kinetic Inductance Traveling Wave Parametric Amplifier
MKID	Microwave Kinetic Inductance Detectors
ML	Multi Layer

Abbreviations

nc-AFM	non-contact Atomic Force Microscopy
NSMM	Near Field Scanning Microwave Microscopy
OM	Optical Microscopy
PCB	Printed Circuit Board
PDH	Pound-Drever-Hall
PLL	Phase Locked Loop
PM	Phase Modulation
RIE	Reactive Ion Etching
SEM	Scanning Electron Microscope
SL	Single Layer
SNR	Signal-to-Noise Ratio
STM	Scanning Tunneling Microscopy
SQUID	Superconducting Quantum Interference Device
TEM	Transverse Electromagnetic
TF	Tuning Fork
TL	Transmission Line
TLF	Two-level Fluctuator
TLS	Two-Level System
TMAH	Tetra Methyl Ammonium Hydroxide
TWPA	Traveling Wave Parametric Amplifier
VNA	Vector Network Analyzer

Contents

Abbreviations	v
Contents	vii
1 Introduction	1
2 Concepts	9
2.1 Transmission Line Theory	9
2.1.1 Impedance mismatch on a terminated TL	12
2.1.2 Transmission through an impedance step	12
2.1.3 Transmission for a lumped element impedance	15
2.1.4 Impedance mismatch on a doubly terminated TL	16
2.1.5 Planar Transmission Lines: Coplanar and Microstrip	17
2.2 Resonators	18
2.2.1 Coplanar Waveguide Resonators	19
2.2.2 Resonator parameters and Transmission response	20
2.2.3 Kinetic Inductance	28
2.3 Parametric Amplification	31
2.3.1 Four-wave mixing	31
2.3.2 Coupled-mode theory	33
2.3.3 Parametric gain	35
2.3.4 Nonlinear phase shift in TWPA	36
2.3.5 Phase Matching	37

CONTENTS

3	Near Field Scanning Microwave Microscopy	41
3.1	Introduction	41
3.2	Challenges to be addressed in NSMM	45
3.3	A slow propagation line for NSMM	45
3.4	Fractal resonator design concepts	46
3.5	Experimental Techniques	48
3.5.1	Microfabrication of fractal resonators for NSMM	48
3.5.2	Cryogenic scanning setup	49
3.6	Results	53
3.7	Summary & Outlook	57
4	Electron Spin Resonance Spectroscopy	59
4.1	Introduction	59
4.2	Challenges to be addressed in ESR	63
4.3	A slow propagation line for ESR	64
4.4	Experimental Techniques	64
4.4.1	Fractal resonator design concepts	64
4.4.2	Microfabrication of fractal resonators for ESR	67
4.5	Results	68
4.5.1	ESR spectroscopy on a DPPH sample	69
4.6	Summary & Outlook	71
5	Kinetic Inductance Traveling Wave Parametric Amplifier	75
5.1	The call for a low-noise, practical amplifier	76
5.2	Challenges to be addressed in KI-TWPA	79
5.3	Slow propagation lines for KI-TWPA	79
5.4	Experimental Techniques	81
5.4.1	Microfabrication of Fractal Lines	81
5.4.2	Measurements	90
5.5	Results	91
5.5.1	Kinetic inductance nonlinearity and parametric gain	96
5.6	Summary & Outlook	98
5.7	The quest for an alternative to the coplanar design	101

5.8	Challenges to be addressed in Tunable Microstrip Resonators . . .	103
5.9	Slow propagation microstrip lines	103
5.10	Experimental Techniques	104
5.10.1	Microstrip resonator design concepts	104
5.10.2	Microfabrication of Microstrip Lines	106
5.10.3	Measurements	107
5.11	Results	109
5.12	Summary & Outlook	113
6	Conclusions	115
A	Derivation of inductively coupled resonant circuit parameters	119
B	Fabrication Recipes	121
C	Calculation of kinetic to geometrical inductance ratio for KI-TWPA	127
	Acknowledgements	129
	Bibliography	131
	Appended Papers	139

CONTENTS

Chapter 1

Introduction

Quantum computing has been hailed as one of the technologies that could radically change the 21st century. Our world advances with an exponentially growing thirst for more computing power. To achieve this, microchips have increasingly been shrinking in size, eventually reaching the size of an atom. Back in 1959, famous physicist R. Feynman said in his visionary talk that: "The principles of physics, as far as I can see, don't speak against the possibility of maneuvering things atom by atom. It is not an attempt to violate any laws; it is something, in principle, that can be done; but, in practice, it has not been done because we are too big." [1]. Feynman's speech served as an inspiration for manipulating individual atoms, producing microchips at nanoscale dimensions and gave a kick-start to the field of quantum computing [2].

Contrary to a classical computer, which can only store information in two separate, zero and one bit states, a quantum computer can store information in quantum bits (qubit) across multiple states at the same time, allowing it to perform millions more calculations per second than any classical computer. To enable the manipulation and read-out of qubits, microwave photons can be used as carriers of quantum information instead of interconnections. While to a non-physicist it certainly sounds alien, quantum mechanics is a subject that puzzles even the most keen scientists. As mathematician John von Neumann once said: "You don't understand quantum mechanics, you just get used to it." [3]. Weird or not, in parallel with exploratory experiments in quantum computing, many remarkable technological advances and achievements were made. Soon after Feynman's

1. Introduction

speech, nanoscience entered a vastly growing phase. The first microscopy tools, such as scanning tunneling microscopy (STM [4]) and atomic force microscopy (AFM [5]), for imaging the 'world at the bottom' were invented. In the late 1960's the electron beam lithography (ebeam) was developed to write nanoscale features [6]. Advances in microfabrication have made it possible to mass-produce nanoscale devices that exhibit quantum effects.

Half a century past Feynman's speech, Wallraff, et al. demonstrated the coupling of a single photon to a superconducting qubit, establishing the concept of circuit quantum electrodynamics (c-QED) [7]. The coherent interaction of qubits with photons, confined in a superconducting microwave resonator, opened up new possibilities for quantum computing experiments [8–10]. Despite many announcements of progress, conceptual implementations of quantum computers have proven to be more elusive than anticipated. Even though conceptual quantum computers have been already demonstrated to be viable using silicon-based materials [11, 12], as well as cryogenic superconductor-based components [13, 14], they still don't outperform commercially available classical computers. One of the reasons has been that for quantum computing to become a reality, qubits need to store the quantum information without its degradation and loss. It turned out to be very tricky to construct robust qubits. In reality qubits couple to a reservoir of spurious, unaccounted two-level fluctuators (TLFs), resulting in a process called dephasing, which destroys the quantum information (decoherence) [15]. Decoherence is the 'Achilles heel' of quantum computing and it is caused by the loss mechanisms intrinsic to qubit materials, that host defects and impurities.

The quantum revolution is already under way, and the prospects that lie ahead are limitless. To pave the way for the quantum technology era, full of interesting possibilities, continuous effort is required to figure out better ways to overcome decoherence, to improve the underlying materials, to expand and functionalize c-QED tool-box with various technologies and instruments and to gain more and more control over the quantum world. Improvements in nanoscale fabrication, as well as spectroscopic characterization techniques will greatly accelerate the mastering of quantum-based technologies.

Near field scanning microwave microscopy (NSMM) is one example of such a characterization technique [16]. With a microwave near field localized at the

scanning tip and a probing power very close to a single photon level, a cryogenic NSMM has a potential to non-invasively study quantum TLFs, as well as investigate the loss mechanisms intrinsic to the underlying materials. The existing NSMM techniques are not optimized for this goal, as they operate in a classical regime at room temperatures with probing powers well above the single photon level.

For this purpose we have developed the first hybrid NSMM-AFM cryogenic system. As the microwave probe, we have employed a high quality (high-Q) superconducting thin film resonator. The trick of shortening the resonator length has been to reduce the wave propagation velocity via increased capacitance in the 'fractalized' resonator. Our resonator is so miniature and light that it doesn't degrade the mechanical quality factor (Q-factor) of the AFM cantilever when integrated on it. The high-Q of the resonator has translated into a greatly reduced probing power and a high microwave sensitivity. On the other hand, we have benefited from the nanometer spatial resolution of the non-contact AFM (nc-AFM). As a result, we can non-invasively (both mechanically and electrically) study material properties at very low powers, important for the coherent interrogation of an individual TLF.

The chase for alternative architectures for quantum information processing and memories has led to the development of another leading approach. Electron spin ensembles, as arrays of natural two-level systems (TLSs), are prospective contenders for long-lived quantum memories due to their exceedingly long coherence times [17]. The envisioned quantum computer should have memory blocks, containing small number of spin arrays. This calls for a method to study spin arrays, composed of small number of spins, and ultimately, to address a single spin. Electron spin resonance (ESR) is a major spectroscopic technique that enables the manipulation of electron spins with microwave photons confined in a resonator [18]. However, in ESR studies the magnetic fields required to bring electron spins into resonance with photons, are much higher than the fields the superconducting resonators can tolerate. This certainly rises the need of a high-Q superconducting resonator, resilient to strong magnetic fields.

The high-Q fractal resonators developed in our group for scanning applications turned out to be also resilient to strong magnetic fields. This was due to a

1. Introduction

i) reduced dissipation, thanks to special current splitting in parallel connected fractal branches, ii) reduced flux focusing, thanks to optimized ground planes. As a result, these high-Q resonators have shown better performance at strong magnetic fields, a spin sensitivity, with a minimum detectable number of spins, four orders of magnitude superior to commercial spectrometers [19] and on par with state of the art experiments [20]. Our observation of an excellent resonator performance and resiliency to strong magnetic fields has made these resonators especially useful for ESR spectroscopy on nanoscale spin samples.

On the way towards being able to measure a single qubit or a single electron spin, a resonator must operate at near single photon level. Here is when we found ourselves in the strong need of a low noise amplifier. To detect and amplify a staggeringly small signal from a few, and ultimately, from a single TLS, a high quality amplifier must have a noise at a single photon level or even less. While semiconductor amplifiers suffer from noise well above the single photon level, parametric amplifiers can reach single photon noise levels. In the microwave domain this is possible through superconducting parametric amplifiers, as the absence of lossy materials suppresses the contribution of thermal fluctuations to the minimum added noise. Still the quantum vacuum fluctuations are unwavering and set the quantum limit of the superconducting parametric amplifier added noise to be $\hbar\omega/2$.

A standard solution for a quantum-limited, superconducting, microwave parametric amplifier is based on Josephson elements, which can only operate at dilution fridge temperatures [21, 22]. Traveling wave parametric amplifiers (TW-PAs), which are utilizing the kinetic inductance (KI) nonlinearity intrinsic to the superconductor instead of Josephson inductance [23], have significantly increased operating temperatures (~ 4 K). For this reason, a TWPA is potentially much more appealing for our NSMM-AFM and ESR techniques. Together with quantum-limited noise performance at temperatures of about few Kelvins, TW-PAs stand out for their potential of high gain and a wide bandwidth [24, 25]. While a prototype quantum-limited TWPA was reported by Eom, et al. in Nature (2012), followed by many other groups, none of them demonstrated a practical device. In order to make the originally weak kinetic inductance-induced nonlinearity enough for obtaining sufficient gain, the superconducting transmission line

has to be around one meter long, one micrometer wide and few tens of nanometers thick. Such a line causes troublesome consequences like a reduced maximum achievable pump power and a limited gain in terms of strong modulations restricting the usefulness of the amplifier. The first issue is a result of weak spots which are impossible to avoid in the fabrication of such a high aspect ratio line. The second issue comes from the high impedance of the high kinetic inductance line. Because of a strong impedance mismatch between the line and the standard $50\ \Omega$ input/output circuitry, the reflections in between the line input and output give rise to ripples in the transmission spectrum.

These challenging problems also found solutions thanks to our slow propagation fractal approach. Most importantly, due to the reduced propagation velocity, we have produced a superconducting line physically much shorter for a given electrical length. Shorter line is less defect-prone as compared to the line in the proof-of-concept amplifier in Eom, et al. [24]. Next, by balancing the high-KI of the line with a high capacitance, we have reduced the line impedance down to $50\ \Omega$ and have managed to suppress reflections due to impedance mismatch. Once we have eliminated gain ripples, we found that the line also couples to spurious resonances. To upshift the spectrum of these resonances, we decided to reduce the KI of the ground plane, while keeping the KI of the line itself high. To this end, we have established a versatile multilayer fabrication technology, which allows to combine high and low KI elements in the same design. As a result, we have demonstrated an average of 6 dB gain, essentially free of modulations and with a line ~ 10 cm long instead of 1 m in the original work [24].

While working on the development of the TWPA, we have realized that a fractal-based approach for implementing slow propagation lines also has its limits. First, a fractal CPW line, with a long perimeter and micrometer wide gaps between superconducting structures, gets easily shorted during fabrication, becoming useless. Second, due to its large transverse dimensions, the fractal line has an increased coupling to spurious ground plane resonances which mess up the transmission spectrum. A new approach was required as an alternative to the fractal solution.

The fractal design allows to greatly boost the per unit length capacitance of the line, thus reducing the propagation velocity and making the line physically

1. Introduction

shorter. An alternative way of slowing down the wave, via increased capacitance, would be to switch to a microstrip design. To get the desired capacitance, the thickness of dielectric layer in the microstrip line should be below $1 \mu\text{m}$. Practically, this implies that the dielectric substrate in between conductors must be replaced with a thin film, deposited dielectric layer. So far, such microstrip lines were inferior to CPWs on crystalline sapphire widely used in the field of c-QED due to poor Q-factors related to lossy thin film dielectric.

Inspired by the earlier reports on promising low loss tangents observed in atomic layer deposited (ALD) oxide, we have decided to try if, by perfecting the fabrication technique, we could reduce the dielectric losses even further, making it on par with the crystalline sapphire used in CPWs. To characterize the dielectric quality, the most straightforward way is to make a microstrip resonator and measure the Q-factor. Thus, we have fabricated a microstrip resonator on the same side of the substrate with Nb-based conductors and ALD oxide. After a set of tricks and trials we have managed to produce a low-loss dielectric. The high quality of the deposited ALD oxide have translated into a dielectric Q-factor of the order of 10^4 with a single photon load in the resonator, rapidly increasing with more photons in the resonator. Thanks to the increased capacitance, we have obtained a wave propagation velocity, reduced almost 3 times compared to typical CPWs and on par with our fractal CPW lines.

In order to implement a microstrip TWPA, apart from the line quality, we also need to know how much of KI-related nonlinearity we can achieve with a microstrip line, or how long the line should be to have a sufficient nonlinearity for a proper gain. A direct way to characterize KI nonlinearity in the resonator is to tune it with a current bias and to trace the resonator frequency. The design flexibility of our microstrip tunable resonators has allowed to incorporate dc bias lines in the design and to tune the resonance frequency through the current-dependent kinetic inductance of the superconductor. More importantly, the frequency tuning was achieved without a detrimental effect on the resonator Q-factor. The resulting slow propagation line-based microstrip resonators combine simplicity, compactness, wide tuning range, fast tuning time and a Q-factor on par (at a single photon load) or superior (at higher powers) to the common CPW-based designs.

Thesis objectives and outline

At the base of the operation of all the above tools, developed in our lab, lies the interaction of quantum systems with microwave photons stored in a section of superconducting, thin film, slow propagation transmission line. The successful realization of various requirements set on these transmission lines helps to face all the mentioned above problems, revealing the wide practicality and usefulness of slow propagation superconducting lines for quantum device applications.

The objective of this thesis is to improve and functionalize the tool-box of c-QED and quantum computing with smart techniques based on NSMM-AFM, ESR and TWPA. In this purpose, the main focus will be to develop and characterize slow propagation line-based superconducting devices for the mentioned applications, opening up a whole new dimension in superconducting circuitry.

The overall structure of this thesis is the following:

Before delving deeper into the subject, **Chapter 2** introduces the basics in transmission line (TL) theory. Two main kinds of planar TLs are discussed to be developed into slow propagation lines - coplanar and microstrip, followed by basic concepts related to TL-based thin film resonators that will be useful throughout the discussion. After this, we go through the basics of parametric amplification, with a set of specific requirements for efficient amplification.

Chapter 3 motivates our choice of NSMM-AFM system, based on a superconducting thin film resonator as a microwave probe. We will go through the hurdles to overcome in this part of the thesis, together with the description of a specific slow propagation line as a remedy for the discussed issues. Next, the fabrication of the microwave probe is explained and our home-made cryogenic NSMM-AFM system is presented. The chapter is concluded with the achievements, results and is summarized in the end (Paper **I**).

Chapter 4 introduces the ESR spectroscopy and the shortcomings of the state of the art techniques. We will detail the modified version of our scanning slow propagation line, adapted to ESR studies of spin ensembles. Next, design considerations and the fabrication method of our superconducting fractal resonators are outlined. The chapter is concluded with the main results and is summarized in the end (Paper **II**).

1. Introduction

Pros and cons of the state of the art parametric amplifiers and a profound analysis of our TWPA, based on a slow propagation fractal line, that utilizes the nonlinearity of kinetic inductance intrinsic to a superconductor is discussed in **Chapter 5**. Further on, the chapter deals with the design principle and experimental techniques used to fabricate, characterize and perform measurements on our slow propagation lines. In particular, the multilayer technology as the workhorse established for TWPA slow propagation line fabrication, is purposed and the issues faced are discussed (Paper **III**, **IV**). After summarizing the important results obtained for TWPA, we will switch to our alternative solution for wave slowing without a fractal design. The remaining material covers our results on tunable microstrip resonators and the study of loss characteristics (Paper **V**). The chapter will conclude with the summary of important conclusions and an outlook for future research will be provided.

Finally, in **Chapter 6** the main results will be reiterated and conclusions will be drawn.

Chapter 2

Concepts

This chapter aims to introduce the basics of transmission line theory and define the quantities and concepts required for the discussion in subsequent chapters. The chapter will begin with a brief introduction of planar transmission line parameters (section 2.1). In section 2.2, TL superconducting resonators will be discussed, together with figure-of-merit quantities and loss mechanisms. Next, we review the nonlinear parameter exploited in our superconducting TL's, i.e. the kinetic inductance. The fundamentals of parametric amplification and the considerations for efficient amplification are addressed in section 2.3.

2.1 Transmission Line Theory

In microwave engineering, to achieve efficient power transfer from one point to the other, transmission lines have been used as guides for electromagnetic propagating waves.

TLs are presented with two or more parallel conductors and when a voltage is applied between them, there are some counter-balanced currents flowing in the conductors, keeping the net current zero. To see how these voltage and current waves are related, let us consider the TL in Fig. 2.1.

For a section of TL with per unit length series resistance R , series inductance L , shunt capacitance C and shunt conductance G , one can directly write TL electromagnetic wave equation solutions for a harmonic voltage and current in

2. Concepts

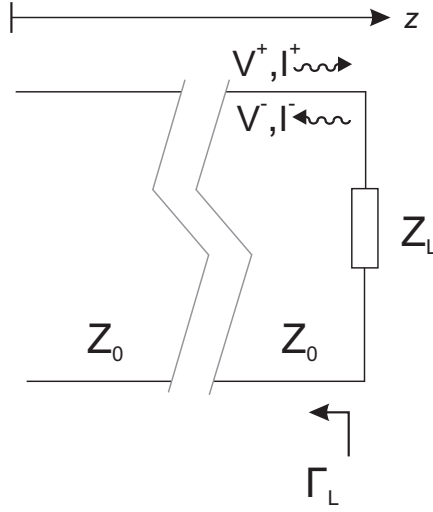


Figure 2.1: Equivalent circuit of a transmission line with a characteristic impedance Z_0 , loaded with a lumped impedance Z_L . Γ_L is the reflection coefficient for the load.

the following way:

$$V = V^+ e^{-\gamma z + j\omega t} + V^- e^{\gamma z + j\omega t}, \quad (2.1)$$

$$I = I^+ e^{-\gamma z + j\omega t} - I^- e^{\gamma z + j\omega t}, \quad (2.2)$$

where the first parts on the right hand side represent forward propagating waves in the positive z direction, with amplitudes V^+ , I^+ and the second parts represent backward propagating waves in the negative z direction, with amplitudes V^- , I^- . ω is the angular frequency and γ is the complex propagation constant given by:

$$\gamma = \sqrt{(R + j\omega L)(G + j\omega C)} = \alpha + j\beta. \quad (2.3)$$

The series resistance R represents the resistance due to a finite conductivity of TL conductors and the shunt conductance G represents losses in the dielectric in between TL conductors. We can rewrite equations (2.1) and (2.2):

$$V = V^+ e^{-\alpha z} e^{-j\beta z + j\omega t} + V^- e^{\alpha z} e^{j\beta z + j\omega t}, \quad (2.4)$$

$$I = I^+ e^{-\alpha z} e^{-j\beta z + j\omega t} - I^- e^{\alpha z} e^{j\beta z + j\omega t}. \quad (2.5)$$

We can see that, for example, $e^{-j\beta z + j\omega t} = e^{j\omega(t - z/v_p)}$, implying that the waves

travel in the line with a propagation velocity $v_p = \omega/\beta = \lambda f$, where $\beta = 2\pi/\lambda$ is the phase constant and λ is the wavelength. Along propagation the waves attenuate in amplitude at a rate defined by α . The ratio of the voltage to current that wave carries, defines the characteristic impedance of the TL:

$$Z_0 = \frac{V^+}{I^+} = \frac{V^-}{I^-} = \sqrt{\frac{R + j\omega L}{G + j\omega C}}. \quad (2.6)$$

Superconducting transmission lines can be approximated as loss-less, resulting in $R = G = 0$ with $\alpha = 0$ and so we will get the following expressions for the propagation constant, propagation velocity and a real characteristic impedance:

$$\gamma = j\beta = j\omega\sqrt{LC}, \quad (2.7)$$

$$v_p = \frac{1}{\sqrt{LC}}, \quad (2.8)$$

$$Z_0 = \sqrt{\frac{L}{C}}. \quad (2.9)$$

$Z_0 \sim 50 \Omega$ for standard microwave devices. Here a question might arise: how is that the impedance of a line with purely non-dissipative elements (C,L) has a purely resistive value in Ohms, i.e. is dissipative? Or if we apply a voltage across a superconducting line without any resistive losses, will the current be infinite, as one would naively expect from Ohm's law? The answer is that in a loss-less line there neither is loss of current across the line, nor the current is infinite. Simply, the infinite distributed inductances and capacitances of the line continuously absorb and store energy from the source, with no dissipation. When current flows, the inductors limit the rate at which it charges the capacitors, in this way establishing the characteristic impedance of the line. This is why the wave propagation in a loss-less line looks like an energy absorption by a pure impedance.

2. Concepts

2.1.1 Impedance mismatch on a terminated TL

Now let us go one step further and consider the scenario when propagating waves in the TL meet a lumped element termination Z_L on one end (Fig. 2.1). As we have already mentioned, a TL is a device that transports energy and has a characteristic impedance of V/I (see Eq. (2.6)). It is interesting to ask what will happen if the load impedance of the TL accepts a different ratio of V/I than the TL ($Z_L \neq Z_0$). In any impedance interface there exist boundary conditions claiming that voltages and currents at the interface must be continuous [26]. The first stems from the conservation of energy and the second comes from the conservation of electric charge. It turns out, to satisfy these boundary conditions between the TL impedance Z_0 and the load impedance Z_L , together with the incident wave, there must be a reflected wave at the interface [27]. If we send a signal with an amplitude V^+ through the TL, at the load the signal will get partly reflected with an amplitude V^- . The load impedance can then be expressed as $Z_L = (V^+ + V^-)/(I^+ - I^-)$. Taking into account Eq. (2.6), we will get $(V^+ + V^-)/(V^+ - V^-) = Z_L/Z_0$. From this expression, we can relate the reflected and incident voltage amplitudes:

$$\Gamma_L = \frac{V^-}{V^+} = \frac{Z_L - Z_0}{Z_L + Z_0}, \quad (2.10)$$

where Γ_L is the reflection coefficient for the load. In case of a perfect match $Z_L = Z_0$, TL behaves as an infinitely long line for reflections and $\Gamma_L = 0$. In other words, we can say that all the power is transmitted to the load, nothing is reflected and energy flows in one direction only. If the load is open circuited ($Z_L = \infty$), then the reflection coefficient is $\Gamma_L = 1$ and the whole signal will reflect back, in phase with the incident wave. Instead, if the load is short circuited ($Z_L = 0$), then $\Gamma_L = -1$ and the whole reflected signal will be 180° out of phase with respect to the incident wave.

2.1.2 Transmission through an impedance step

Now let us consider the TL impedance step ($Z_1 \neq Z_2$), pictured in Fig. 2.2, as the most general situation. On Port 1 we will have an incident wave with

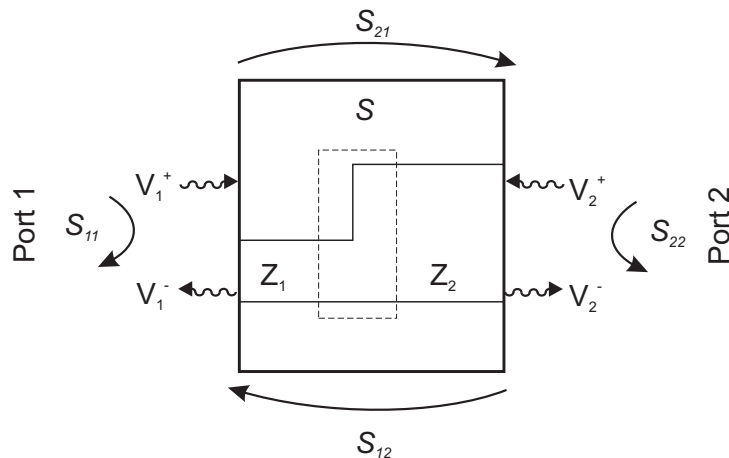


Figure 2.2: S-matrix representation of a step in TL impedance.

amplitude V_1^+ and a back reflected wave with an amplitude V_1^- . On Port 2 there will be a transmitted wave with an amplitude V_2^- and an incoming wave with an amplitude V_2^+ . The incoming waves from both sides will be partly transmitted through the step with a coefficient defined as the ratio of the transmitted to the incident voltage amplitude. For example, at Port 1 the transmission coefficient will be:

$$T = \frac{V_2^-}{V_1^+}. \quad (2.11)$$

T and Γ are not independent. The conservation of energy requires that $T = 1 + \Gamma$.

In the microwave domain there is no multimeter that can directly measure voltages and currents. Instead, with a Vector Network Analyzer (VNA) it is possible to measure transmitted and reflected (scattered) wave amplitudes¹ and phases relative to those of the incident wave. This relationship is described by the S Scattering matrix $[V^-] = [S][V^+]$, which couples incoming and outgoing waves. The number of S -parameters necessary to describe a network is equal to $(\text{Number} - \text{of} - \text{ports})^2$, i.e. a two-port TL will need four S -parameters: $S_{11}, S_{22}, S_{21}, S_{12}$. S_{11} and S_{22} are equivalent to input and output complex reflection coefficients, while S_{21} and S_{12} are equivalent to forward and backward complex transmission coefficients. In the context of this work, it is useful to

¹Note, in VNA the measured amplitudes are presented in power units, which means amplitude squared is measured.

2. Concepts

derive the S -parameters for the impedance step in Fig. 2.2:

$$\begin{aligned} V_1^- &= S_{11}V_1^+ + S_{12}V_2^+, \\ V_2^- &= S_{21}V_1^+ + S_{22}V_2^+. \end{aligned} \quad (2.12)$$

As we have noted earlier, voltages and currents at the impedance boundary must be continuous: $V_1 = V_2$, $I_1 + I_2 = 0$. The total voltages and currents on each side of the boundary are defined in the following way:

$$V_1 = V_1^+ + V_1^-, V_2 = V_2^+ + V_2^-, \quad (2.13)$$

$$I_1 = I_1^+ - I_1^-, I_2 = I_2^+ - I_2^-. \quad (2.14)$$

Also, taking into account that the voltage to current ratio on each side simply corresponds to the impedance, we will get:

$$V_1^+ + V_1^- = V_2^+ + V_2^-, \quad (2.15)$$

$$\frac{V_1^+}{Z_1} - \frac{V_1^-}{Z_1} + \frac{V_2^+}{Z_2} - \frac{V_2^-}{Z_2} = 0. \quad (2.16)$$

From (2.15) we get,

$$V_1^- = V_2^+ + V_2^- - V_1^+. \quad (2.17)$$

Inserting (2.17) into (2.16) and arranging, we arrive at,

$$V_2^- = \frac{2 \cdot Z_2}{Z_1 + Z_2} \cdot V_1^+ + \frac{Z_1 - Z_2}{Z_1 + Z_2} \cdot V_2^+. \quad (2.18)$$

Inserting (2.18) into (2.15) will give:

$$V_1^- = \frac{Z_2 - Z_1}{Z_1 + Z_2} \cdot V_1^+ + \frac{2 \cdot Z_1}{Z_1 + Z_2} \cdot V_2^+. \quad (2.19)$$

From (2.12), (2.18) and (2.19), we can derive the S -parameters for a step in

impedance:

$$\begin{aligned} S_{21} &= \frac{2 \cdot Z_2}{Z_1 + Z_2}, & S_{22} &= \frac{Z_1 - Z_2}{Z_1 + Z_2}, \\ S_{11} &= \frac{Z_2 - Z_1}{Z_1 + Z_2}, & S_{12} &= \frac{2 \cdot Z_1}{Z_1 + Z_2}. \end{aligned} \quad (2.20)$$

Hence the S -matrix will be:

$$S = \frac{1}{Z_1 + Z_2} \cdot \begin{pmatrix} Z_2 - Z_1 & 2 \cdot Z_1 \\ 2 \cdot Z_2 & Z_1 - Z_2 \end{pmatrix}.$$

Later in section 2.3.5 we will make use of steps in impedance for implementing a so-called, dispersion engineering for our TWPA line.

2.1.3 Transmission for a lumped element impedance

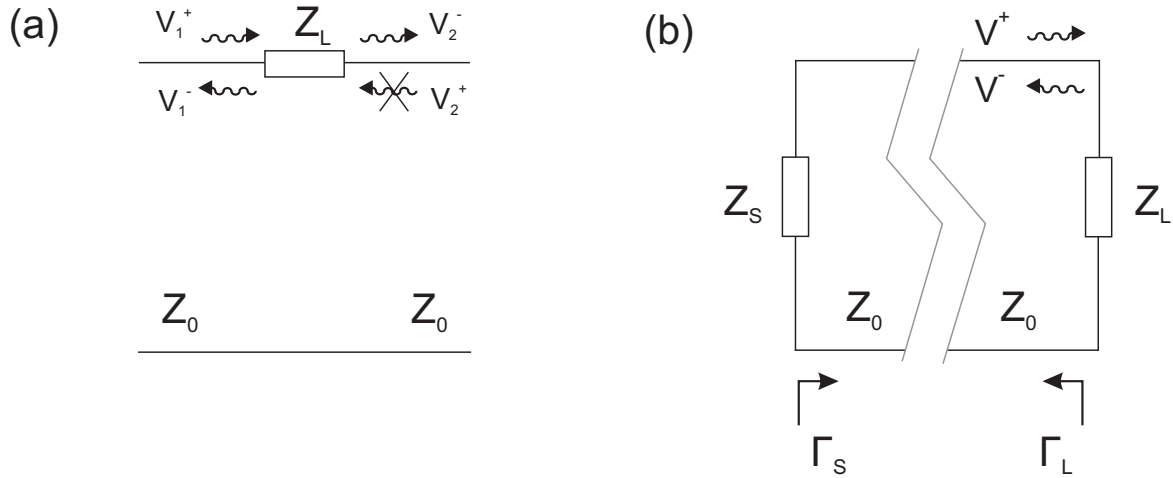


Figure 2.3: (a) A series lumped element impedance in a TL. (b) TL terminated with lumped element shunt impedances at both ends.

In case TL has a series impedance Z_L like in Fig. 2.3 (a), S_{11} is simply the reflection on Z_L and Z_0 connected in series [26]:

$$S_{11} = \frac{Z_0 - (Z_0 + Z_L)}{Z_0 + (Z_0 + Z_L)} = \frac{-Z_L}{2Z_0 + Z_L}. \quad (2.21)$$

Assuming that the line is matched on the right and $V_2^+ = 0$, from equations

2. Concepts

(2.15) and (2.12) we can get

$$V_1^+ + S_{11}V_1^+ = V_2^-,$$

$$S_{21} = 1 + S_{11} = \frac{2Z_0}{2Z_0 + Z_L}. \quad (2.22)$$

2.1.4 Impedance mismatch on a doubly terminated TL

If the TL is terminated with lumped element shunt impedances at both ends, after getting reflected on the load the wave will eventually come back to the source (Fig. 2.3 (b)). In case the source impedance Z_S also differs from Z_0 , another reflected wave will be generated at the source of the TL, with a reflection coefficient Γ_S . The new reflected wave will head towards the load, together with the original incident signal. Then, both these waves will get reflected on the load, and so on. This resembles an end-less game of ping-pong, the wave being the ball going back and forth. Furthermore, in the described system there will be multiple such tennis matches happening at the same time.

An analogue device in optics is the conventional Fabry-Perót interferometer (Fig. 2.4) [28]. In this case, the light is getting multiply reflected between 2 reflecting surfaces, located at a distance L far from each other. If all these left and right traveling waves are in phase, they interfere constructively, otherwise they interfere destructively and excite so-called, standing waves. The standing

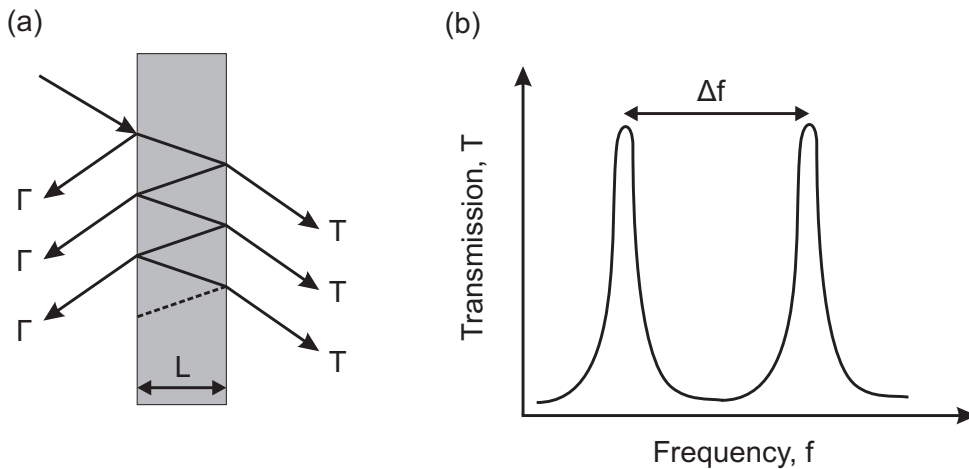


Figure 2.4: (a) A sketch of Fabry-Perót multiple reflections. (Reproduced from [29]). (b) The transmission as a function of frequency.

waves are at maximum/minimum in case of a constructive/destructive interference. Whether the component waves are in-phase or out-of-phase, depends on the phase δ they acquire in one tour-retour excursion. The transmission function is given by [29]:

$$T_{FP} = \frac{1}{1 + F \sin^2(\delta/2)}, F = \frac{4R}{(1 - R)^2}, \quad (2.23)$$

where R is the surface reflectance. The frequency spacing between two adjacent Fabry-Perót peaks (or ripples) in the transmission spectrum is inverse proportional to the distance between the reflective surfaces:

$$\Delta f \sim \frac{1}{L}. \quad (2.24)$$

The ratio of voltage (or current) maximas and minimas is described with the standing wave ratio:

$$SWR = \frac{V_{max}}{V_{min}} = \frac{I_{max}}{I_{min}} = \frac{1 + |\Gamma|}{1 - |\Gamma|}. \quad (2.25)$$

$SWR = 1$ means no reflection, while $SWR = \infty$ corresponds to total reflection. For a nice visualization of standing waves, a film by J. N. Shive [30] is highly recommended.

The standing waves are undesirable, as they cause excessive losses due to dissipation. To avoid such losses in a microwave device and to achieve an efficient power transfer, a proper impedance matching is a must. Later, in section 5.3, we will learn how to get rid of the unwanted reflections due to impedance mismatch in-between TWPA line and in/out terminals, eliminating the Fabry-Perót ripples from the transmission spectrum.

2.1.5 Planar Transmission Lines: Coplanar and Microstrip

Planar TLs are divided into two major types: coplanar and microstrip. A schematic drawing of conventional coplanar and microstrip transmission lines is demonstrated in Fig. 2.5. The Coplanar TL consists of a central conductor (width - w , thickness - t) in between two ground plane conductors (thickness - t , gap - g), all located on the same side of a dielectric substrate (substrate thickness

2. Concepts

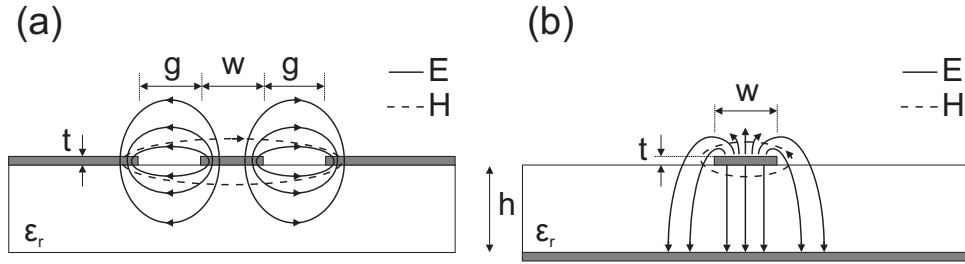


Figure 2.5: Planar transmission lines with Electric and Magnetic field lines. (a) Coplanar transmission line, (b) Microstrip transmission line.

- h), (Fig. 2.5 (a)). The microstrip TL consists of a top conductor (width - w , thickness - t) and a bottom conductor (ground plane), located on opposite sides of a dielectric substrate (Fig. 2.5 (b)).

As we can see, one difference between coplanar and microstrip TLs is the dielectric thickness between the central (top) conductor and the ground plane. The small gap in case of CPW transforms into a much reduced microwave mode volume. Another difference is that in case of a coplanar line, the current flowing through the central conductor has a direction opposite to that of the current flowing in the surrounding ground planes, indicating low radiation losses (more about losses in section 2.2.2). Also the microwave field is mainly confined in the gaps between the conductors.

The similarity is that both coplanar and microstrip TLs support a quasi-Transverse Electromagnetic (TEM) wave (not exactly TEM wave), as the dielectric constant above and below the central (top) conductor is not the same. In a quasi-TEM wave, electric and magnetic fields are orthogonal to each other and to the wave propagation direction ($\mp z$), as shown in Fig. 2.5.

2.2 Resonators

Resonators are microwave devices for storing electromagnetic energy, which oscillates between electric energy stored in a capacitor and magnetic energy stored in an inductor. Generally, TL resonators are implemented from a TL segment with a finite length. To obtain full power reflection at both ends, they are either short-circuited or left open, thus providing a resonance whenever the length is a

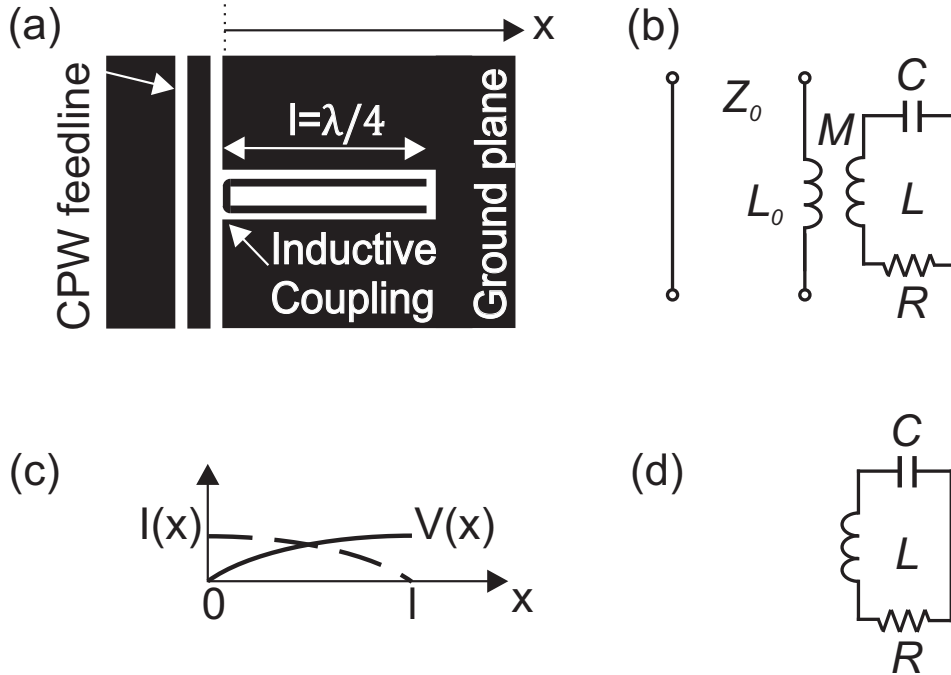


Figure 2.6: (a) The sketch of a $\lambda/2$ TL resonator consisting of two $\lambda/4$ sections in series. The resonator is inductively coupled to the CPW feedline from the left side, and is left open from the right side. Metal is in black color. (b) Lumped element representation of the resonator in (a), inductively coupled to a microwave feedline. (c) Microwave current (dashed line) and voltage (full line) mode distributions along each $\lambda/4$ section of the resonator in (a). (d) Lumped element representation of a basic $\lambda/4$, open-ended resonator, without coupling.

multiple of $1/4$ wavelength [31].

2.2.1 Coplanar Waveguide Resonators

Coplanar waveguide resonators (CPW) have been essential building blocks in microwave photon detectors [32], c-QED [10, 33, 34] and ESR setups [18, 35].

In the scope of this thesis we will be dealing with a $\lambda/2$ CPW resonator with two open ends, folded as a tuning fork and in the middle point inductively coupled to an external feeder (see Fig. 2.6 (a)). Due to such coupling only the odd modes of the resonator are excited and the spectrum is equivalent to that of two $\lambda/4$ prongs, connected in series. The current amplitude is at maximum in the inductive coupling area, and the voltage amplitude is at maximum at the open end of each prong (shown in Fig. 2.6 (c)) (Paper I, II).

2. Concepts

2.2.2 Resonator parameters and Transmission response

As a basic case we discuss here a simple $\lambda/4$ resonator, which is short-terminated on one end and open on the other. The resonance frequencies of $\lambda/4$ resonator occur at $f_n = (2n + 1)c/4l$, that is when the line is an odd multiple of a quarter wavelength long (n is an integer, l is the resonator length, c is the speed of light in vacuum). In practice, if only one resonance is relevant for a specific application, then a single-resonant-frequency lumped element circuit represents the TL resonator fair enough [26]. Thus, for intuitive understanding we can replace our resonator with its equivalent series lumped element resonant circuit in the vicinity of fundamental resonant frequency for which $l = \lambda/4$ (Fig. 2.6 (b)).

In this section, we will briefly discuss the main properties for the resonator shown in Fig. 2.6. More detailed derivation can be found in Appendix A. The impedance of the lumped element unloaded resonator, shown in Fig. 2.6 (d), near the resonance frequency is

$$Z_r = R(1 + 2jQ_i \frac{\Delta\omega}{\omega_0}), \quad (2.26)$$

where $\Delta\omega = \omega - \omega_0$ is the detuning from resonance frequency ω_0 . Q_i is the internal or unloaded quality factor (Q-factor), expressing resonator intrinsic losses and can be defined by the ratio of energy stored and power dissipated in the resonator:

$$Q_i = \omega_0 \frac{E_{stored}}{P_{dissip}} = \omega_0 \frac{LI^2/2}{RI^2/2} = \frac{\omega_0 L}{R} = \frac{1}{\omega_0 RC} = \frac{Z_0}{R}. \quad (2.27)$$

Here $\omega_0 = \sqrt{1/LC}$ is the resonance frequency and $Z_0 = \sqrt{L/C}$ is the characteristic impedance.

When the resonator is inductively coupled to the microwave feedline like in Fig. 2.6 (b), then the input impedance of the resonator is given by [27, 36]

$$Z_{in} = j\omega L_0 + \frac{\omega^2 M^2}{R + j(\omega L - \frac{1}{\omega C})}, \quad (2.28)$$

where M is the mutual inductance between the coupling loop and the TL, L_0 is

the inductance of the coupling loop. For a coupled or loaded resonator, the ratio of internal to external Q-factors is given by

$$\frac{Q_i}{Q_e} = \frac{P_e}{P_i} = \frac{\omega_0^2 M^2}{2RZ_0}, Q_e = \frac{2LZ_0}{\omega_0 M^2}. \quad (2.29)$$

In Eq. (2.29), Q_e represents the external Q-factor and relates to the energy absorbed by the external load (feedline) to which the resonator is coupled. The S_{21} transmission for the circuit in Fig. 2.6 (b), which is similar to the one in Fig. 2.3 (a), can be derived from Eq. (2.22) for $Z_L = Z_{in}$ [37]

$$S_{21} = \frac{2}{2 + \frac{Z_{in}}{Z_0}} = \frac{S_{21,min} + 2jQ_{tot}\frac{\Delta\omega}{\omega_0}}{1 + 2jQ_{tot}\frac{\Delta\omega}{\omega_0}}, \quad (2.30)$$

where Q_{tot} is the total (loaded) Q-factor and can be expressed in terms of Q_e, Q_i : $1/Q_{tot} = 1/Q_e + 1/Q_i$. $S_{21,min}$ is the value of S_{21} at resonance. Taking into account the asymmetry factor due to, for example, large inductive coupling loop or coupling to spurious ground plane resonances, the transmission coefficient becomes [38]

$$S_{21} = 1 - \frac{(1 - S_{21,min})e^{j\varphi}}{1 + 2jQ_{tot}\frac{\Delta\omega}{\omega_0}}, \quad (2.31)$$

where φ is the asymmetry parameter. Eq. (2.31) simply implies that for frequencies far from the resonance frequency, $S_{21} = 1$, i.e. almost all the incident power gets transmitted. Instead, when $\omega = \omega_0$, $S_{21} = S_{21,min}$ and is defined as

$$S_{21,min} = \frac{Q_e}{Q_i + Q_e}. \quad (2.32)$$

From Eq. (2.32), three regimes can be differentiated depending on the ratio between internal and external losses in the resonator:

1. $Q_i \gg Q_e$, an overcoupled, low-loss resonator with $S_{21,min} \rightarrow 0$,
2. $Q_i \ll Q_e$, an undercoupled, lossy resonator with $S_{21,min} \rightarrow 1$,
3. $Q_i = Q_e$, a critically coupled resonator with $S_{21,min} = 1/2$.

2. Concepts

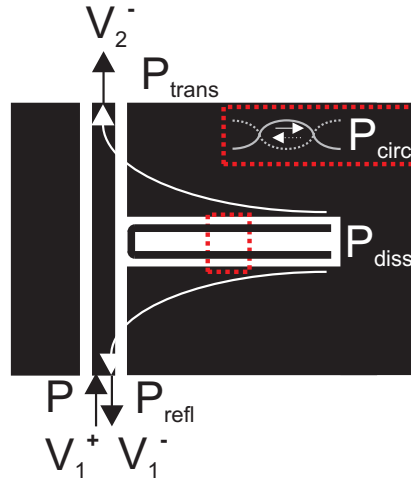


Figure 2.7: Powers in $\lambda/2$ CPW TL resonator.

Power in the resonator

To know the number of photons present in the resonator, it is instructive to introduce the concept of circulating power and to consider how it depends on the excitation power passing through the feeder line.

The boundaries at two ends of the resonator in Fig. 2.7 give rise to reflections and standing waves. The standing waves develop inside the resonator as a superposition of propagating and counter propagating microwaves. We can think of these left and right moving waves carrying the power in the resonator back and forth, as if some power P_{circ} is circulating in the resonator (Fig. 2.7). Besides the incident P and the circulating P_{circ} powers, there is also a power that relates to dissipated energy inside the resonator (P_{diss}), a power related to the energy that is reflected back to the source (P_{refl}) and a power that is transmitted and measured (P_{trans}). We will define the circulating power for the resonator pictured in Fig. 2.7 [39].

In Eq. (2.27), we have already defined the Q-factor, which is the ratio of energy stored in the resonator and the power dissipated in the system $P_{diss} = \frac{P_{circ}}{Q_i}$. Then the reflected and transmitted powers will be

$$\begin{aligned}
 P_{refl} &= \frac{\omega_0 E}{2Q_e} = \frac{P_{circ}}{2Q_e} = \frac{(V_1^-)^2/Z_r}{(V_1^+)^2/Z_0} \cdot P, \\
 P_{trans} &= \frac{(V_2^-)^2/Z_r}{(V_1^+)^2/Z_0} \cdot P.
 \end{aligned} \tag{2.33}$$

Inserting $V_2^-/V_1^+ = S_{21}$ and $V_1^-/V_1^+ = S_{11} = S_{21} - 1$ and taking into account equation (2.32), we get

$$\begin{aligned}
 P_{trans} &= \frac{|S_{21}|^2 Z_0}{Z_r} \cdot P = \frac{Q_{tot}^2 Z_0 P}{Q_i^2 Z_r}, \\
 P_{refl} &= \frac{P_{circ}}{2Q_e} = \frac{|S_{21} - 1|^2 Z_0}{Z_r} \cdot P, \\
 P_{circ} &= \frac{2Q_{tot}^2 Z_0 P}{Q_e Z_r}.
 \end{aligned} \tag{2.34}$$

From Eq. (2.34), we can deduce that:

1. $Q_i \gg Q_e, P_{trans} \rightarrow 0$
2. $Q_i \ll Q_e, P_{circ} \rightarrow 0$
3. $Q_i = Q_e, P_{trans} \approx P/4, P_{circ} \approx P/2.$

If the resonator is overcoupled (case 1), then there is no transmitted power to measure. If the resonator is undercoupled (case 2), there is no power in the resonator for exciting the TLS, coupled to the resonator. The critically coupled resonator (case 3) is the most favorable case, as the measured power is on the same order as the power in the resonator.

From P_{circ} , it is possible to estimate the average number of photons in the resonator simply by

$$\langle N \rangle = \frac{P_{circ}/\omega_0}{\hbar\omega_0} = \frac{2Q_{tot}^2 Z_0 P}{Q_e Z_r \hbar\omega_0^2}. \tag{2.35}$$

At resonance, when $\Delta\omega = 0$ and resonator impedance has a minimum value, the current flowing through the resonator reaches its maximum value, thus the power absorbed in the resonator is at maximum.

When $\Delta\omega = \omega_0/2Q_{tot}$, the absorbed power will be half (i.e. -3 dB below) of its maximum value. Thus for an overcoupled resonator a rapid Q-factor estimation can be done with the resonant frequency and the resonance bandwidth: $Q_{tot} = \omega_0/BW$, where BW is the frequency range at half-height power level.

2. Concepts

Resonator internal losses

In general there are few loss mechanisms that sum up to give the total internal losses in the resonator.

$$\frac{1}{Q_i} = \frac{1}{Q_{rad}} + \frac{1}{Q_d} + \frac{1}{Q_B} + \frac{1}{Q_\sigma}, \quad (2.36)$$

where $1/Q_{rad}$ represents radiation losses, $1/Q_d$ stands for dielectric losses, $1/Q_B$ are losses associated with magnetic field, and $1/Q_\sigma$ is for conducting losses. To achieve high-quality resonators, all loss mechanisms have to be suppressed. Here we will briefly describe them.

- **Radiation losses**

In CPW resonators with a dielectric below and air above the conductors, power is radiated as the fields are not completely confined in the gaps between the central conductor and the ground plane, and radiate out constituting to internal losses. CPW is a combination of two slot lines, each with some current dipole momentum $\sim I \cdot l$, where l is the resonator length, I is the current in each half of the dipole. In case of the CPW even mode sketched in Fig. 2.5 (a), the dipole momenta of two slot lines cancel each other, resulting in not radiating CPW. However, the dipole momenta sum up giving rise to a considerable radiation in case of a CPW odd-mode. In this case, two ground planes next to the central conductor have opposite potentials and the EM field lines go from one ground plane to the other, skipping the central conductor. The radiated power can be evaluated as [40] $P_{rad} \sim \frac{\pi^2}{3c} (\frac{I \cdot l}{\lambda})^2$. Then the radiation Q-factor can be estimated as $Q_{rad} \sim \frac{1}{P_{rad}} \sim \frac{\lambda^2}{l^2}$. To suppress possible radiation losses, the resonator length must be kept as short as possible. To minimize radiation losses, it is recommended to avoid any discontinuity, asymmetry in the CPW structure and to connect the ground planes with wire-bonds.

- **Dielectric losses**

CPW resonators are especially interesting for quantum computation applications in the quantum regime: at low temperatures and with close-to-

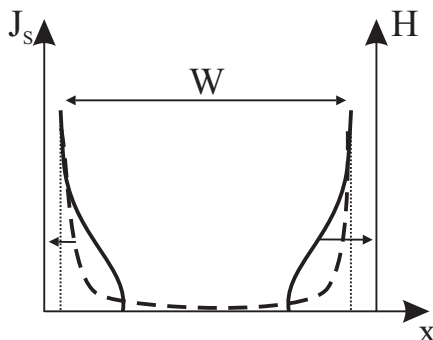


Figure 2.8: Current density (dashed), flux density (solid) for a superconducting strip with width W .

single-photon circulating power. Under these conditions Q_i is known to be limited by coupling to parasitic two-level fluctuators (TLFs) [41]. TLFs are localized states that absorb and dissipate energy at low powers and temperatures. TLFs can reside in a bulk dielectric substrate, on substrate-superconductor interface, as well as in the native surface oxide of the superconductor. It is possible to suppress the TLF-related loss mechanism with high powers and temperatures. This will transform into the increase of $Q_d = 1/\tan \delta$, where $\tan \delta$ represents the loss tangent of dielectric material [42]. It was reported that TLF-related losses can be significantly lowered by careful sample surface treatment before sputtering, or, for example, by using Nitrides as superconducting materials, that are less susceptible to oxidation in air [43].

- **Magnetic-field caused losses**

A static magnetic field applied to a CPW superconducting resonator will introduce dissipation in its turn, degrading the internal Q -factor. According to the Meissner effect, at temperatures $T < T_c$ the magnetic field is expelled from a superconductor via surface screening currents. London penetration depth λ_L is the distance from the surface of a superconductor, over which both the magnetic field and the current density decay exponentially with depth x [44]:

$$B = \mu_0 H e^{-x/\lambda_L}, J_s = J_{s0} e^{-x/\lambda_L}. \quad (2.37)$$

Type-II superconductors like Nb, NbN, at fields $H_{c1} < H < H_{c2}$ (H_{c1}, H_{c2}

2. Concepts

are the first and second critical fields) enter a mixed state, where magnetic flux penetrates the superconductor via Abrikosov vortex structure. Each vortex has a quantized flux of Φ_0 and there is a circulating surface supercurrent around each vortex core, separating a local normal region inside the vortex from a superconducting region. The superconductor tries to keep the number of such vortices as many as possible [45].

The local vortex density in a superconducting strip is given by $\mu_0 H(x, H_0) / \Phi_0 = n$, where n is the number of vortices per unit area, $H(x, H_0)$ is the local magnetic field proportional to H_0 applied magnetic field and μ_0 is the vacuum permeability. The microwave currents make these vortices move, so that the local dissipation is proportional to current and flux densities in the superconducting strip with a width W and the total dissipation in the strip can be found as in Eq. (2.38) [46]

$$\frac{1}{Q_B} \propto \int_{-W/2}^{W/2} \int_0^L \int_0^{2\pi/\omega} |H(x, H_0)| |J(x, z)|^2 \sin^2(\omega t) dx dz dt, \quad (2.38)$$

where L is the resonator length. Both the local field and the current density are at maximum at the strip edges and attenuate towards the strip center because strip surface currents still try to expel the magnetic field on the edges (see Fig. 2.8). With increasing applied field the current density increases and reaches its maximum value. This state is described by the critical-state or Bean model, according to which the flux density profile is a straight line, where the current density is clipped to the critical current density value [47]. Local magnetic field-induced dissipation mainly comes from superconductor strip edge dissipation. We can separate magnetic-field induced losses from the total internal losses in the resonator by introducing a corresponding Q-factor Q_B defined as:

$$\frac{1}{Q_B} = \frac{1}{Q_i(B)} - \frac{1}{Q_i(B=0)}. \quad (2.39)$$

To prevent the vortices from moving and to reduce the dissipation, the vortices can be 'pinned'. Such pinning centres can be local impurities in

the superconductor or specially introduced holes in the resonator design.

On top of vortex movement, there is also an effect called flux focusing, when the expelled magnetic flux is focused in the narrow gaps between, for example, the CPW central strip and the ground plane. As a result, the effective magnetic field gets much larger and vortices start to penetrate the superconductor at much lower applied fields.

In order to minimize magnetic field-induced losses, the following points need to be considered (Paper II):

- To suppress dissipation due to currents flowing in the structure, a careful microwave engineering is required.
- To reduce flux-induced dissipation, holes are introduced in the ground plane and the central conductor as flux pinning centers [48, 49].
- To reduce flux focusing, the amount of superconducting material needs to be reduced. Also, its important to make sure there is always an open path for the flux to escape.

• Conducting losses

Surface currents on the superconductor completely screen static electric fields. On the contrary, superconductors show finite dissipation in case of ac fields. The reason is the following: the ac electric field accelerates Cooper pairs, which own some mass. Because of this mass the superconducting current is retarded with respect to the field and does not screen it completely. At the same time, this field acts on normal electrons, which scatter and dissipate.

At high frequencies, conducting losses become prominent, which can be described by the two-fluid model [47]. According to this model, the density of electrons in the superconductor can be modeled as $n = n_s + n_n$, where n_s is the density of the Cooper pairs (super-fluid) and n_n is the density of normal electrons (normal-fluid). In the low frequency limit $\omega\tau_n \ll 1$, where $\tau_n \sim 10^{-11}$ s is the average time between scatterings for normal electrons and assuming no scattering for Cooper pairs ($\tau_s \rightarrow \infty$), the total conductivity

2. Concepts

is related to complex super-fluid and real normal-fluid conductivities in the following way [47]:

$$\begin{aligned} \sigma &= \sigma_n - i\sigma_s, \\ \sigma_n &= \frac{e^2\tau_n n_n}{m_e}, \sigma_s = \frac{e^2 n_s}{\omega m_e}, \end{aligned} \quad (2.40)$$

where ω is the angular frequency. This approximation holds for frequencies below the BCS energy gap. σ_s corresponds to the admittance $1/j\omega L_s$ of an imaginary inductive channel in parallel with a real resistive channel of conductance $1/R_n$ in the superconductor. Here L_s is associated with the kinetic energy of Cooper pairs and will be discussed in the next section. Such a circuit has a characteristic frequency $\omega \sim 1/\tau_n \sim 10^{11}$ Hz, below which the current through the loss-less inductive channel dominates and the inductor acts as a short. At all nonzero frequencies there is also a small fraction of current flowing through the $1/R_n$ resistive channel, giving rise to a nonzero dissipation in a superconductor and limiting the internal Q-factor of the resonator.

For an ac current density J , the dissipated power per unit volume is $\approx (\sigma_n/\sigma_s^2)J^2 = \sigma_n E^2$. From this, we can draw two conclusions. First, the dissipation depends on $\sim \omega^2$, the electric field must increase with ω , because it has less time to accelerate the super-fluid. Second, the dissipation (at $T < T_c$) is proportional to n_n , implying a dissipation channel through the normal-fluid.

From Eq. (2.27), it is possible to relate the conductive losses to the complex impedance of the superconductor [50]:

$$Q_\sigma = \frac{\omega L_s}{R_n} \sim \frac{n_s}{n_n \omega}. \quad (2.41)$$

2.2.3 Kinetic Inductance

Kinetic inductance is the dominant part of the total inductance in some superconducting microwave circuits. Thanks to its dependence on magnetic field, temperature and dc bias current, kinetic inductance allows to tune impedance,

propagation velocity and the resonance frequency of microwave circuits.

Within the framework of the two-fluid model discussed in the previous section, the Cooper pairs are accelerated with an inertia term L_k , the so-called kinetic inductance of the superconductor. In addition to L_k , there is also an electromagnetic inductance L_m due to the energy stored in the magnetic field generated by the current in the superconductor. Then, the total inductance becomes $L_s = L_m + L_k$.

For the CPW geometry shown in Fig. 2.5 (a), the electromagnetic or geometrical inductance per unit length is given by

$$L_m \approx \frac{\mu_0}{4} \frac{K(k')}{K(k)}, \quad (2.42)$$

where K is the complete elliptic integral, $k' = \sqrt{1 - k^2}$ and $k = w/(w + 2g)$, w is the central strip width, g is the central-to-ground gap width. L_m depends only on CPW geometry.

L_k is derived from the kinetic energy of Cooper pairs [51]

$$\begin{aligned} E_k &= \int \frac{1}{2} n_s m \langle v \rangle^2 dS, \\ J_s &= -en_s \langle v \rangle, \end{aligned} \quad (2.43)$$

where m is the electron mass, $\langle v \rangle$ is the average velocity of Cooper pairs. Inserting $\langle v \rangle$ from J_s into E_k , we get

$$E_k = \frac{1}{2} L_k I^2 = \frac{1}{2} \frac{m}{e^2 n_s} \int J_s^2 dS = \frac{1}{2} \mu_0 \lambda_L^2 \int J_s^2 dS, \quad (2.44)$$

where $\lambda_L = \sqrt{m/(\mu_0 n_s e^2)}$ is the London penetration depth. The Cooper pair current density is $J_s = I/wt$ for a thin film superconductor ($t < \lambda_L$) with a uniform current distribution. The kinetic inductance will then be:

$$L_k = \frac{\mu_0 \lambda_L^2}{wt}. \quad (2.45)$$

So it can be seen that L_k strongly depends on geometry and it quickly grows as CPW strip thickness becomes small. L_k grows also for a narrow and long CPW

2. Concepts

central conductor. Additionally, L_k depends on temperature (T), magnetic field (B) and dc bias current (I) in the superconductor via λ_L .

In thin film superconducting structures, made of NbN or Nb, L_k typically dominates over L_m . Further on, with a varying L_k of the superconductor, it is possible to obtain shifts in resonance frequency, as for $L_k \gg L_m$, $f = 1/(2\pi\sqrt{L_k C})$. A small shift in a resonance frequency can be approximated as follows [52]

$$\frac{\delta f(T, B, I)}{f(0)} = \frac{-\delta L_k(T, B, I)}{2L_k(0)}, \quad (2.46)$$

where $L_k(0) = \hbar R_n / \pi \Delta$ relates to the superconductor band-gap Δ and normal state resistance of the film R_n , according to Mattis-Bardeen theory [53].

The **temperature dependence** of L_k originates from $n_s(T) \approx n_s(0)(1 - T/T_c)$ for $T \rightarrow T_c$ [54],

$$L_k(T) = L_k(0) \frac{1}{1 - T/T_c}. \quad (2.47)$$

The **magnetic field dependence** of L_k comes from the magnetic field dependence of the penetration depth. According to Ginzburg-Landau theory for a thin superconducting film in a magnetic field H [55]

$$\lambda_L(H)^{-1} = \lambda_L(0)^{-1} \left(1 - \alpha \left(\frac{H}{H_{c\parallel}}\right)^2\right), \quad (2.48)$$

where α is a proportionality constant and $H_{c\parallel}$ is the critical field of the superconductor in parallel-to-plane direction.

The **current dependence** of L_k can be obtained from Ginzburg-Landau theory, valid for low bias currents $I \ll I_*$ [55, 56]:

$$L_k(I) \approx L_k(0) \left(1 + \frac{I^2}{I_*^2}\right), \quad (2.49)$$

where I_* is the characteristic nonlinearity parameter, which, according to BCS theory, is related to the critical current I_c and is constrained by [54]: $I_* > 1.9I_c$. Eq. (2.49) can be interpreted as the higher the flow of Cooper pairs, the higher their kinetic energy, thus the larger the L_k .

2.3 Parametric Amplification

Towards mastering NSMM-AFM and ESR techniques, and ultimately, for the interrogation of a single TLS, we shall develop microwave reflectometry measurements on a resonator loaded with a single photon. The need to measure a signal at a single photon level calls for an amplifier with an added noise close to a single photon. The best semiconductor amplifiers are still far from the single photon level [57]. A quantum-limited amplification was possible to achieve with parametric amplifiers [58].

Parametric amplification relies on the periodic modulation of a system parameter via some kind of nonlinearity. The nonlinearity that we will deal with is the current-dependent kinetic inductance intrinsic to the superconducting TL. An amplifier, that makes use of the kinetic inductance nonlinearity, is known as traveling wave parametric amplifier (TWPA) and has underlying operation basics similar to those in optical parametric amplification. The latter makes use of the Kerr nonlinearity, that modulates the intensity-dependent refractive index of the fiber [59].

2.3.1 Four-wave mixing

In both microwave and optical cases, propagating waves with different powers get coupled (mixed) through Kerr nonlinearity [60]. This process is called four-wave mixing (FWM). As the name suggests, FWM process is the mixing of four photons $2\omega_p = \omega_s + \omega_i$, where two photons from a strong Pump tone with a frequency ω_p are annihilated to be simultaneously created at symmetrically spaced sideband frequencies ω_s, ω_i , resulting in an amplified Signal tone. We will constrain ourselves to the case of degenerate or single-pumped FWM process, involving only three waves. More specifically, two photons with identical Pump frequency $\omega_{p1} = \omega_{p2} = \omega_p$ are mixed with a weak Signal tone ω_s , resulting in two sidebands; the first for the amplified Signal ω_s and the second for the Idler tone ω_i . We will assume that Signal and Idler tones are not degenerate $\omega_i \neq \omega_s$ (Fig. 2.9).

To demonstrate the elementary picture of traveling wave parametric amplification, we note that the sum of Signal and Idler can be presented as an amplitude modulated wave with a carrier frequency exactly matching ω_p (see Fig. 2.9):

2. Concepts

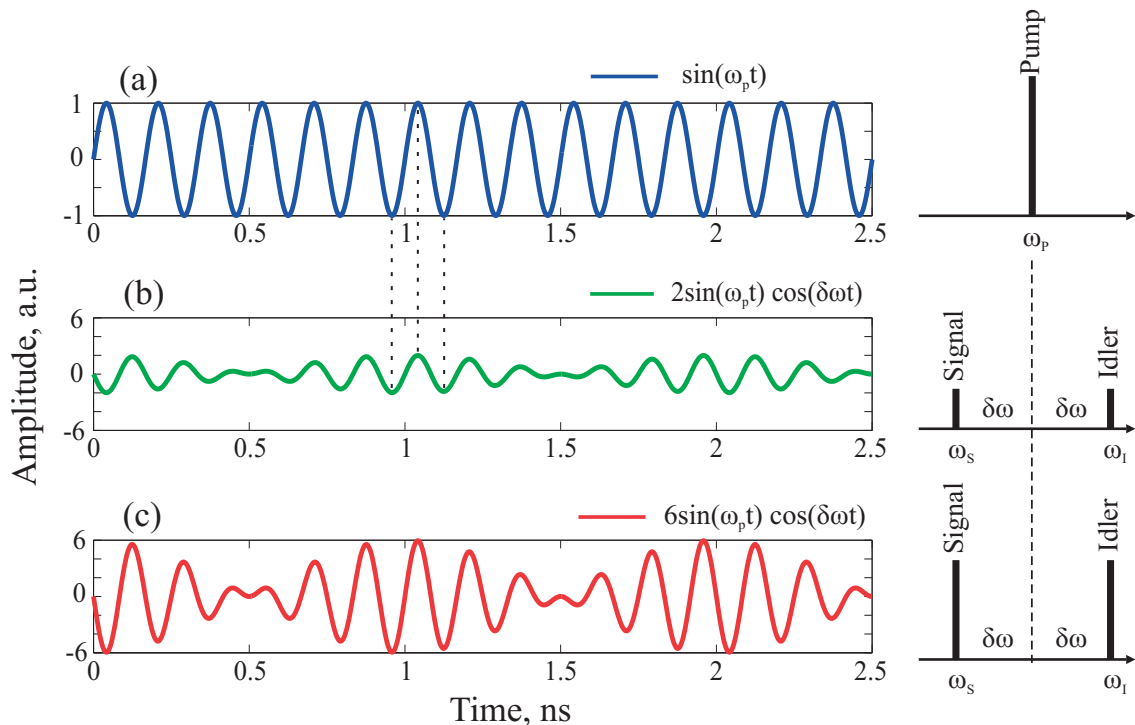


Figure 2.9: The elementary picture of parametric amplification in TWPA and the concept of FWM. (a) The curves are plotted for $\omega_p/2\pi = 6$ GHz. (b) For 2 photons annihilated at a strong Pump tone, 1 photon is created at a weak Signal and 1 photon is created at an Idler tone. $\delta\omega/2\pi = 0.5$ GHz. The sum of Signal and Idler waves is shown in green. (c) The amplified carrier of the sum of the sidebands shown in red, resulting in the amplification of Signal and Idler waves.

$$\sin((\omega_p - \delta\omega)t) + \sin((\omega_p + \delta\omega)t) = 2 \sin(\omega_p t) \cos(\delta\omega t). \quad (2.50)$$

According to Eq. (2.50), two sidebands are created at frequencies $\omega_s = \omega_p - \delta\omega$ and $\omega_i = \omega_p + \delta\omega$ as a result of a slow $\delta\omega$ signal modulating the amplitude of a carrier wave ω_p (shown in Fig. 2.9 (b)). When the strong Pump tone (Fig. 2.9 (a)) and the carrier of the Signal/Idler combo in Fig. 2.9 (b) are synchronized, both having identical frequency and phase, parametric amplification takes place. The strong Pump tone modifies the line KI in TWPA. By changing KI in a synchronized manner, the strong Pump boosts the carrier amplitude of the Signal/Idler combo (Fig. 2.9 (c)). Accordingly, the amplitudes of Signal and Idler waves increase simultaneously, corresponding to the amplified composite wave. In a similar way, if the carrier of the Signal/Idler combo is out of phase with respect to the Pump, the combo wave will be attenuated instead of being amplified.

2.3.2 Coupled-mode theory

As we have mentioned, the Signal/Idler combo is amplified if it is in phase with the strong Pump tone at $\omega_p = (\omega_s + \omega_i)/2$. However, due to a nonlinear media the strong Pump and the Signal/Idler combo have different propagation velocities. This means that even if the Signal and the Pump are properly synchronized at the entry port, they will lose synchronization with respect to each other when propagating across the line, accumulating a nonlinear phase shift. The nonlinear phase shift they acquire must be compensated with a so-called, 'dispersive' phase shift. To compensate for the power-dependent shift in order to have efficient parametric amplification, a proper dispersion engineering is needed.

A standard coplanar line is dispersion-free due to translational symmetry and to arrange a dispersion engineering one must periodically perturb the propagation velocity. Introducing a dispersion into the device structure results in frequency-dependent propagation velocity, thus the waves acquire an additional dispersive phase shift. When the dispersive and nonlinear phase shifts cancel each other, the mixing process gives rise to a maximum gain. Otherwise, the phase matching will be lost and the gain will be suppressed (see section 2.3.3).

The nonlinear phase shift is possible to derive from the wave equation for current in the coplanar TL [24].

$$\frac{\partial^2 I}{\partial z^2} - \frac{\partial}{\partial t} [L(I)C \frac{\partial I}{\partial t}] = 0, \quad (2.51)$$

where $L(I), C$ are TL inductance and capacitance per unit length. $L(I)$ is given by:

$$L(I) = L(0) \left(1 + \frac{I^2}{I_*^2}\right). \quad (2.52)$$

We search for a solution in a form of three co-propagating waves, so that the total current can be expressed in terms of the sum of different frequency components:

$$I = \frac{1}{2} \left(\sum A_n(z) e^{i(\beta\omega_n z - \omega_n t)} + c.c. \right), \quad (2.53)$$

where $c.c.$ is the complex conjugate, z is the coordinate along propagation, $n \in \{P, S, I\}$ and A_n corresponds to A_P, A_S, A_I Pump, Signal and Idler mode am-

2. Concepts

plitudes. Each wave is characterized by a propagation constant $\beta = \omega/\nu_p$ and an amplitude $A_n(z)$. The coupled-mode theory is based on a slow-varying amplitude approximation, which assumes that the wave amplitudes do not change significantly on the scale of the wavelength, namely A_P, A_S, A_I satisfy

$$\left| \frac{d^2 A_n}{dz^2} \right| \ll \left| \beta \omega_n \frac{dA_n}{dz} \right|. \quad (2.54)$$

Inserting Eq. (2.53) and (2.52) into (2.51), and neglecting the higher frequency tones $(2n + 1)\omega_p$, we will arrive at the following coupled-mode equations [59–61].

$$\frac{dA_P}{dz} = i\gamma[(|A_P|^2 + 2(|A_S|^2 + |A_I|^2))A_P + 2A_S A_I A_P^* e^{i\Delta\beta z}], \quad (2.55)$$

$$\frac{dA_S}{dz} = i\gamma[(|A_S|^2 + 2(|A_P|^2 + |A_I|^2))A_S + A_I^* A_P^2 e^{-i\Delta\beta z}], \quad (2.56)$$

$$\frac{dA_I}{dz} = i\gamma[(|A_I|^2 + 2(|A_S|^2 + |A_P|^2))A_I + A_S^* A_P^2 e^{-i\Delta\beta z}], \quad (2.57)$$

where $\Delta\beta = \beta_S + \beta_I - 2\beta_P$ is the wave propagation constant mismatch and $\gamma = \beta\omega_n\alpha/2I_*^2$ is the nonlinearity coefficient and $\alpha = L_k/(L_k + L_m)$ is the ratio of kinetic to total inductance. Substituting $A_n(z) = \sqrt{P_n(z)}e^{i\theta_n(z)}$ into Eq. (2.55-2.57), where $P_n(z)$ is the propagating power associated with the corresponding wave and $\theta_n(z)$ is the phase, Eq. (2.55-2.57) can be rewritten as:

$$\frac{dP_P}{dz} = -4\gamma\sqrt{P_P^2 P_S P_I} \sin(\theta_{rel}), \quad (2.58)$$

$$\frac{dP_S}{dz} = \frac{dP_I}{dz} = 2\gamma\sqrt{P_P^2 P_S P_I} \sin(\theta_{rel}), \quad (2.59)$$

$$\begin{aligned} \frac{d\theta_{rel}}{dz} &= \Delta\beta + \gamma(2P_P - P_S - P_I) + 2\gamma\sqrt{P_P^2 P_S P_I} \left(\frac{1}{P_S} + \frac{1}{P_I} - \frac{2}{P_P} \right) \cos(\theta_{rel}), \\ \theta_{rel} &= 2\theta_P - \theta_S - \theta_I \end{aligned} \quad (2.60)$$

Assuming a strong Pump and weak Signal/Idler waves, we can use the undepleted pump approximation $d|A_P|/dz = 0$ and neglecting the last term in $d\theta_{rel}/dz$ ($\theta_{rel} = \pi/2$ close to the phase-matched condition); we arrive at the condition for

perfect phase matching:

$$k \equiv \Delta\beta + 2\gamma P_P = 0, \quad (2.61)$$

where k is the phase mismatch parameter, $\Delta\beta$ represents the dispersive propagation mismatch and $2\gamma P_P$ is the nonlinear phase shift. From Eq. (2.61) is evident that the perfect phase matching condition will be fulfilled if the nonlinear and dispersive shifts cancel each other.

Initially having only Pump and Signal tones with arbitrary phases at TWPA input allows to create a phase-insensitive amplification [61]. The Idler that is formed during wave propagation from amplified vacuum fluctuations, has a phase such that the total phase difference θ_{rel} stays constant.

2.3.3 Parametric gain

The gain resulting from FWM process is called parametric gain. An expression for Signal tone parametric gain can be derived in terms of k phase mismatch parameter (Eq. (2.61)) [59–62]:

$$G_s = 1 + \left(\frac{\gamma P_P}{g} \sinh(gL)\right)^2, \quad (2.62)$$

where L is the amplifier TL length and g is the gain coefficient given by

$$g = \sqrt{(\gamma P_P)^2 - \left(\frac{k}{2}\right)^2}, \quad (2.63)$$

valid for $P_P \gg P_S, P_I$.

We can differentiate two special cases that highlight the importance of phase matching for the amplification efficiency.

- **Exponential gain**

In case of perfect phase matching, from Eq. (2.61), $k = 0$, $g = \gamma P_P$, and thus,

$$G_s \simeq \sinh^2(\gamma P_P L) \simeq \frac{1}{4} e^{2\gamma P_P L} = \frac{1}{4} e^{2\Delta\theta}, \quad (2.64)$$

where $\Delta\theta$ is the nonlinear phase shift of the Pump signal (given by Eq. (2.68)). The nonlinear phase shifts of Signal and Idler tones are twice that

2. Concepts

for the Pump tone. We can identify that only when linear and nonlinear phase shifts cancel out $\Delta\beta = -2\gamma P_P = -2\Delta\theta/L$, the parametric gain grows exponentially with the amplifier length L .

- **Quadratic gain**

In case of no linear phase shift (a uniform, dispersion-less superconducting line), $\Delta\beta = 0, k = 2\gamma P_P, g = 0$, the Taylor expansion of $\sinh(x)$ will yield in much lower G_s which is approximately quadratically dependent on the nonlinear phase shift:

$$G_s \simeq 1 + (\gamma P_P L)^2 = 1 + (\Delta\theta)^2. \quad (2.65)$$

2.3.4 Nonlinear phase shift in TWPA

As discussed earlier in Section 2.2.3, the kinetic inductance can also be tuned by passing dc bias current through TWPA TL. For fitting the KI nonlinearity data (nonlinear phase shift $\Delta\theta$ vs dc current) of our TWPA line, it will be useful to derive an expression for $\Delta\theta$ through dc current-proportional nonlinearity of KI, $L_k \sim I^2$.

From Eq. (2.49) and Eq. (2.8), the propagation velocity can be rewritten as:

$$v_p \approx v_p(0) \sqrt{\frac{\alpha}{1 + (I/I_*)^2}}. \quad (2.66)$$

On the other hand, the electrical length (total input-output phase shift) of the amplifier TL is given by [24]

$$\theta = \frac{2\pi L f}{v_p} \sim \frac{\theta_0}{\sqrt{\alpha}} \sqrt{1 + (I/I_*)^2}. \quad (2.67)$$

Assuming $L_k \gg L_m$ and $\alpha \sim 1$, after rearranging Eq. (2.67) and Taylor expanding $\sqrt{1+x} \approx 1 + \frac{x}{2}$, we will end up with the nonlinear phase shift as a function of dc current in the TWPA line:

$$\Delta\theta = \frac{\theta}{2} \left(\frac{I}{I_*}\right)^2. \quad (2.68)$$

2.3.5 Phase Matching

The phase matching in TWPAs is implemented through dispersion engineering. To understand the dispersion engineering in our case, it is constructive to discuss first more simple examples.

The theory behind dispersion engineering is explained with the Bragg's law for crystals [63, 64]. According to the Bragg's law, the waves incident to the crystal get reflected by atoms located in lattice planes separated by distance d from each other. Consider two neighboring atoms shown in Fig. 2.10 (a): if the phase shift between reflected waves from the first and the second atom is an integer multiple of the radiation wavelength, then the waves will interfere constructively. As a result, for specific incident angles and wavelengths satisfying the condition $2d \sin(\theta) = n\lambda$, the crystal will produce intense cumulative reflected radiation from all crystal planes simultaneously.

- **Electrons in solids**

The electrons within solids are subject to an array of periodic potential with a period a caused by atoms in a lattice (shown in Fig. 2.10 (b)). The Bloch's theorem predicts a periodic electron wave function for a periodic potential of the following form [65]:

$$\psi(x) = U(x)e^{ikx}, U(x) = U(x + a), \quad (2.69)$$

where k is the wave number and U is the periodic potential. Taking into account the Bloch's theorem, one can solve the Schrödinger equation only for a propagation across a single period of the periodic potential. Next, with the Kronig-Penney potential model [65, 66], which approximates the lattice potential with an array of periodic rectangular potentials (shown in Fig. 2.10 (b)), it is possible to find a propagation matrix for a single unit of the rectangular potential array, which relates the amplitudes of waves on the left side of the barrier to the amplitudes of waves on the right side of the barrier. Having a propagation matrix for a single barrier, one can find the electron transmission probability through the rectangular array from the total propagation matrix for N barriers.

2. Concepts

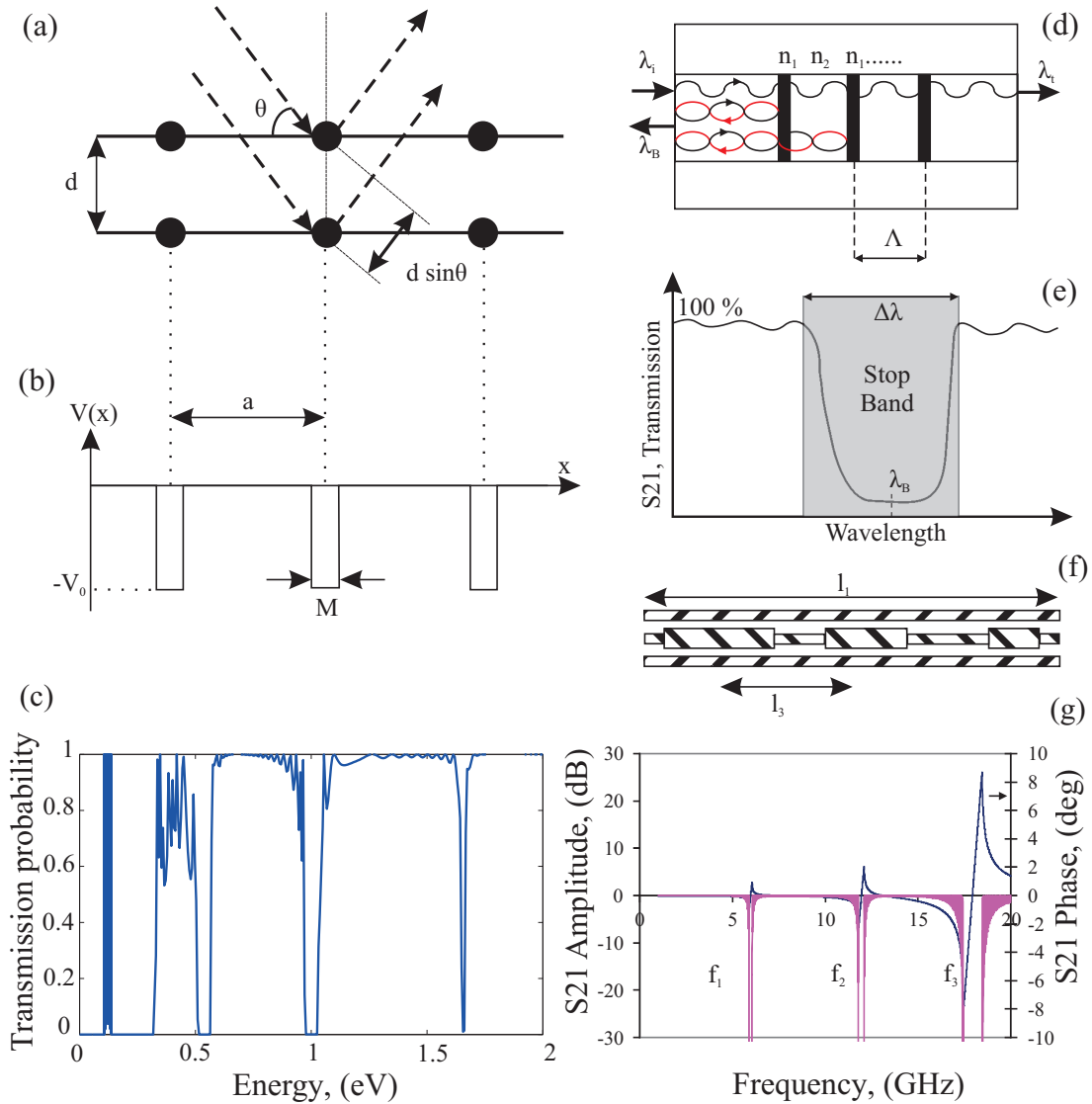


Figure 2.10: (a) Bragg reflection from atoms in a crystal lattice. (b) Kronig-Penney rectangular potential barriers representing atoms in a crystal lattice. (c) Calculated transmission probability as a function of electron energy in a periodic potential, electronic stop bands are the result of cumulative Bragg reflection from multiple barrier boundaries. (d) A sketch of a fiber Bragg grating: wavelengths that satisfy the Bragg condition will get reflected creating a stop band in the transmission spectrum. (e) A sketch of the wave transmission through a Bragg grating: the photonic stop band is centered around λ_B . (f) An illustration of a dispersion engineering by periodic loading of TL with widened sections. (g) Simulated transmission and phase of TWPA TL with Microwave Office. Stop bands at different frequencies are the result of different dispersion loading periods l_1, l_3 .

The calculated transmission probability is depicted in Fig. 2.10 (c)¹. An essential feature in this diagram is the alternating transmission and reflection regions that create bands in energy. Due to Bragg reflection on potential barriers, there are no propagating waves across the lattice for certain wave numbers, resulting in forbidden bands in the energy spectrum. It can also be noted that there exist transmission oscillations which are related to the interference of consecutive reflected waves from potential boundaries. The stop bands get deeper with increased number of barriers, as the cumulative interference effect of Bragg reflected electrons will be intensified.

- **Fiber Bragg gratings**

The concept of Bragg's law applies to a related example in optics as well: the Bragg grating. It is a dispersion compensator, a section of a fiber made of alternating layers of high and low refractive index materials, shown in Fig. 2.10 (d). The Bragg's law dictates which frequency waves will get reflected from the refractive index steps and will join the other backward traveling waves with constructive interference. All other frequencies that are non-commensurate with the grating period, will be transmitted [67]. The reflection condition in this case becomes $\lambda_B = 2n_{eff}\Lambda$, where n_{eff} is the effective refractive index and Λ is the grating period. The resulting stop band in the transmission spectrum looks like the one in Fig. 2.10 (e). The central position of the band is defined by λ_B , while the bandwidth is defined by refractive index contrast $\Delta\lambda \sim \delta n\lambda_B$ and the depth of the band is proportional to the number of grating periods. Essentially, via shifts in Λ, n_{eff} caused by the device under test, Bragg gratings can sense temperature and strain [68, 69].

¹Calculation was done in Matlab, for 100 rectangular potential barriers with $M = 1$ nm width, $a = 1$ nm barrier separation and $V_0 = 0.3$ eV height. The calculated transmission probability fits the Kronig-Penney model in the δ -function limit $M \rightarrow 0, V_0 \rightarrow \infty$.

2. Concepts

- **Dispersion engineering in a TL**

As discussed earlier, the dispersion engineering can be achieved by introducing a periodic reflection pattern. In a coplanar line, one way to introduce reflection is to arrange an impedance step (Fig. 2.2). To obtain phase matching through dispersion engineering in an amplifier line, the central strip is loaded with periodically widened sections, that locally perturb the line impedance and propagation velocity (Fig. 2.10 (f)). For the same reasons as described in the above two examples, such periodic impedance steps give rise to stop bands for microwaves in the transmission spectrum. For example, the largest period l_1 , containing all three loading elements, forms the first band at $f_1 = \nu_p/2l_1$ and its harmonics at $f_2 = 2f_1, f_3 = 3f_1$. The smallest period $l_3 = l_1/3$ forms the highest frequency band at $f_3 = 3f_1$ and its harmonics at $2f_3, 3f_3$ ¹. The number of dispersion elements defines the depth of the bands, while the length and the width define how wide the bands will be. The design challenge of dispersion engineering is to achieve significant dispersive phase shift at frequencies approaching but not falling in the stop band. By tuning the Pump frequency f_P to be in a transmissive region, i.e. in the vicinity, but not inside the bands, it is possible to balance the nonlinear and dispersive phase shifts in the device.

¹The need for two distinct dispersion engineering periods for TWPA will be explained later in section 5.5.

Chapter 3

Near Field Scanning Microwave Microscopy

This chapter aims to explain how microwave reflectometry is deployed in NSMM technique and will motivate the need for a thin film TL superconducting resonator as a near field scanning probe in section 3.1. In order for microwave probes to become a useful tool for the characterization of materials used in quantum devices, several major problems must be solved and we will go through these challenges in section 3.2. In section 3.3 we will introduce the basic slow propagation line design that will serve as a base for developing a fractal resonator as a microwave probe. We will briefly describe the fractal resonator design considerations and the fabrication steps as well as our cryogenic home-build AFM/NSMM system with integrated fractal resonator as a scanning probe in section 3.5.1. The important results will be discussed in section 3.6 and the chapter will be summarized in section 3.7 (Paper I).

3.1 Introduction

After defining the main building blocks of c-QED experiments, TLs and TL resonators, we can proceed with introducing the microwave techniques that make use of them.

With the advent of STM [4] and AFM [5], a number of hybrid techniques

3. Near Field Scanning Microwave Microscopy

based on STM, AFM were investigated with added possibilities to map extra useful information about material properties, such as impedance (capacitance [70], resistance [70, 71]), dielectric properties [72], etc. Such mapping, however, is usually not as straightforward as topography imaging because in many cases, these properties are related to buried structures not directly shown on the surface. It calls for some innovative approaches to 'see through' with sufficient sensitivity and resolution. One such approach is the near field microscopy that operates with a microwave probe within a distance from the radiation source significantly shorter than the wavelength. Near field microscopy has been applied for material characterization in various research fields [16, 73].

The operation principle of NSMM is based on the electromagnetic interactions of the sample under test and the microwave energy confined in the near field proximity to the scanning tip. If the sample is within the near field zone from the tip, then sample local electromagnetic properties can be estimated from the perturbed near field pattern of the tip.

Its challenging to integrate a distance control mechanism with a near field scanning tip. In different near field microscopes the scanning tip was formed with various field concentrating features like STM tip terminating a TL resonator [74], TL tip attached to AFM cantilever [75] or a sharpened electric wire attached to a Tuning Fork (TF) [76]. In the next section we will motivate our choice of TF-based distance control mechanism.

TF-based AFM/NSMM

Our long term goal is to study dielectric materials comprising solid-state quantum devices. The loss mechanisms lying behind the defects in these dielectrics (two-level fluctuators (TLFs)) cause decoherence by coupling to engineered two-level systems (TLSs) [39, 42]. The quality assurance of losses and dielectric properties of these materials will give a very valuable feedback. We shall find a way to study loss mechanisms and properties of these dielectrics. As TLFs have excitation spectrum with typical energies in microwave range, our near field probe must also operate in the same range [77]. Thus, a microwave TL resonator as a near field probe could be the best choice for this purpose.

3. Near Field Scanning Microwave Microscopy

An ultimate goal is to coherently study a single TLF without saturating it. For this, we shall have low microwave powers in our probe and ultimately we shall operate the resonator in a near-single photon regime. This can be achieved with a microwave high-Q superconducting resonator as a probe, as the high-Q will translate into greatly reduced excitation powers. Moreover, the high-Q will translate into a high microscope sensitivity [78].

The high-Q microwave probe made of a superconducting resonator needs to be measured at low temperatures (4 K). Also, the microscope must be cryogenic (0.3 K), such that $\hbar\omega \geq k_B T$ [79].

To diagnose dielectric properties (losses, capacitance), we must be able to follow the sample surface topography and that is why we would like to combine our microwave probe with some kind of AFM. However, it is a big challenge to separate the topography signal from the microwave signal. This challenge must be confronted.

AFM is an established technique for characterizing conducting sample surface topographies with nanoscale resolution. It is important to characterize quantum samples non-invasively, i.e. without snapping the tip into the sample. This implies that a cantilever-based AFM should operate in a tapping mode. The tapping mode allows to gently detect repulsive Coulomb interactions and attractive van der Waals forces, reducing the damage to the sample. However, the cantilever is light and can not handle any extra mass attached to it to form the probe/tip. The only way of mechanically non-invasive characterization thus reduces to the TF-based distance control operating in a non-contact mode [80]. In contrast to cantilevers, TF is much stiffer (high spring constant ~ 1000 N/m) and can handle large tip-sample forces without snapping the tip into the sample. Another advantage is that TF is compact (4 mm long) and can be used in a cryogenic microscope. Also, if the microwave resonator probe/tip is made compact enough, it can be directly mounted on one prong of the TF.

Piezoelectric TF's are mechanical devices. With an applied ac voltage to the TF, prongs start to oscillate with a typical resonance frequency of ~ 32 kHz. The tip-sample interaction causes a TF oscillation frequency shift Δf_{TF} . The AFM feedback loop tries to maintain $\Delta f_{TF} = \text{const}$ by adjusting the tip-sample distance so that the distance also stays constant.

3. Near Field Scanning Microwave Microscopy

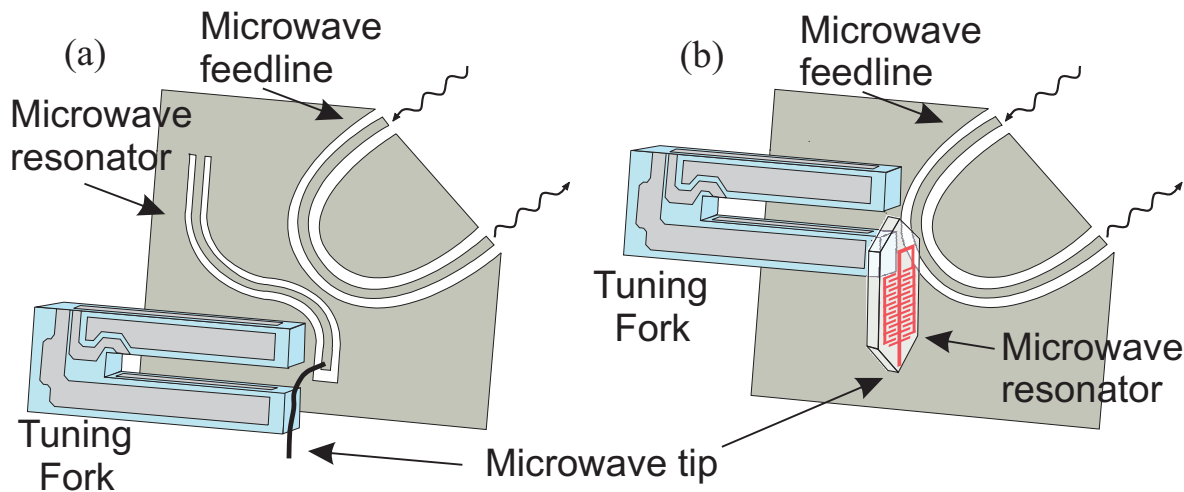


Figure 3.1: The sketch of NSMM microscope based on a TF AFM distance control. Microwave feedline is a CPW on a separate chip. (a) Microwave resonator is a CPW coupled to the feedline on the same chip. The scanning tip is a Nb wire extended from the resonator and glued on the TF prong. (b) Microwave fractal resonator is directly mounted on a TF prong to form the scanning probe. The resonator edge is dedicated for a scanning tip. The coupling between the microwave resonator and the feedline is tunable.

Our first implementation of NSMM, combined with a TF-based distance control, had a $\lambda/2$ CPW resonator placed on a separate chip decoupled from the TF. A Nb wire, to be used as a microwave near field tip, was bonded at one end of the resonator and was glued on a TF prong (shown in Fig. 3.1 (a)). Such a long wire acted as an antenna dipole and radiated. Radiation losses resulted in low probe Q-factors (~ 1000). This drastically reduced the sensitivity. An ideal probe would be a compact TL resonator, integrated with a scanning tip, which would not radiate and at the same time would not affect itself on the TF Q-factor when directly mounted on it, as shown in Fig. 3.1 (b)¹.

In summary, the high spatial resolution of AFM, together with the sensitivity of high-Q CPW resonator operating at ultra-low probe powers could be the perfect combination for our needs - non-invasive characterization of engineered TLSs and spurious TLFs. To the best of our knowledge, at the time of working on this project, there existed no such scanning microscope with all the above

¹If the TF center of mass is broken due to extra mass attached to its prong, the TF Q-factor typically degrades below 100 once the loaded mass approaches the mass of the prong.

functionalities at the same time in literature.

3.2 Challenges to be addressed in NSMM

- Development of a high-Q microwave probe operational at close to single photon powers.
- Development of a miniature and light-weight CPW resonator probe to be directly integrated on a TF prong.
- Integration of a near field scanning tip with the microwave resonator probe at its voltage antinode, where the electric field is at maximum.
- Tip sharpening to ensure high NSMM microwave resolution.
- Coupling of a separate feedline chip to the resonator at its current antinode, preferably with the possibility of tunable coupling.

3.3 A slow propagation line for NSMM

We found it beneficial to implement a slow propagation transmission line to overcome the challenges mentioned previously. As the name suggests, slow propagation line has lower propagation velocity (compared to conventional CPW TLs). Because the wave propagation velocity is inverse proportional to per unit length capacitance of the TL, $\nu_p \sim 1/\sqrt{LC}$, an increased capacitance slows down the wave propagation in the TL. We obtain this via a design with a quasi-fractal interdigitated capacitance in between two inductors (Fig. 3.2 (a)). Each unit cell in a fractal design has primary, secondary, tertiary, etc. branches, which maximize the per unit length capacitance of the TL. The basic unit cell, shown in Fig. 3.2 (b), periodically repeats itself on a large scale forming the whole resonator. The red and blue lines in Fig. 3.2 (b) join on one end of the fractal line, thus making a resonator electrically resembling a U-shaped mechanical TF like in Fig. 3.2 (d-f).

A clear advantage of a slow wave propagation velocity is that it enables to significantly shorten the length and weight of TL microwave resonator ($\nu_p = \lambda f$),

3. Near Field Scanning Microwave Microscopy

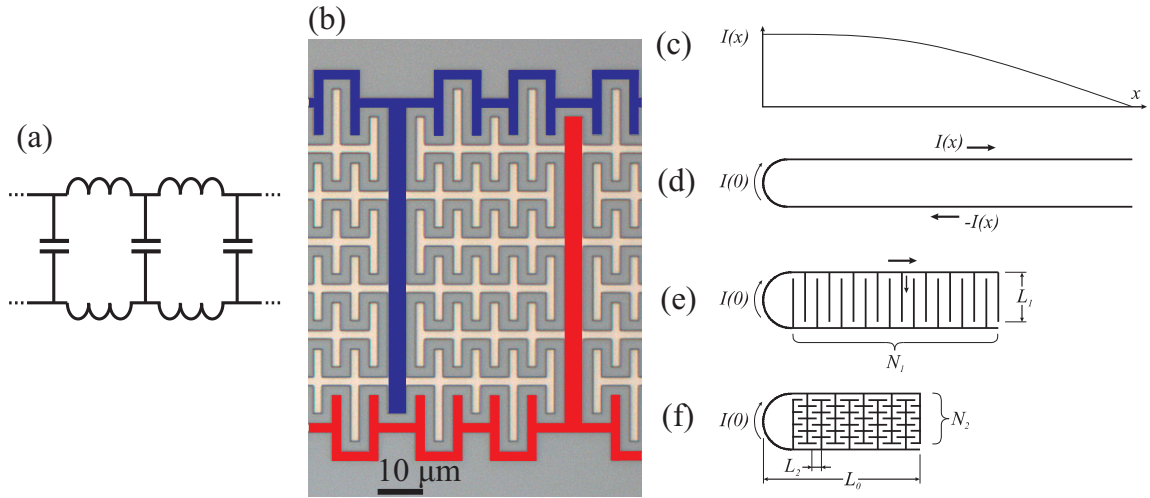


Figure 3.2: (a) The lumped element representation of a section of fractal design. (b) A fractal design, comprising a section of a slow propagation line, used in microwave resonators for scanning. One prong is colored in red, the other in blue. The structure is folded as a mechanical TF and the area in-between prongs is filled with a fractal capacitance. (c-f) Evolution of a U-shaped $\lambda/2$ structure into a fractal design, where the resonance frequency is kept the same for all iterations. (c) The current distribution along one prong of $\lambda/2$ fractal resonator. (d) $I(0)$ is the current antinode where two prongs join. (e) The second order fractal iteration with N_1 secondary branches. (f) 4th-order fractal design with N_2 sub-branches. The final length L_0 is ten times reduced. Sketch not to scale.

(Fig. 3.2 (f)). This facilitates the development of more compact scanning probes. Furthermore, compactness makes it easier to control radiation losses.

3.4 Fractal resonator design concepts

The fundamental principle of the fractal resonator, to be implemented as a microwave scanning probe, is that it is a simple U-shaped structure, folded so that voltage antinodes meet each other on one end, resembling a mechanical TF with two ‘prongs’ (Fig. 3.2 (c,d)). The resonator with two $\lambda/4$ prongs supports a $\lambda/2$ mode (Fig. 3.3 (a)). The area in between resonator prongs is filled with a capacitor. The capacitor is extended from an interdigital to a four-order fractal structure, as shown in Figs. 3.2, 3.3. Thanks to the increased capacitance, the wave slows down in a fractal structure. The resulting resonator length is reduced to only 1 mm.

3. Near Field Scanning Microwave Microscopy

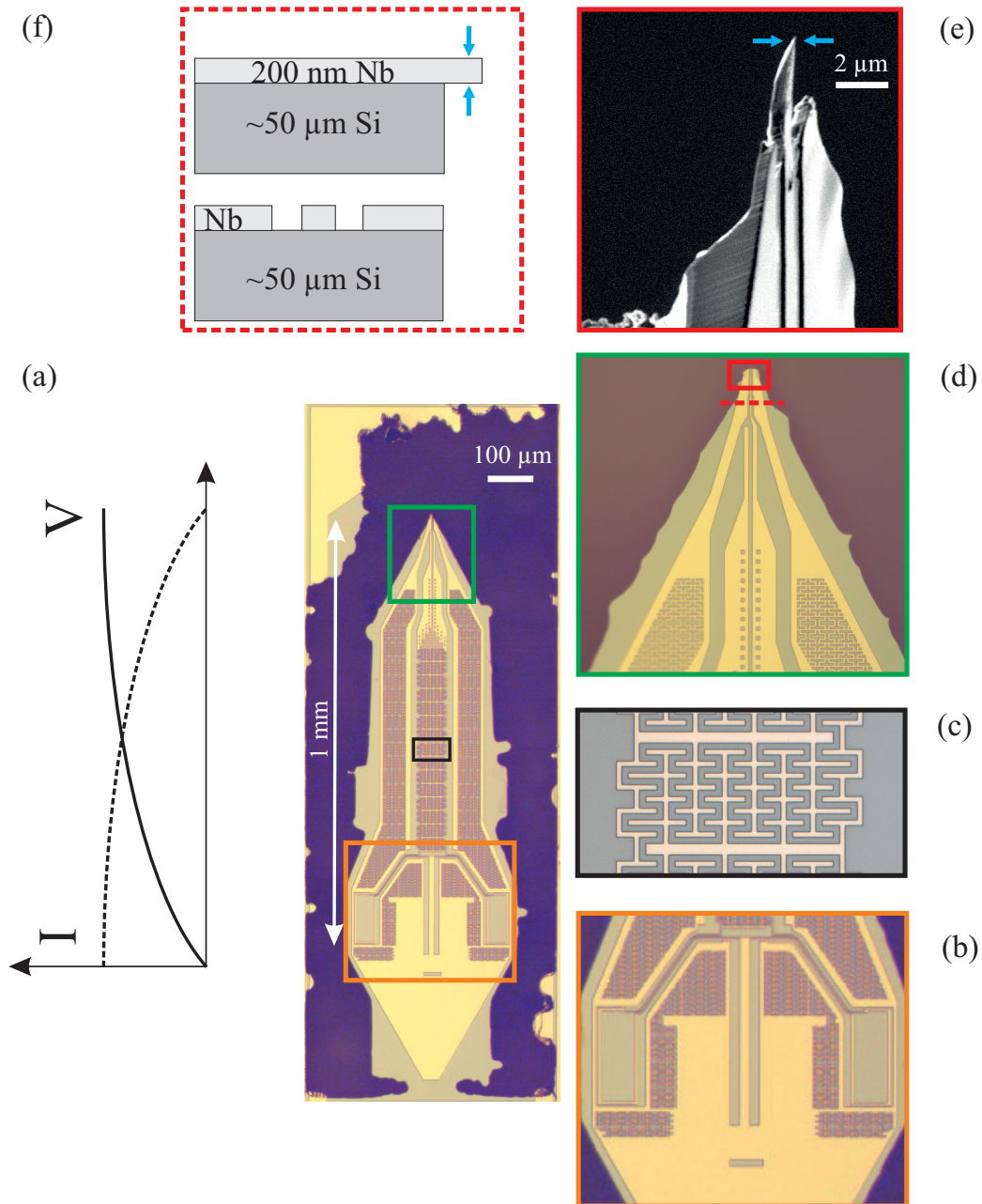


Figure 3.3: (a) Optical Microscope (OM) image of 6 GHz fractal resonator as a microwave probe with the voltage and current modes sketched for a single prong of the resonator. (b) Zoom-in on the coupling area of the resonator. (c) Zoom-in on the resonator central fractal area. (d) Zoom-in on the near field probe tip. (e) Scanning Electron Microscope (SEM) image of the tip, right after Focused Ion Beam (FIB) thin-down. (f) Cross-section across the red dotted line in (d), front view (bottom), side view (top).

3. Near Field Scanning Microwave Microscopy

The resonator end with maximum electric field is to be coupled to a near field probe. As shown in Fig. 3.3 (d), 1 prong of the resonator is extended to form the scanning tip (Fig. 3.3 (e)). The opposite side (Fig. 3.3 (b)) is to be inductively coupled to a separate microwave feeder chip. By adjusting the distance (~ 0.1 mm) between the resonator coupling loop and a nearby feedline, we can tune the coupling (sketched in Fig. 3.2 (b)). Except for the need for maximum voltage at the tip area, we chose inductive coupling, as it would be impossible to achieve strong capacitive coupling¹.

At the voltage node of the resonator, all the metallized areas are joined in a common pad which is intended for dc biasing/ground connection of the resonator. For this, a thin bonding wire is glued in the large metallized dc pad area (Fig. 3.3 (a), Fig. 3.4 (b)).

The resonator has two inductive loops opposite to each other, one for coupling to the feedline, the other as a dummy, to keep the resonator symmetry with respect to the dc pad and avoid increased radiation losses. Additionally, the resonator is surrounded with perforated ground planes to screen the tip by reducing stray capacitances. The ground plane is also needed to further suppress radiation losses. The ground plane is separated from the central fractal area of the resonator via a gap. Prong-to-ground capacitance is much lower than the prong-to-prong fractal capacitance (~ 1000 times). This ensures that the microwave currents are concentrated on the resonator itself.

3.5 Experimental Techniques

3.5.1 Microfabrication of fractal resonators for NSMM

The tip of the as-fabricated resonator (shown in Fig. 3.3 (d)) needs to be sharpened by FIB-SEM ion milling, until some section of Nb becomes free hanging with a diameter of ~ 100 nm (as shown in Fig. 3.3 (e)). As Si is much easier and faster to mill away, the resonator was fabricated on a Si substrate. The simplicity

¹For capacitive coupling one plate of the capacitor, located on the resonator and the other plate, located on a separate feedline chip, would need to be $1 \mu\text{m}$ apart. In contrast, the effective range of inductive coupling is defined by dimensions of feedline and the diameter of the coupling loop on the resonator chip ($> 10 \mu\text{m}$).

3. Near Field Scanning Microwave Microscopy

of micromachining is compromised with the relatively high loss tangent of Si as compared to sapphire.

To fabricate resonator structures, first 200 nm Nb was sputtered on Si, then patterned with e-beam and NF_3 Plasma Reactive Ion Etching (RIE). After diamond saw-cutting the wafer into chips, the top side of chips was protected with a photoresist. Then Si was thinned from the chip backside with a Bosch process ($\text{SF}_6/\text{C}_4\text{F}_8$) down to $\sim 50 \mu\text{m}$. After this, the Si in a small area around the resonator's perimeter was completely removed via patterning with Infrared-alignment photolithography and a Bosch process. This last Si etching was done in small steps to be able to monitor when the resonator surroundings are completely etched through Si and to stop the process on-time. The chip at this point looked like in Fig. 3.3 (a).

The front side view on the cross-section of the area next to resonator tip (Fig. 3.3 (d)) is demonstrated in Fig. 3.3 (f), bottom. The side view of the cross-sectional area is pictured in Fig. 3.3 (f), top. For more detailed fabrication steps, see [46].

3.5.2 Cryogenic scanning setup

The nc-AFM/NSMM microscope is mounted inside a single-shot He^3 cryostat with a base temperature of 300 mK. A simplified sketch of the nc-AFM/NSMM microscope is illustrated in Fig. 3.4. The as-fabricated fractal resonator chip is glued with stycast on one prong of the TF. Then a bonding wire is glued on the dc bias pad with a conductive cryogenic epoxy. The assembly is then placed on a separate Printed Circuit Board (PCB) with an excitation CPW feedline and the distance between them is adjusted with a differential screw so that the coupling of the microwave resonator to the feedline can be controlled. The microscope has two operation modes: nc-AFM and NSMM.

3. Near Field Scanning Microwave Microscopy

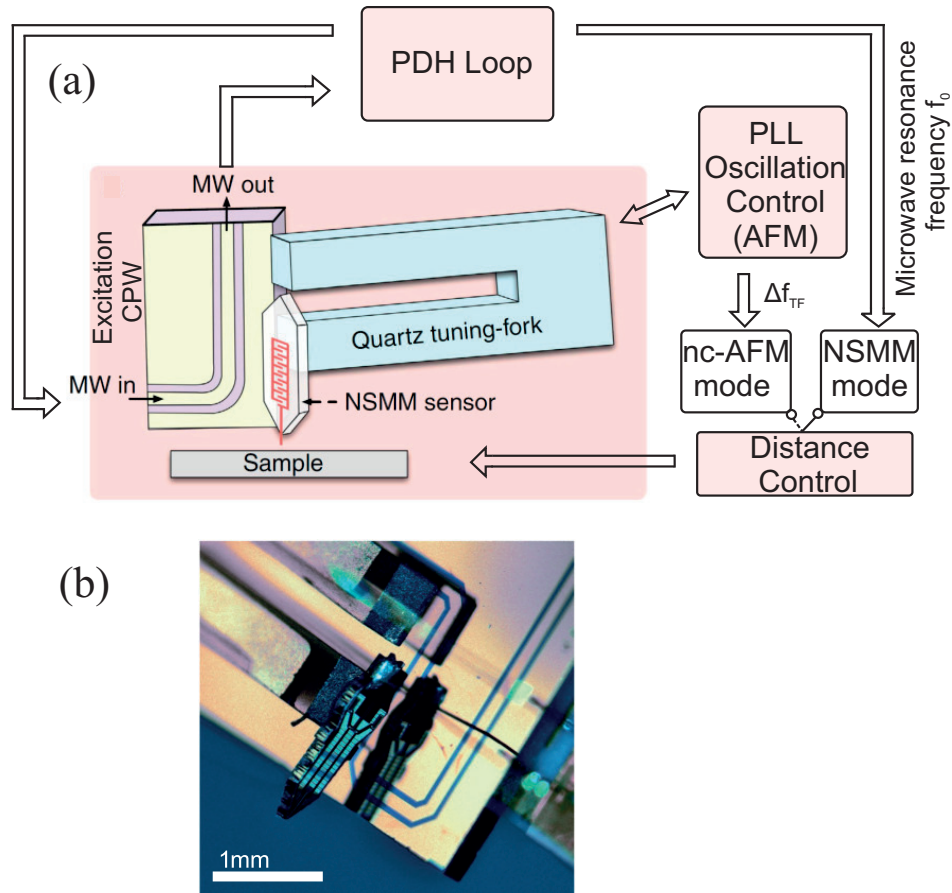


Figure 3.4: (a) The sketch of the nc-AFM/NSMM setup with two distinct operation modes: NSMM and nc-AFM. (Adopted from [77]). (b) The optical image of the microwave resonator glued on the TF prong. The assembly is mounted on top of a separate PCB with a CPW feedline.

nc-AFM mode

In the simplest case of a sample with flat topography and variable dielectric properties, in nc-AFM mode the tip will simply follow the flat topography. The Pound-Drever-Hall (PDH) system generates a signal which is proportional to a microwave resonance frequency shift Δf_0 . This signal is recorded as the microwave output.

In a more complicated case of a sample with non-flat topography, the tip will lift up/down due to topography. Phase locked loop (PLL) feedback, by keeping constant tip-sample distance, tries to maintain TF resonance frequency shifts $\Delta f_{TF} = const$. This gives a high resolution topography information. On the

3. Near Field Scanning Microwave Microscopy

other hand, due to tip movements the microwave resonance frequency will also change from point to point. Because the tip follows topography, the microwave signal given by PDH gets convoluted with topography and can not be used for estimating true microwave resolution. The detailed discussion of PDH system operation can be found in the end of this section.

NSMM mode

PLL feedback is disconnected. Only PDH feedback supplies a signal. In NSMM mode, in the simplest case of a sample with flat topography and variable dielectric properties, the tip will lift up/down to follow the microwave landscape (to keep $f_0 = \text{const}$).

In a sample with non-flat topography, the tip sample distance will vary from point to point, thus shifting the microwave resonance frequency. To compensate for these shifts, PDH feedback sends a signal to z-piezo, that adjusts the tip-sample separation to keep $f_0 = \text{const}$ [81]. By doing so, the tip non-directly will follow the constant capacitance profile of the sample and will give a microwave contrast. In this case, the microwave image does not contain sharp features coming from sudden up/down tip shifts in PLL (AFM) z-control, and the spatial resolution reflects the true microwave resolution. The microwave resolution is, in turn, defined by the tip radius and thus can be estimated.

The PDH technique

The main reason why we have chosen the PDH-loop is that it relies on phase measurements, which are much faster ($\sim 1/f_0$) than VNA with amplitude measurements ($\sim 1/Qf_0$). The second advantage of PDH-loop, as compared to conventional homodyne/heterodyne techniques, is its exceptional phase stability. The basic idea of PDH technique (and its advantage compared to standard homodyne technique) can be explained as follows: the PDH technique is similar to homodyne technique in a way that it also relies on both signal and reference. In homodyne technique, the signal and reference follow two different routes. The phase of the signal is affected by instabilities in cables/connectors (due to mechanical vibrations, temperature drifts etc.). To cancel the effect of all these instabilities, one

3. Near Field Scanning Microwave Microscopy

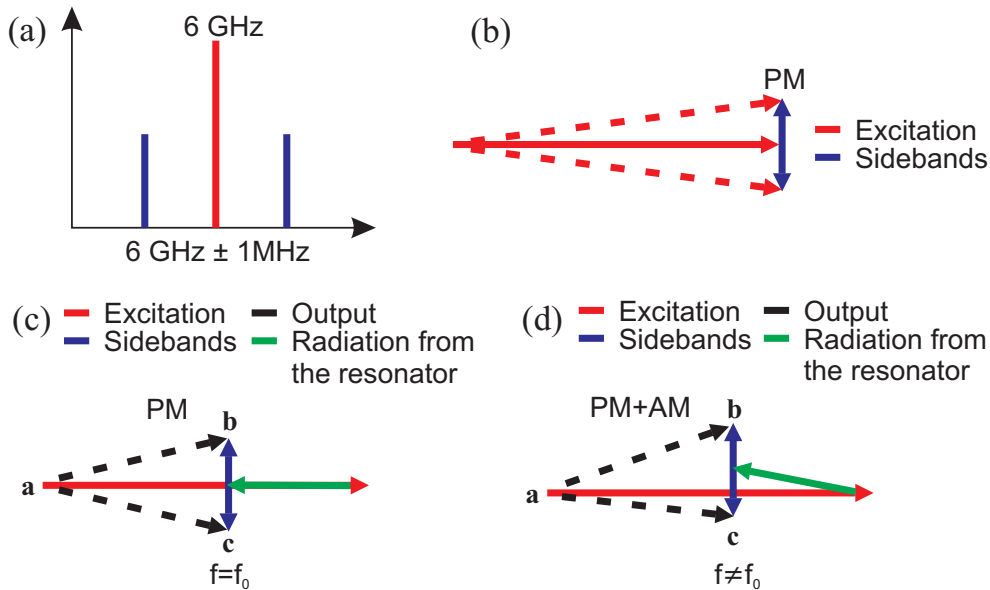


Figure 3.5: Phasor representation of different signals used in PDH locking technique. (a) The frequency spectrum of a phase modulated excitation signal centered at 6 GHz. (b) Phase modulated excitation signal in phasor representation. The carrier is shown in red, the sidebands in blue. (c) At resonance the output signal (black) is PM modulated. The output (black) is the sum of excitation (red+blue) and the signal radiated from the resonator (green). (d) Off-resonance the output signal will acquire a phase shift and will get also AM modulated ($ac \neq ab$).

should ideally pass the reference through the same route as the signal itself (then all drifts will equally shift the phases of both signal and the reference). But just passing the reference through the same route will excite the resonator. The solution is to get the reference signal PM modulated, that is, to convert a single frequency in the spectrum into two sidebands. Once the sidebands are outside the microwave resonance linewidth, they will not interact with the resonator and will not inject energy into the resonator.

In more details, the basic principle of PDH locking, demonstrated in Fig. 3.5, is the following: a phase modulated (PM) signal with a carrier at 6 GHz and two sidebands $\pm 1 \text{ MHz}$ away from the carrier is fed to the microwave resonator Fig. 3.5 (a,b). The output signal is the sum of the excitation and the signal radiated from the resonator and traveling towards the output Fig. 3.5 (c). If the excitation signal is at resonance with the resonator, then the output signal will be with constant amplitude and only phase modulated ($ab=ac$ in Fig. 3.5 (c)).

3. Near Field Scanning Microwave Microscopy

Off-resonance both the radiated and the output signals will be phase shifted with respect to the excitation, causing partial PM-to-AM conversion ($a_c \neq a_b$ in Fig. 3.5 (d)). The resulting error signal allows to easily track f_0 . The PDH feedback system locks to f_0 by minimizing the error signal.

With PDH, which detects precisely and tries to minimize any shifts from f_0 , we can read out microwave resonator frequency shift Δf_0 . The PDH system generates some voltage to shift the frequency of voltage-controlled generator, so that this frequency matches the resonance frequency of resonator. The voltage which is generated by PDH feedback system is proportional to Δf_0 and is recorded as a microwave channel signal, composing the NSMM sample image. PDH-loop allows to accurately measure f_0 by detecting shifts from f_0 with high sensitivity down to a few $\text{Hz}/\sqrt{\text{Hz}}$ and a high bandwidth (5 kHz).

3.6 Results

The Q-factors of our Nb/Si fractal resonators, when pre-measured in a He gas-flow cryostat at ~ 2 K, were of the order of $> 10^5$. Suppressed radiation losses prove the benefits of, firstly the short length of the resonator, then the intrinsic symmetry and the continuous ground plane surrounding the resonator. However, the Q-factors reduce to $\approx 15000 - 30000$ in the NSMM assembly. We assign this decrease in Q to 4 K photons generating quasiparticles in the superconductor and we expect improvement in Q-factors if the scanner would be additionally shielded at 1 K. The Q-factor of TF stayed > 5000 at low temperatures, as it was successfully loaded with the compact microwave resonator, which did not degrade its symmetry.

The fact that AFM provides nanoscale spatial resolution is well known. But what is problematic to know with conventional NSMM techniques, is the microwave resolution for samples with non-flat topography. Any step in topography shifts the tip, introducing an extra capacitive change on top of the capacitance intrinsic to the sample, thus making it impossible to resolve the true microwave response. To find out the length-scale at which microwaves were localized at the sharpened tip of our microwave probe, we scanned on a Nb sample with topographic protrusion with both nc-AFM and NSMM modes (see Fig. 3.6). In

3. Near Field Scanning Microwave Microscopy

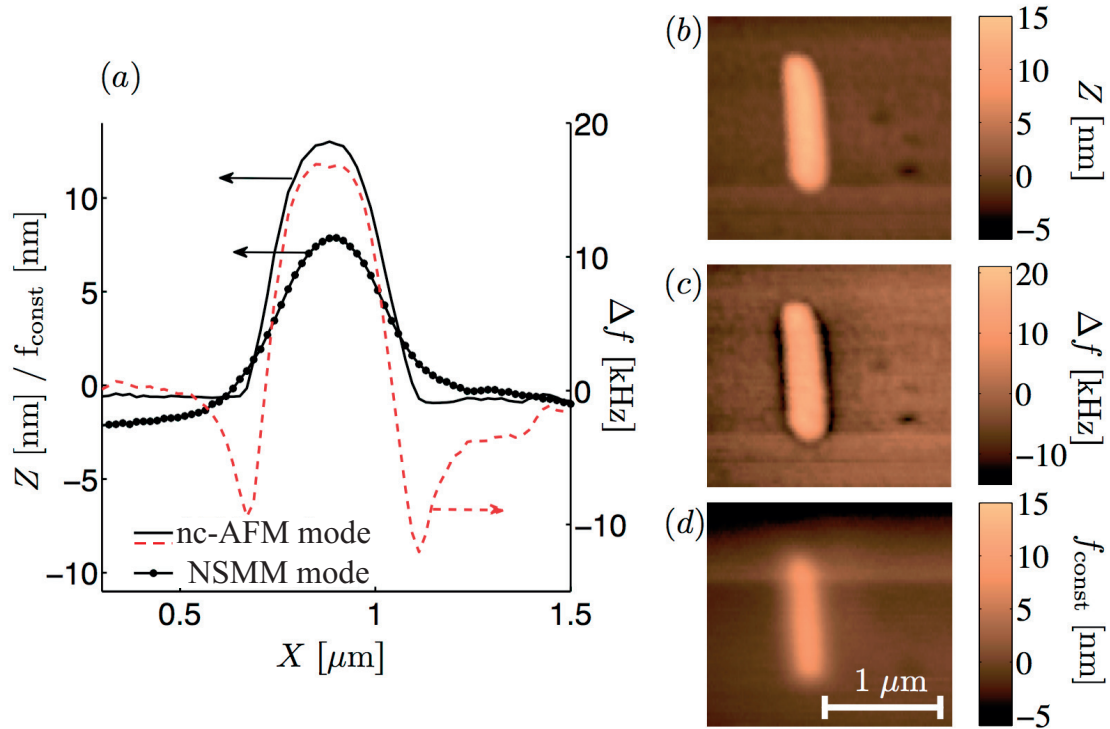


Figure 3.6: Scans on a superconducting sample with topographic protrusion. Temperature 0.5 K, scan speed $0.8 \mu\text{m/s}$, microwave power -80 dBm . (a) Line traces extracted from scans in (b,c,d). (b) Topography in nc-AFM mode. (c) Microwave frequency shift obtained in nc-AFM mode, simultaneously with (b). (d) Topography in NSMM mode comprising a surface of constant microwave frequency, or constant capacitance.

nc-AFM mode, the topography (Z) signal clearly shows the metallic protrusion with a ($\sim 20 \text{ nm}$) height contrast (Fig. 3.6 (b)). The microwave resonator frequency shift (Δf) signal, simultaneously recorded in nc-AFM mode (Fig. 3.6 (c)), is convoluted with capacitive contribution from topography, thus doesn't allow to estimate the real microwave response. In the last plot obtained in NSMM mode with a constant capacitance (Fig. 3.6 (d)), the metallic protrusion's contrast is $\sim 40\%$ lower than that in nc-AFM mode. This is simply because all the microwaves are well localized at the tip within an area that has the same dimensions as the topographic object itself, implying $\sim 250 \text{ nm}$ microwave reso-

3. Near Field Scanning Microwave Microscopy

lution¹. This further confirms that the tip apex contribution to microwave field is dominant at small tip-sample distances (< 20 nm), while the contribution of stray capacitance due to unshielded tip dipole moment is well screened by the perforated ground plane surrounding the resonator.

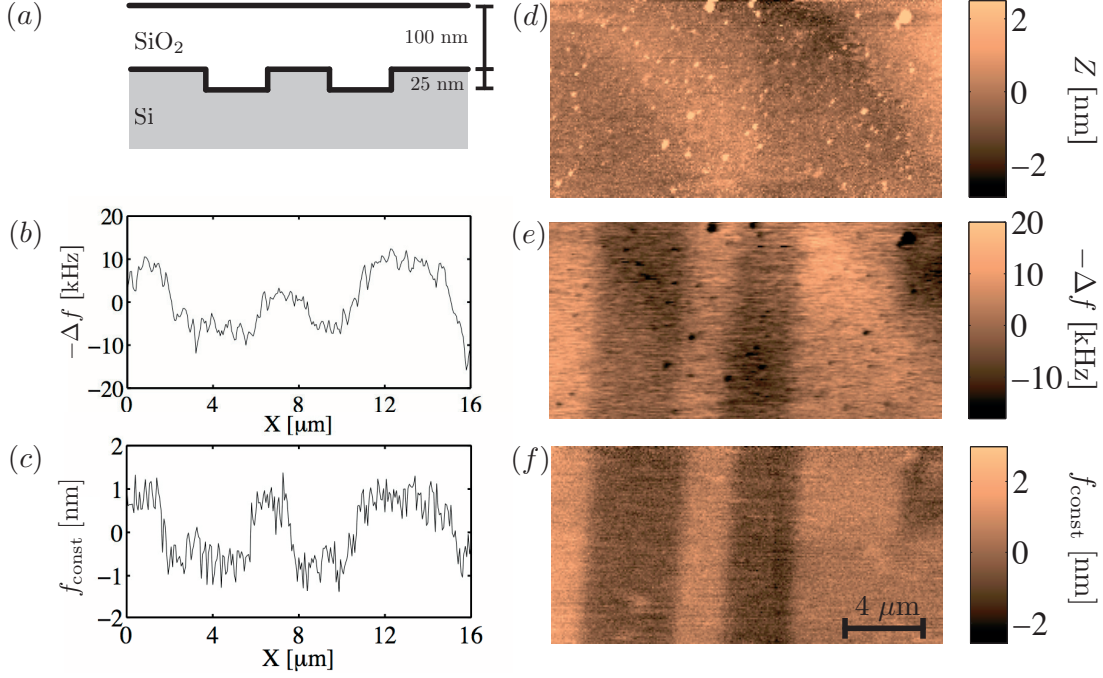


Figure 3.7: Scans on a flat sample with trenches in dielectric. Temperature 0.3 K, microwave power -70 dBm. (a) Sample cross-section. (b,c) Single line traces extracted from scans in (e,f). (d) Topography in nc-AFM mode. (e) Microwave frequency shift obtained in nc-AFM mode, simultaneously with (d). (f) Topography in NSMM mode comprising a surface of constant microwave frequency, or constant capacitance.

To evaluate the capacitive sensitivity of our microscope, a test sample has been made with a flat topography, but with a dielectric contrast. Such a sample was aiming to eliminate the contribution of topography-related capacitance variation and to get a microwave response exclusively from the capacitance embedded in the dielectric. The test sample comprised a Si substrate with 25 nm deep etched trenches and a SiO₂ deposited on top. The surface was then polished down to 100 nm (cross-section shown in Fig. 3.7 (a)). The sample was

¹To assure the same height scale and keep the same tip-sample separation, the microwave resonance frequency shift in NSMM mode was linked to that in nc-AFM mode.

3. Near Field Scanning Microwave Microscopy

scanned again in two modes. The topography and the microwave signal in nc-AFM mode is demonstrated in Fig. 3.7 (d,e), while the topography from the constant capacitance surface in NSMM mode is shown in Fig. 3.7 (f).

Directly from line traces extracted from the scans (Fig. 3.7 (b,c)), it is possible to estimate the capacitive sensitivity of our microscope. Translating the frequency shift step difference in the scan trace into capacitance, assuming a 200 nm tip radius with 10 nm tip-sample distance, we obtain 3.5 aF capacitance difference. Further, by calculating SNR for Fig. 3.7 (c) and using the pixel sampling frequency as bandwidth, the estimate of capacitive sensitivity will be $66 \text{ zF}/\sqrt{\text{Hz}}$ for -70 dBm microwave excitation power.

Another way of estimating the capacitive sensitivity is via frequency noise of the PDH loop as a sum of the residual frequency noise spectral density and mechanical noise spectral density. Converting frequency noise into capacitance

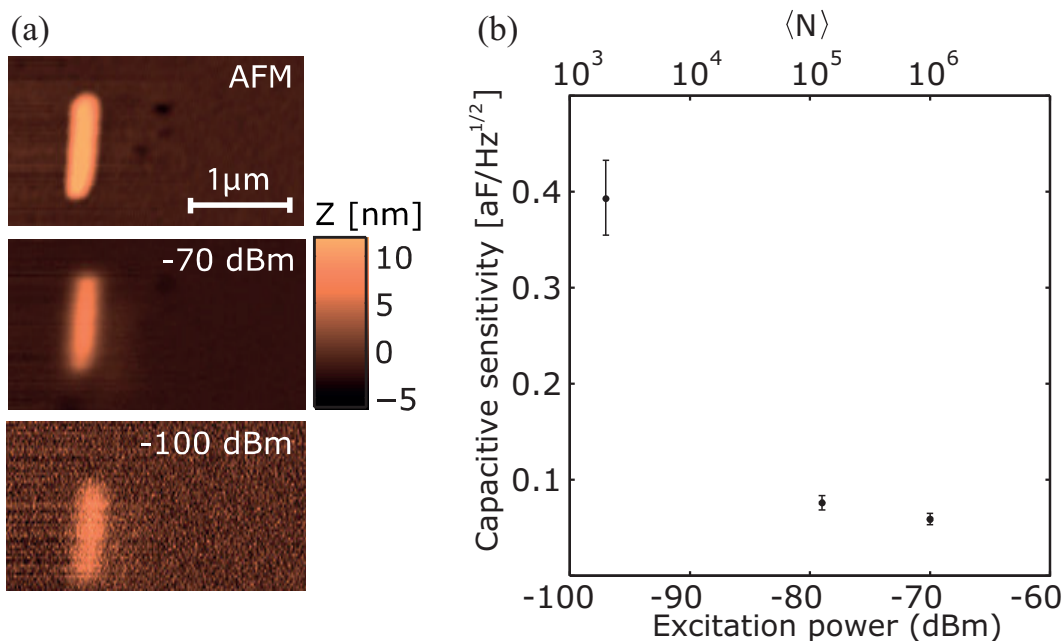


Figure 3.8: (a) Top: AFM topography of the superconducting sample with topographic protrusion. Temperature 0.3 K, scan speed $2 \mu\text{m/s}$. Middle: topography in NSMM mode, microwave power -70 dBm . Bottom: topography in NSMM mode, microwave power -100 dBm . (b) Total capacitive sensitivity of nc-AFM/NSMM microscope in NSMM mode for different excitation powers. Error bars were calculated for a fixed error in setpoint, the uncertainty in z-calibration and other constant errors in measurements of noise spectra.

noise, we get around $64 \text{ zF}/\sqrt{\text{Hz}}$ for -70 dBm power (10^5 photons in the resonator), similar to the number estimated above. At higher powers mechanical noise dominates over electrical noise. A better mechanical vibration damping would improve the sensitivity upto an order of magnitude.

With a reduced power (-100 dBm , 1000 photons), the sensitivity reduces to $0.38 \text{ aF}/\sqrt{\text{Hz}}$ (Fig. 3.8 (b)). Even with 1000 photons in the resonator, the PDH loop is stable enough to show microwave contrast on a topographic protrusion sample with the same scan speed as AFM (Fig. 3.8 (a)). At lower powers ($< 100 \text{ dBm}$), the PDH loop gets really unstable and noisy, mainly due to the high noise temperature of our low noise amplifier ($\sim 75 \text{ K}$). A quantum-limited cryogenic amplifier would solve this issue and enable nc-AFM/NSMM operation at close to single photon probe powers.

3.7 Summary & Outlook

In summary, we report on the first cryogenic nc-AFM/NSMM system with a superconducting fractal resonator as the microwave probe. Thanks to resonator compactness and suppressed radiation losses, we obtain the highest ever reported microwave probe Q-factor. The high Q-factor translates into four orders of magnitude lower probe power amplitudes ($100 \mu\text{V}$ or 1000 photons) as compared to powers in conventional NSMMs. Even with such low powers the sub-attoFarad sensitivity and nanoscale resolution stay on the same page as in state of the art microscopes [73]. This, together with TF-based nc-AFM distance control, enables both electrically and mechanically non-invasive measurements.

The reported sensitivity and excitation power have already proved to be sufficient for measurements on a test device, where we demonstrated the coherent interaction of a fractal resonator with a Cooper pair box in NSMM configuration [82]. Such an experiment claims the strong potential of our microscope for the coherent interaction with a single TLS in a quantum regime. This technique opens up new prospects for studying losses in the dielectric comprising TLSs and for implementing localized spectroscopic characterization of an individual TLF at single photon power levels [77].

In the future developments of the microscope, for having single photon pow-

3. Near Field Scanning Microwave Microscopy

ers in the probe, the microscope sensitivity and stability must be improved. One should focus on increasing the resonator Q-factor, reducing the mechanical vibrations in the system, introducing better shielding from high temperature radiation by integrating the microscope inside a 0.3 K shield, as well as implementing a cryogenic amplifier with a quantum-limited noise performance.

Chapter 4

Electron Spin Resonance Spectroscopy

In this chapter we will explain how microwave reflectometry is deployed in ESR spectroscopy and will motivate the advantage of deploying a thin film TL superconducting resonator in this characterization technique in section 4.1. Different requirements set new challenges for obtaining useful spin-probe resonators to successfully interrogate with spin samples (section 4.2). We will briefly describe the modifications we made to our original fractal scanning resonator design to overcome the challenges and then will go through the fabrication steps in section 4.4.2. The important results will be discussed in section 4.5 and the chapter will be summarized in section 4.6 (Paper II).

4.1 Introduction

The growing quest for an alternative quantum computing architecture that utilizes natural TLSs rather than engineered qubits, gave hype to the spectroscopic characterization of spin ensembles containing small number of spin arrays as strong contenders for quantum memories [17, 18, 83]. Electron Spin Resonance (also known as Electron Paramagnetic Resonance (EPR)), which entered various research fields since 1940's, is a technique, that allows to study the interaction of materials containing spins with microwaves [84]. The operation principle of

4. Electron Spin Resonance Spectroscopy

standard ESR spectroscopy is based on the microwave radiation absorbed by a paramagnetic sample at certain frequencies for a given magnetic field or, alternatively, at certain magnetic fields for a given microwave frequency.

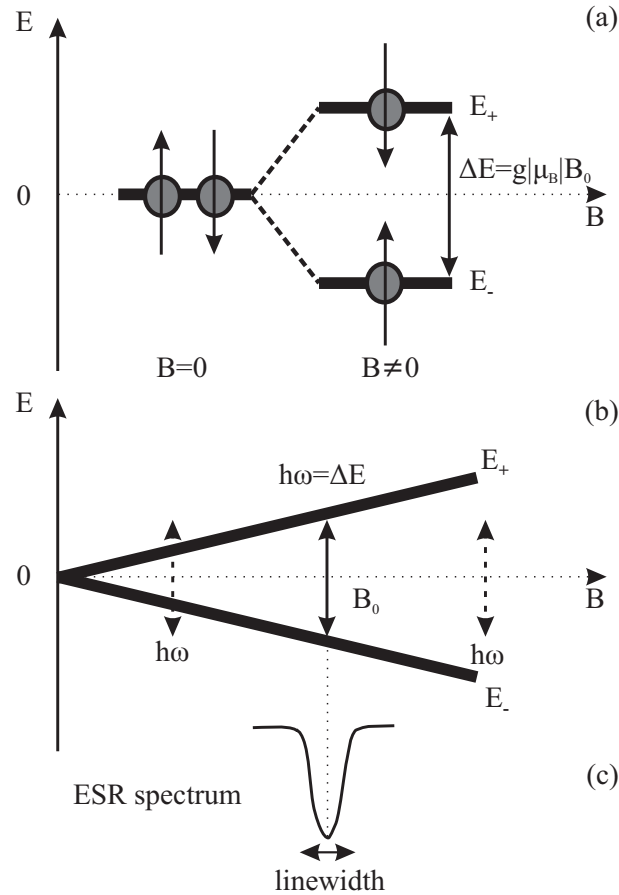


Figure 4.1: (a) The Zeeman effect. Magnetic field splits the energies of free electron spin-up and spin-down states. (b) The resonance condition is reached for a fixed microwave radiation and swept static magnetic field. (c) ESR spectrum for a free electron spin. The picture is reproduced from [84].

The ESR signal emerges from the Zeeman effect. Electrons have an intrinsic angular momentum called spin. According to quantum mechanics, the free electron spin can have two states, with opposite orientations but same magnitude. The spin vector for these two states is assigned quantum mechanical numbers: $S_z = \pm\hbar/2$. The spin angular momentum in its turn is associated with a magnetic moment: $\mu_e = g\mu_B S$, where $g = 2.002319$ is the free electron g -factor and $\mu_B = -9.2741 \cdot 10^{-24} \text{ JT}^{-1}$ is the Bohr magneton. When the electron is in the presence of a static magnetic field, the energies corresponding to different spin

4. Electron Spin Resonance Spectroscopy

states separate,

$$E_{\pm} = -\mu_e B = g|\mu_B|S_z B_0 = \pm \frac{1}{2}g|\mu_B|B_0, \quad (4.1)$$

assuming magnetic field B_0 is along z-axis. The splitting of electron spin energy in the presence of a magnetic field is called the Zeeman effect (demonstrated in Fig. 4.1 (a)). The electron in the lower state may absorb microwave radiation and get excited into a higher state, if the radiation frequency matches the energy difference between upper and lower electron spin states:

$$\hbar\omega = \Delta E = g|\mu_B|B_0. \quad (4.2)$$

In a similar way, the electron in the upper state may absorb microwave radiation and relax into the lower level, emitting microwave energy into environment. The ESR setup detects net absorption, i.e. the difference between the number of photons absorbed and the number emitted. To observe ESR resonance absorption, the spin ensemble is placed in the swept static magnetic field and a fixed frequency microwave radiation¹. When the magnetic field intensity matches the resonance condition in Eq. (4.2), ESR absorption takes place (Fig. 4.1 (b,c)).

Bulk cavity resonators are the basic building blocks of standard ESR spectroscopy. The resonator should sustain strong enough magnetic field needed to bring the spins in resonance with microwaves and should have low internal losses in order not to obscure the energy absorption by spins. The spin detection sensitivity is defined by the ratio of the energy absorbed in the spin sample to the energy absorbed in the resonator. This ratio in its turn is proportional to the filling factor η , i.e. the ratio of the sample volume to the resonator volume. The conventional bulk cavity resonators applied in ESR studies have dimensions of about λ^3 , ($\lambda = 1$ cm being the wavelength of microwave field), translating into a filling factor of about 10^{-18} for a nanoscale spin sample. To maximize this ratio, it is essential to have a compact resonator.

Despite the extensive efforts, the state of the art sensitivity of the best commercial ESR spectrometers is still limited to $\sim 10^9$ spins/ $\sqrt{\text{Hz}}$ [19]. On the other

¹The other ways are not relevant in this thesis.

4. Electron Spin Resonance Spectroscopy

hand, a tremendous advance in nanotechnology puts ever increasing demand on expanding ESR to nanoscale objects with number of spins well below 10^4 , and, ultimately to a single spin. As explained before, the low filling factor of bulk cavity resonators obviously calls for a miniaturized sensor design. With recent advances in nanofabrication, CPW resonators with typical dimensions of few μm have become an alternative for bulk cavity resonators. In coplanar design, the gap between the central line and the ground plane, where the microwave field is localized, can be made $< 10 \mu\text{m}$, so that the microwave mode volume is squeezed 10^6 times. As a result, the filling factor can be significantly boosted up.

Even with such a boost, to detect a single spin is quite a challenge. A single spin can only absorb a single photon, and if there are, say, one million photons in the resonator, then the absorption of a single photon can hardly be spotted. Practically, the number of photons in the resonator should not exceed the number of spins in the sample, and, ultimately, for a single spin detection the microwave power in the CPW resonator must be kept close to a single photon level.

Apart from introducing spin induced absorption, the spins placed in resonator also shift the resonance frequency. The frequency shift of the resonator, induced by the presence of a single spin, can be estimated as follows. From a resonance frequency $\omega_0 = 1/\sqrt{LC} = 6 \text{ GHz}$ and impedance $Z_0 = \sqrt{L/C} = 50 \Omega$, we get CPW total capacitance of $C = 0.5 \text{ pF}$ and inductance of $L = 1.3 \text{ nH}$. Next, we can estimate the microwave current corresponding to a single photon circulating in the resonator, by equating the photon's energy to magnetic energy $\hbar\omega_0 = LI_{rms}^2/2$, the root-mean-square current will be $I_{rms} = 50 \text{ nA}$. Knowing the current, it is possible to estimate the magnetic field for a CPW central strip to be $B_0 = \mu_0 I_{rms}/l_p = 3 \cdot 10^{-7} \text{ T}$, where the cross-section perimeter of a strip with $1 \mu\text{m}$ width and 250 nm thickness is $l_p = 2.5 \mu\text{m}$. In a magnetic field B_0 , a spin will oscillate with a Rabi frequency $g_0 \approx \mu_B B_0 = 2\pi \cdot 300 \text{ Hz}$, i.e. single photon energy will go back and forth between microwaves in the resonator and the spin, with a rate g_0 . This rate is what defines the coupling between two resonance systems: the microwave cavity and the spin. For spins located further away from the strip, the coupling will be smaller. Averaging over the whole coupling area, we arrive at an average single spin coupling $g_0 = 2\pi \cdot 75 \text{ Hz}$ [8].

To detect such a small shift caused by a single spin, a resonator with a Q-factor

$Q = \omega_0/g_0 > 100000$ is necessary, calling for a superconducting CPW resonator. However, a superconductor as a resonator material presents an obvious problem: the magnetic field needed to bring electron spins into resonance with microwave field exceeds the first critical field for most superconducting materials (~ 350 mT for a resonance frequency of 10 GHz). For a standard CPW design, the vortex-induced dissipation degrades the Q-factor by many orders of magnitude. Also, due to flux focusing, vortices penetrate the superconductor at a much lower magnetic field, thus making CPW design not suitable as an ESR sensor [85]. To reach the desired Q-factors, some advanced engineering is a must.

As it was mentioned before, small spin arrays are prospective candidates for hybrid quantum memory systems. This application requires the spin array to be strongly coupled to the electromagnetic field. Unfortunately, single spin to microwave coupling does not exceed $g_0 \sim 300$ Hz even for the most prospective planar resonators [86]. To bring the spin system into a strong coupling regime, all prototype designs reported so far exploited the cooperative coupling enhancement $\Gamma = \sqrt{N} \cdot g_0$ for an N-spin ensemble in macroscopic (~ 1 cm) crystals [87–89]. The most straightforward way to miniaturize the design will be to build a memory element around a microscopic spin sample like in Ref. [90]. Assuming a resonator Q-factor of 10^6 , we can reach a strong coupling regime for $N \approx 10^3$ spins in the ensemble. All these requirements together call for a superconducting CPW resonator design, that withstands strong static magnetic fields and maintains a high Q-factor.

4.2 Challenges to be addressed in ESR

- To boost the spin-microwave coupling and therefore, spin sensitivity, the resonator must be compact, such that due to a squeezed microwave mode volume the microwave energy density is increased at the volume of the spin sample.
- To tolerate strong static magnetic fields and maintain a high-Q factor, the resonator design should suppress magnetic field induced dissipation. Possible directions that can lead to reduced dissipation are: reduced current

4. Electron Spin Resonance Spectroscopy

in the resonator, reduced flux focusing, as well as flux pinning centers (as already discussed in Chapter 2).

4.3 A slow propagation line for ESR

The slow propagation fractal line, developed for our scanning resonators (Fig. 3.2), turned out to be also a good starting point for the development of spin-sensitive resonators for ESR spectroscopy. First of all, the compactness of the resonator is promising for an increased coupling of spin systems to microwave field. Then, importantly, fractal design naturally exhibits attractive intrinsic features leading to reduced magnetic losses. Those features are: the specially engineered current branching in the primary, secondary, tertiary, etc. fractal iterations, the fractallized ground plane optimized for suppressed flux-focusing and the pinholes in the non-fractallized area, acting as flux-pinning centres. We will go through these design features in more detail in the next section.

4.4 Experimental Techniques

4.4.1 Fractal resonator design concepts

The design concept and optical images of the $\lambda/2$ resonator are demonstrated in Fig. 4.2. The design is similar to our scanning resonator design in Fig. 3.3 (in chapter 3), in a sense that it is an electromagnetic analog of a mechanical tuning fork. Same as the design in Fig. 3.3, it is also compact (1.6 mm) thanks to reduced propagation velocity. The differences are:

1. There is only one coupling loop, which magnetically couples to a feedline defined on the same chip. The resonator is inductively coupled to the CPW feedline at its current antinode (Fig. 4.2 (c)). The thin ground strip between the loop and the feedline is necessary to have a continuous path for the return currents on the feedline ground plane. Otherwise, the currents will have to encircle the whole resonator and induce radiation. Close to the current antinode, in between two superconducting strips, where the

4. Electron Spin Resonance Spectroscopy

magnetic field components of the microwave field from two strips sum up giving rise to maximum magnetic field, we put the spin sample for ESR spectroscopy (Fig. 4.2 (c,d)).

2. At the ends with voltage antinodes, resonator prongs are terminated with a large inter-digitated capacitor. Covering the capacitor with a dielectric plate enables the frequency tuning of the resonator (Fig. 4.2 (e)).

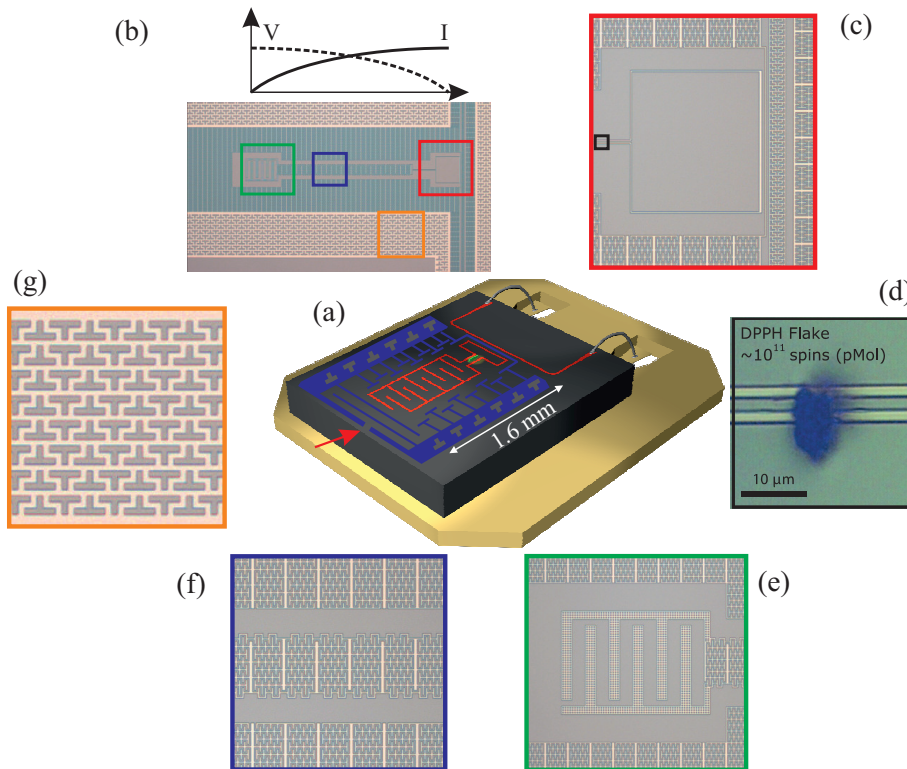


Figure 4.2: (a) A sketch of a fractal resonator chip, mounted and bonded on a PCB. The red pattern depicts the feedline and the resonator, the blue frame represents the ground plane and the spin sample is illustrated in green. The red arrow points at the escape route for flux. (b) Optical microscope image of a 5 GHz resonator, coupled to a microwave feedline. Microwave current and voltage modes for a single prong are shown on top. (c) Zoom-in on the inductive coupling loop, separated from the fractallized ground plane with a gap. (d) Zoom-in on the maximum current area that is depicted with a black frame in (c), with a flake of a DPPH spin sample. (e) Resonator prongs terminated with a large inter-digitated capacitor. (f) Zoom-in on resonator central area surrounded with ground planes on both sides. (g) Pinholes in the ground plane to induce vortex pinning.

4. Electron Spin Resonance Spectroscopy

The following modifications were made to optimize the resonator design for magnetic field studies:

1. An important property of the fractal design, that has contributed to the reduced magnetic field induced dissipation, is its short length with a branched current between many superconducting strips. As we have already mentioned in the previous chapter, the magnetic field dissipation is proportional to the current flowing in the resonator $p_0 \sim i_0^2$, where p_0 is the dissipation per unit length of a fractal line and i_0 is the current. In the resonator central area (shown in Fig. 4.2 (f)), the microwave currents pass through a network of many fractal iterations connected in parallel to minimize the total network resistance (r), as sketched in Fig. 3.2. In the fractal network, only the main branch significantly contributes to the current and thus the total dissipation is $P_{loss} \sim p_0 L_0$ (L_0 is the length of the primary fractal iteration). As compared to conventional CPW resonators with a similar strip size and resonance frequency, L_0 in the fractal design is shortened ~ 10 times (1.6 mm vs 12 mm), accounting for almost an order of magnitude less dissipation¹. Indeed, the resistive losses in the resonator are given by $1/Q = r/Z_0$, where Z_0 is the resonator impedance, and reduced resistance r translates into reduced resistive losses in the resonator.
2. The flux focusing is dramatically reduced, because the non-metalized area surrounding the fractal resonator is 150 μm wide, which is 30 times wider than the gap in a typical coplanar resonator. The flux focusing can be reduced even further by replacing a solid ground plane with fractal-like structure which allows all the excess flux to spread over the whole fractalized area. Also, to avoid currents circulating the resonator, we make sure there is a path, not enclosed with superconductors, for the flux to escape (Fig. 4.2 (a), pointed with a red arrow). Next, the fractalized ground planes, together with the resonator symmetry, help to control radiation losses in the resonator. A solid ground plane (Fig. 4.3 (a)) would screen the resonator better than the fractalized ground plane does (Fig. 4.3 (b)),

¹Assuming magnetic field penetrates superconductor on the length scale $< \lambda_L$. In case of stronger fields, penetrating the superconductor deeper than λ_L , the dissipation is 3 times lower than in CPWs.

4. Electron Spin Resonance Spectroscopy

but at the expense of increased flux focusing in the former case, therefore the fractallized ground plane is a good trade-off.

3. Fractalization splits the superconductor into $2 \mu\text{m}$ wide strips. This technique aims to reduce the width of superconducting strip $< \lambda_L$, so that it will expel vortices and become more magnetic field resilient [91].
4. Finally, to minimize flux-induced dissipation by flux pinning, the outer ground plane area of the resonator is perforated with pinholes (Fig. 4.2 (g)).

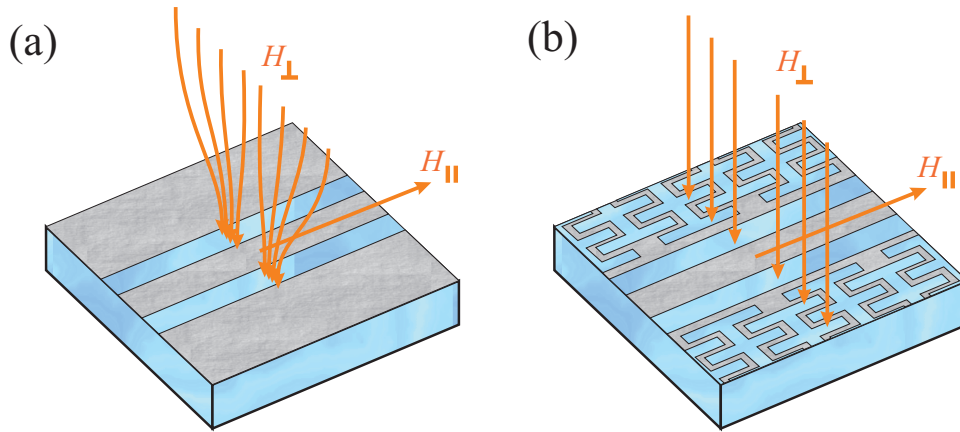


Figure 4.3: (a) A sketch of flux focusing in a CPW line. The ground plane is pictured in grey, the superconductor in light blue and the magnetic flux lines in orange. (b) Reduction of flux focusing via spread of flux lines in the fractal pattern.

4.4.2 Microfabrication of fractal resonators for ESR

Fractal resonators for ESR studies were fabricated with 200 nm Nb sputtered on a sapphire substrate. Nb was chosen because of its high H_{c1} critical field value. Samples were patterned with a single e-beam lithography step and CF_4 / O_2 RIE etching.

The spin sample for ESR spectroscopy is a small flake of 2,2-diphenyl-1-picrylhydrazyl (DPPH) crystal (see Fig. 4.2 (a), in green, (d) in black). From the sample size ($\sim 10 \times 8 \times 8 \mu\text{m}^3$) and spin density, we estimate the sample to contain approximately 10^{11} spins. DPPH is an organic molecule and it is a

4. Electron Spin Resonance Spectroscopy

well known reference sample for ESR studies, as it has a single and sharp spin resonance line in the ESR spectrum (g factor of 2), which makes it easy to detect.

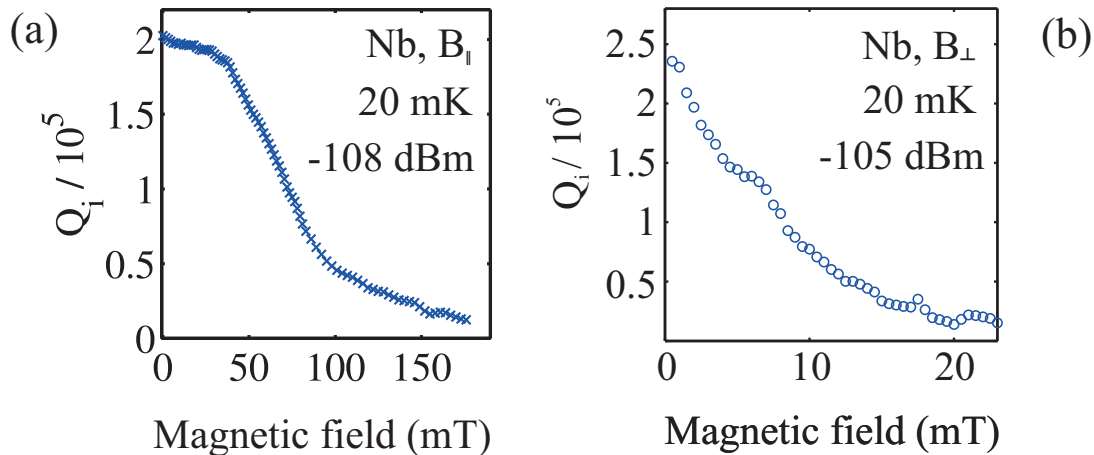


Figure 4.4: (a) Internal Q-factor for Nb/sapphire resonator as a function of parallel magnetic field, measured at 20 mK, -108 dBm power. (b) Internal Q-factor for Nb/sapphire resonator as a function of perpendicular magnetic field, measured at 20 mK, -105 dBm power.

4.5 Results

We will now present a short summary of results taken with our fractal resonators and will discuss the current status of this project together with prospective future work.

The S_{21} transmission measurements were performed in a He gas-flow cryostat with 1.8 K base temperature and a dilution refrigerator at 20 mK. With our Nb resonators we have achieved internal Q-factors of ~ 25000 in parallel to substrate magnetic fields of 160 mT (20 mK, excitation power -108 dBm, Fig. 4.4 (a)). The achievable Q-factors were ~ 10 times higher than previously reported in literature for such a strong field [85]. Such an excellent performance was mainly thanks to the special current splitting technique.

In perpendicular magnetic fields up to 25 mT, the measured internal Q-factors remained ~ 25000 (20 mK, excitation power -105 dBm, Fig. 4.4 (b)). Such a loss rate was 50 times better than reported in literature by that time [92]. This

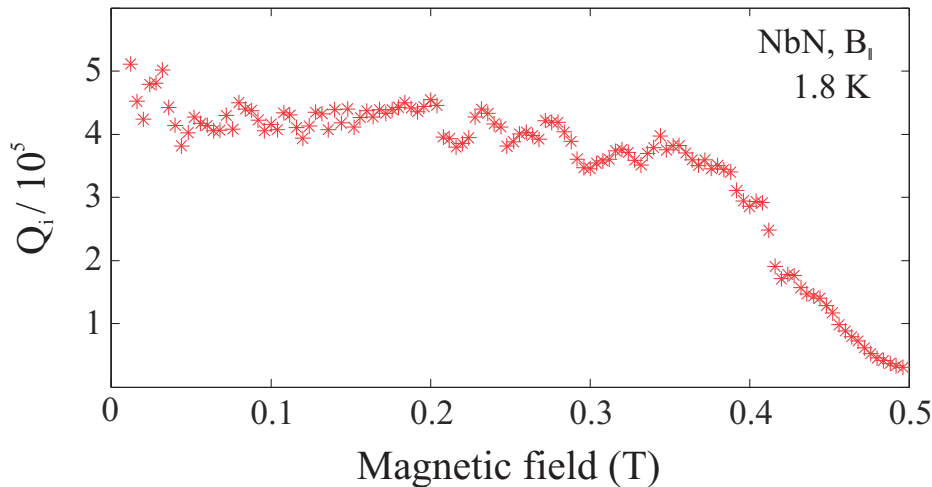


Figure 4.5: Internal Q-factor for NbN/sapphire fractal resonator as a function of parallel magnetic field, measured at 1.8 K.

improvement was due to ~ 10 times reduced flux focusing factor in the fractal design together with an order of magnitude reduced current-induced dissipation as compared to CPWs.

At the lowest powers, with the circulating power in the resonator in the range of $\sim 0.1\hbar\omega$, the 0-field internal Q-factors of fractal resonators saturated around few tens of thousands (at 20 mK). This was inferior to the best numbers reported for CPW designs. We attribute this to significant coupling to TLF's in the resonator substrate due to its large fractal perimeter.

Except Nb, we have also tested the resiliency of NbN/sapphire fractal resonators to magnetic fields, having in mind the higher second critical field H_{c2} of NbN. NbN resonators sustained much stronger parallel magnetic fields, revealing Q-factors above 100000 in fields up to 400 mT (at 1.8 K), shown in Fig. 4.5¹.

4.5.1 ESR spectroscopy on a DPPH sample

To benchmark the sensitivity of our ESR setup, we measured on a small flake of DPPH sample. A flake with dimensions of $\sim 10 \times 8 \times 8 \mu\text{m}^3$ was placed on a Nb/sapphire fractal resonator, where the magnetic field component of microwave field is at maximum. To read-out the spin state of the spin sample, we implemented the PDH technique, described earlier in section 3.5.2. This tech-

¹At 300 mK and zero field, Q-factors were in the order of 10^6 .

4. Electron Spin Resonance Spectroscopy

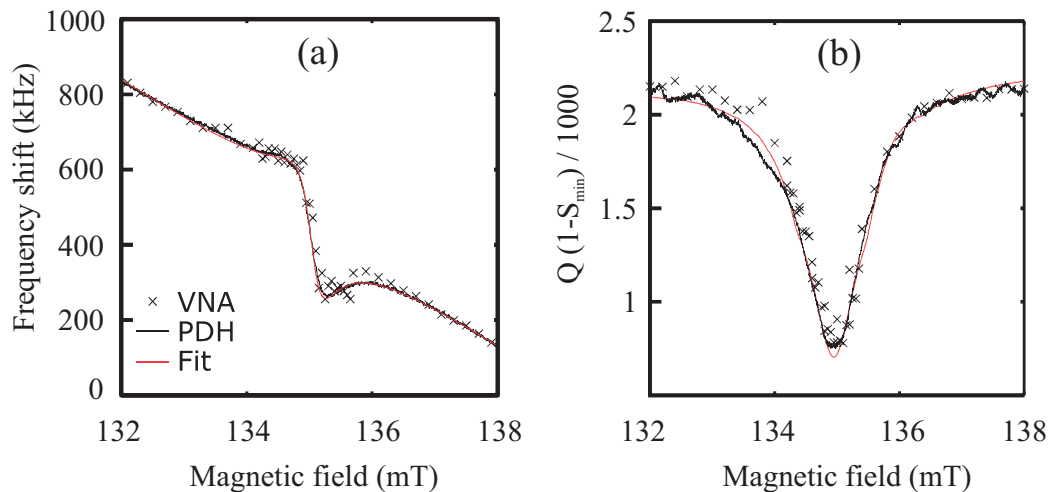


Figure 4.6: ESR signal measured near the Zeeman field for a resonator coupled to a DPPH spin ensemble. $T=1.7$ K, excitation power -80 dBm. (a) Frequency shift. (b) Resonator Q-factor. Data is fitted to a theoretical response (red). The parameters extracted from the fit are: total coupling $\Gamma/2\pi = 1.5$ MHz, spin linewidth $\gamma/2\pi = 15$ MHz. Adopted from [93].

nique allows to read-out resonator frequency shifts with a noise level of ∓ 1 kHz and $\mp 0.2\%$ variations in Q-factor. The recorded resonance frequency shift and dissipation versus magnetic field are presented in Fig. 4.6.

The ESR transition was observed at a Zeeman field of 135 mT corresponding to 3.73 GHz (1.7 K) [93]. Both data taken with VNA and PDH were consistent with the theoretical fit. As we knew how much a single spin should shift the resonance frequency (single spin coupling $g_0/2\pi = 75$ Hz) and we measured the cumulative effect of many spins (total coupling $\Gamma/2\pi = 1.5$ MHz), we could deduce the total number of spins in the sample: $N = \Gamma^2/g_0^2 \sim 10^8$ spins. This number is in agreement with the spin density and the size of the flake, considering that at 1.7 K only 15% of spins are polarized, the spin participation ratio is 25% and there is another factor of 25% due to the sample volume with spins actually coupled to microwaves. Taking into account $\text{SNR} = 300$ for PDH technique, estimated from a fit to the theoretical response in Fig. 4.6, a spin linewidth of 15 MHz and a PDH time constant of 150 ms, the minimum detectable number of participating spins can be estimated as $\sim 5 \cdot 10^5$ spins/ $\sqrt{\text{Hz}}$. The minimum detectable number of spins, reported by our group, was about four orders of magnitude better than in commercial spectrometers [19] and comparable to state of

the art ESR measurements [20].

4.6 Summary & Outlook

It is instructive to compare the sensitivity of our planar resonator based set up against the sensitivity achieved with a bulk cavity. Fig. 4.7 presents our latest (as yet unpublished) data and demonstrates the current status of spin sensitivity limit that we have achieved so far with our NbN resonators at 300 mK. The resonator (4.4 GHz) has no intentionally introduced spins and we have measured resonators on a pristine sapphire. The small peak at $g \approx 6$, shown in Fig. 4.7 (a), is related to naturally occurring paramagnetic impurities in sapphire and was observed by other groups as well [94]. The peak, corresponding to 10000 spins¹, is very reproducible and is approximately 10 times above the noise level (1000 spins), (Fig. 4.7 (b)). This number is seven orders of magnitude below the number of spins detected in Ref. [95] for spins in a 2-DEG quantum dot. In Ref. [95], the experimental setup was based on a conventional bulk cavity spectrometer and a cryogenic High Electron Mobility Transistor (HEMT) amplifier at 5 K. Via magnetic field modulation, they have measured a spin signal proportional to the derivative of the Q-factor, while our spin signal is directly proportional to the resonator Q-factor (Fig. 4.7 (c)) [95].

As explained earlier, no spins were intentionally introduced into resonators and the presented ESR data are for pristine sapphire. Still, we see a clear spin signal in the ESR spectrum at $g \approx 2$ due to some environmental spins (around 10^6 spins or 10^{-3} of the monolayer). It was demonstrated that these environmental spins cause decoherence in flux qubits and noise in superconducting quantum interference devices (SQUIDs) [96]. Though these spins are known to be spurious TLFs of obscure origin, their presence on the sapphire surface was certainly reported. To shed light on the nature of these spins, we are currently undertaking a full-scale study applying our ESR technique with high sensitivity, combined with surface treatments of sapphire. We believe that this is the first ever direct observation of sapphire surface TLFs. Though this observation gives a great insight

¹Estimated from the area under the peak.

4. Electron Spin Resonance Spectroscopy

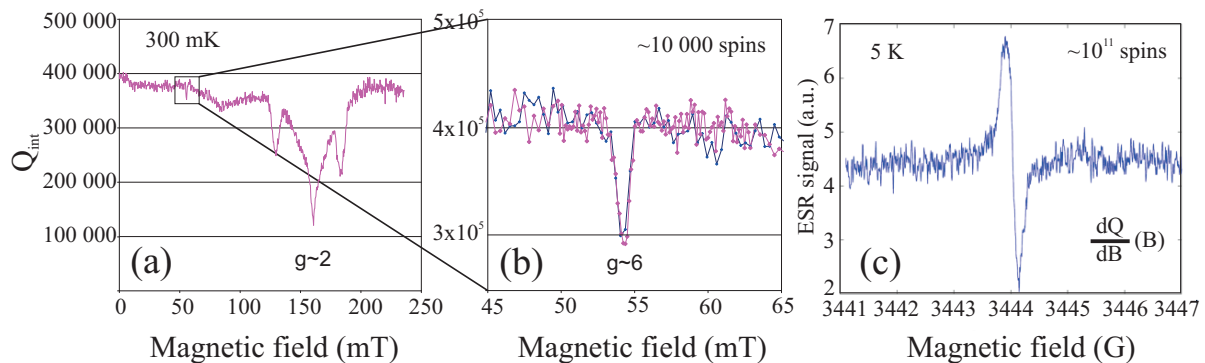


Figure 4.7: (a) Internal Q-factor measured for a pristine NbN/sapphire fractal resonator with 4.4 GHz resonance frequency. $T=300$ mK, excitation power -80 dBm. (b) Zoom-in on $g \approx 6$ peak in (a). Estimated number of spins is 10000, with a noise floor of 1000 spins. Different colors correspond to trace/retrace scans to show signal reproducibility. (c) The result reported in [95], for a sample with $\approx 10^{11}$ spins. ESR signal dQ/dB as a function of magnetic field for a bulk cavity resonator measured at $T=5$ K.

on the behavior of surface TLFs, still a lot of research is needed to control or even remove these TLFs for fighting decoherence and noise in quantum devices.

In summary, our Nb resonators can sense $5 \cdot 10^5$ spins of DPPH molecule with aW probing power at 20 mK temperatures. Thinner Nb films are expected to help in boosting the magnetic field resiliency of resonators [97]. Improved resiliency can be achieved also by further reduction of flux focusing with an extra fractal iteration, if microfabrication limits are beaten. Recently, an exceptional resiliency to 6 T magnetic field was reported for a superconducting narrow strip, not surrounded by a ground plane [98]. As the vortex state becomes energetically unfavorable in this narrow strip, it expels the magnetic field more efficiently. We foresee that we can reach similar performance with a proper modification of our microstrip resonator (see section 5.7).

With NbN resonators at 300 mK temperatures, we have demonstrated the ESR spectrum taken on a sample of 10000 environmental spins. The data presented in Fig. 4.7, taken with VNA, demonstrate the noise floor of 1000 spins.

The possibility to study very small number of spins makes these resonators prospective candidates for reaching the ultimate limit of ESR sensitivity: the single spin detection. Still, until a coherent interrogation with a single spin can become a reality, there is a lot to understand and study in this interesting field.

4. Electron Spin Resonance Spectroscopy

Currently, the future progress of our spin detection sensitivity is hampered by the presence of the environmental spins. Otherwise, we are certain that taking the following actions can, in principle, reduce the spin sensitivity down to single spin detection: as explained earlier, applying PDH readout technique in the experiments shown in Fig. 4.7, we can further reduce the noise floor by a factor of ~ 10 . The noise temperature of our low temperature HEMT amplifier is $T_N \sim 5$ K. Deploying a quantum-limited parametric amplifier will boost the spin sensitivity down to 10 – 100 spins. Moreover, having a few hundred nm wide constriction in the CPW area dedicated to coupling to spins, will locally boost the magnetic field and reduce the spin sensitivity down to 1 – 10 spins. This shall make the next crucial step towards the Holy Grail of ESR spectroscopy: the single spin detection, opening up for a set of c-QED experiments.

4. Electron Spin Resonance Spectroscopy

Chapter 5

Kinetic Inductance Traveling Wave Parametric Amplifier

In the first part of this chapter, we will discuss the challenges reported in literature with earlier attempts to implement a practical traveling wave parametric amplifier and we will propose the slow propagation fractal line as a solution to address the challenges. We will go through a list of design considerations and fabrication techniques that will motivate the choice of the established processes for building slow propagation line-based TWPA and serve for the new starter fellow as a background work to move on. The story-line of alternative techniques for producing fractal transmission lines for TWPA is presented in section 5.4.1. The measurement techniques, presented in section 5.4.2, include details on room temperature and cryogenic (2 K) setups for gain and dc bias measurements. The important results will be discussed in section 5.5 (Paper III, IV).

In the second part of this chapter, we will propose microstrip lines with a deposited thin film dielectric as a competitive replacement for CPWs (section 5.7). Section 5.10.2 will describe the fabrication of microstrip resonators and section 5.10.3 will present the cryogenic (300 mK) setup for dc bias and microwave measurements. The important results will be discussed in section 5.11 (Paper V). Each part of this chapter will conclude with a summary and outlook.

5.1 The call for a low-noise, practical amplifier

As we have learnt by now, a further boost in the ESR spin sensitivity, as well as a coherent interaction with an individual TLS (TLF) in the nc-AFM-NSMM technique call for an ultra-low noise amplifier.

Amplifiers are ubiquitous: the desire for a better amplifier hardly needs any justification. The main purpose of any amplifier, as the name suggests, is to amplify a small signal. In practice, how small signal an amplifier can deal with depends on its noise properties: as soon as the signal is below the noise added by the amplifier, the amplification no longer improves the quality of the signal. The minimum added noise is set by the laws of thermodynamics (thermal fluctuations) and quantum mechanics (vacuum fluctuations). While the former can be, at least in principle, suppressed at low enough temperatures, the latter is fundamental and can not be eliminated. That is, no amplifier can be ideal (noise free), a perfect amplifier is the one ultimately limited by quantum fluctuations.

State of the art semiconductor amplifiers are limited by thermal fluctuations, even when operating at cryogenic temperatures: for the best units the thermal noise power is ~ 16 dB (a factor of ~ 40) above the quantum noise limit of $\hbar\omega/2$ [57, 99]. A quantum-limited amplification was achieved in the optical domain for fiber optical parametric amplifiers [58] and the great potential of this technology for next-generation telecommunication systems have been demonstrated [100].

The race is now on to reach an ultimate performance in the microwave domain. This, however, represents a substantial challenge: while in optics the energy ~ 1 eV = 10^4 K of a single quantum exceeds an environmental temperature by orders of magnitude, thus naturally making thermal fluctuations negligible, in the microwave domain the situation is opposite: 1 GHz translates into $\hbar\omega/2k_B = 50$ mK equivalent temperature. As the thermal noise stems from any dissipative element, the only way to reach the quantum-limited performance in the microwave domain is to eliminate all resistive elements from the amplifier design, i.e. to build an amplifier from superconducting elements only.

Parametric amplifiers can reach quantum-limited noise performance in the microwave domain. The first quantum-limited superconducting parametric amplifiers were implementing the nonlinearity of the Josephson inductance [101].

5. Kinetic Inductance Traveling Wave Parametric Amplifier

However the dynamic range of Josephson paramps (JPA's) is limited by the Josephson energy (the input saturation power being below -100 dBm) [102]. Also, being resonance devices, these amplifiers have a limited bandwidth less than 1 GHz [22, 103, 104]. To get a similar gain in a non-resonance device, it was suggested to 'unfold' the resonance cavity into a line loaded with periodic array of Josephson elements. In such a Josephson traveling wave parametric amplifier (JTWPA) instead of passing many times through the same element, the signal will be amplified after passing through many cascaded junctions [21, 102, 105]. Unfortunately, an implementation of this idea faces many technical difficulties and has not yet resulted in a practical amplifier. Finally, Josephson elements based on aluminum junctions are limited to operating temperatures < 1 K.

A proof-of-concept close to quantum-limited superconducting TWPA was reported in the pioneering paper by Eom et al., where the nonlinearity intrinsic to the superconductor kinetic inductance was used rather than Josephson inductance [24]. For distinction, from now on, we will call it a kinetic inductance traveling wave parametric amplifier (KI-TWPA instead of TWPA). The operation of KI-TWPA is based on co-propagating waves in a transmission line that deliver parametric gain due to the process of FWM (see section 2.3). Such amplifiers are favorable for few reasons: they enable operating temperatures up to 4 K, higher dynamic range, bandwidths up to a few GHz and more controllable nonlinearity as compared to Josephson element-based amplifiers. However, as it is always the case in life, there must be some kind of compromise and below we will go through the chain of problems limiting the progress of KI-TWPA's reported in literature.

Because the nonlinearity intrinsic to the superconductor is rather weak, to get a substantial nonlinearity, one should resort to a long, thin and narrow line (see Eq. (2.45)). As a result, in Ref. [24] a coplanar line $1 \mu\text{m}$ wide, ~ 35 nm thick and about 1 m long was needed to achieve the desired nonlinearity for ~ 10 dB gain.

From the fabrication point-of-view, even with the best microfabrication facilities it is hardly possible to produce a high aspect ratio line ($1 \mu\text{m} : 1$ m) completely free of defects (weak spots). Indeed, compelling evidence was presented in [25] that in a real device the maximum pump power (and, therefore, a nonlinearity) is always limited by local fabrication defects (weak spots); a device

5. Kinetic Inductance Traveling Wave Parametric Amplifier

with two times longer line did not deliver a higher gain.

Next, such a long line with high kinetic inductance possesses a characteristic impedance much higher than the standard instrument impedance ($300\ \Omega$ vs $50\ \Omega$ in [24]). Such a strong impedance mismatch causes strong reflections at the terminal points of the amplifier line. Most annoyingly, this serious interface problem resulted in a frequency dependent gain with bouncing ripples of more than 10 dB; the device was hardly usable as a practical amplifier. This interface problem was acknowledged in [24], but not solved.

Yet there is another troublesome consequence of the impedance mismatch: the reflections at line edges lead to the formation of standing waves, in analogue to Fabry-Perót cavity (see section 2.1.4). While not contributing to the gain (because only synchronized traveling waves matter for the gain), the standing waves cause the premature break down of superconductivity. With reduced nonlinearity, the maximum achievable gain will drop significantly.

At a glance, a solution for impedance matching could be rather straightforward with an adiabatic impedance converter. In reality, the taper converters work fine in case of moderate impedance mismatch ($70\ \Omega$ vs $50\ \Omega$). In case of strong mismatch, the predictive power of design simulation is rather questionable. To make the things worse, none of the available microwave simulation tools can adequately treat the kinetic inductance. One should rely on the combination of modeling and scaling. As a result the attempts to fix this impedance mismatch issue by deploying adiabatic tapers as impedance transformers were not completely successful [25, 106].

Finally, to be put on a chip, the very long superconducting line is folded as a spiral or a meander. This complex shape imposes a non-trivial shape also on the ground plane. The spectrum of spurious resonances overlaps with Fabry-Perót type ripples in the transmission spectrum.

In the quest for a quantum-limited amplifier, these are serious issues making the device not suitable for practical applications. Though the seminal paper by Eom et al. inspired many research teams, in more than four years since the prototype was demonstrated, no operational amplifier has been demonstrated yet.

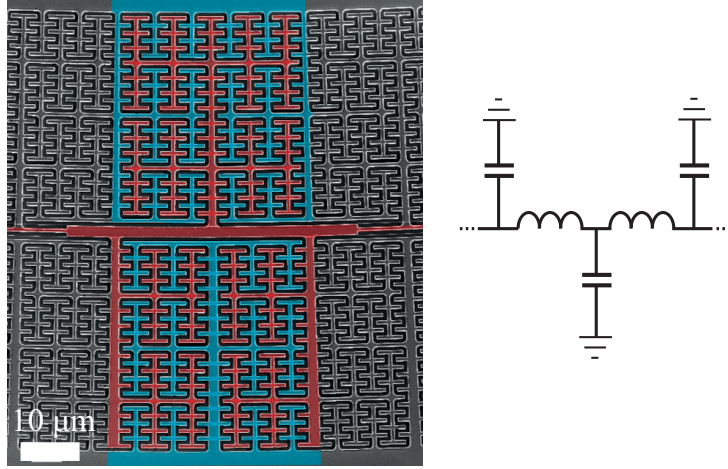


Figure 5.1: Left: a section of a fractal design used in TWPA slow propagation line, the area coupled to the central strip is in red, the ground plane is in blue. Right: the schematic representation of the design on the left.

5.2 Challenges to be addressed in KI-TWPA

- Fabrication of an almost defect (weak spot) free and a high aspect ratio superconducting TL.
- Impedance matched high-KI TL with suppressed ripples in the transmission spectrum.
- Decoupling of an amplifier structure from parasitic ground plane resonances.
- Phase matching between high power Pump and low power Signal tones.

5.3 Slow propagation lines for KI-TWPA

To address the challenges listed above, we have developed another kind of slow propagation transmission line. In this case, we slow down the wave propagation velocity via a fractal design with maximized quasi-fractal interdigitated capacitance in between the central conductor of the TL and the ground plane (Fig. 5.1). The following quick expectations can be drawn for such a design.

- Most importantly, the slow wave propagation velocity will enable to significantly shorten the TL length. Reduced TL length should result in a less defect-prone KI-TWPA line, from a fabrication point-of-view.

5. Kinetic Inductance Traveling Wave Parametric Amplifier

- A shorter line with a simpler shape will be less coupled to ground plane resonances.
- Apart from shortening the line length, the increased fractal capacitance has a second purpose. Due to its high KI, the line has rather high impedance as compared to standard $50\ \Omega$ circuitry. The increased capacitance will aid us in balancing the high-KI of the TL. This will lead to a reduced line impedance $Z \sim \sqrt{L/C}$, comparable to input/output terminal standard $50\ \Omega$ impedance, which will eventually suppress the impedance mismatch caused reflections in the structure.
- As previously explained in section 2.3.5, to achieve phase matching between high power Pump and low power Signal tones, some dispersion engineering is needed. We could arrange a dispersion engineering by periodically widening the central line, as shown in Fig. 5.1.

It took us a few iterations until we have resolved to the design shown in Fig. 5.1. To highlight for the reader the learning path we went through, three core design versions will be reviewed (Design 1, Design 2, Design 3)¹ in the following sections.

Moreover, because the fractal geometry is vulnerable to shorts (more about shorts in the next section), three different fabrication technologies have been established, aiming for a short-free device. In what follows, we will refer to those processes as: 'plasma etching', 'lift-off' and 'Chemical Mechanical Polishing (CMP)'. Although our final results were obtained with a plasma etching process, the other two processes can be considered as spin-off directions for future fractal line developments. We will describe the essence of these processes developed for our last and the best design (Design 3 below).

¹Created with AutoCAD modeling software.

5.4 Experimental Techniques

5.4.1 Microfabrication of Fractal Lines

The plasma etching process

Design 1 This design served us in making sure that the quality of our NbN material is high enough and on par with the original work reported in Ref. [24].

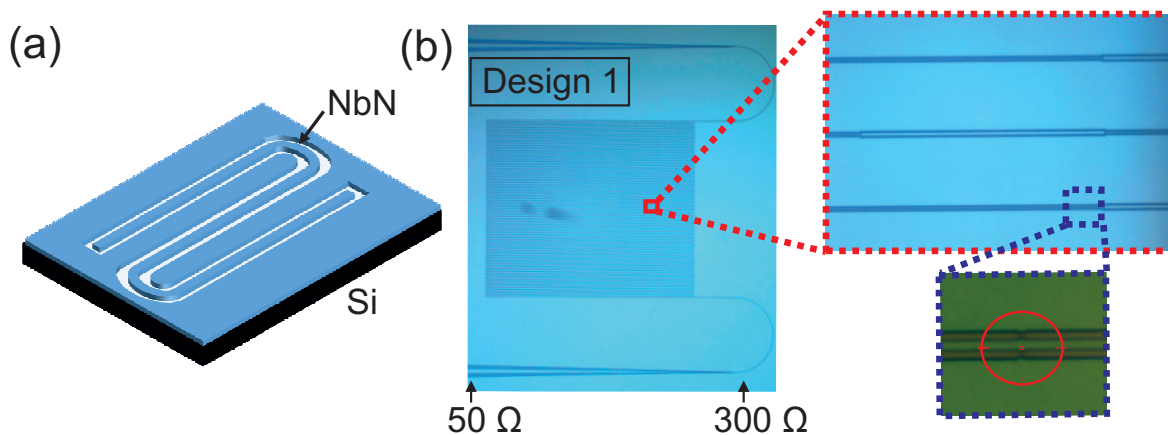


Figure 5.2: Design 1. (a) A section of a meander-shaped NbN CPW line on a Si substrate. (b) OM image of the meander line with tapered transition from 50 to 300 Ω . Inset: zoom-in on dispersion loading elements (red frame). Inset: zoom-in on a central line with a defect (blue frame).

The adiabatic tapers, shown in Fig. 5.2 (b), intended to continuously transform the high ($\sim 300 \Omega$) impedance of the high-KI line to 50 Ω , similar to the original work.

In the pioneering paper [24], as well as in follow-up designs [25, 106], to arrange dispersion the line was loaded with periodic perturbations of the central strip width. We have followed their approach as shown in Fig. 5.2 (b), inset highlighted with a red frame.¹

Similar to the original work, we also have faced the issue of weak spots due to fabrication defects. Because of the high aspect ratio of the line, it was not feasible to avoid weak spots in the line, presumably caused by stitching errors in

¹Dispersion engineering details will be given for the final Design 3, here details are not relevant.

5. Kinetic Inductance Traveling Wave Parametric Amplifier

the e-beam (Inset in Fig. 5.2 (b), highlighted with a blue frame).¹ Such weak spots constrain the width of the central strip and are tricky to detect.

For fabrication, first 140 nm NbN was sputtered on top of a 2'' Si wafer (Fig. 5.2 (a)). After defining the meander shape of a 0.5 m long and 1 μm wide line with e-beam, the line was etched with NF_3 gas in RIE plasma etching system and the chips were diced away. The sample was measured in a He^4 gas-flow cryostat at 2.3 K and the results are presented in section 5.5. In summary, the amplifier performance obtained with Design 1 was similar to that reported in [24].

Design 2 Having all the confidence that we got a grip on the basic material and design matters, we have turned to our core idea and Design 2, presented in Fig. 5.3, was developed. After the test of a few prototype devices, we resolved to this specific fractal design with the line KI optimally balanced by a fractal capacitance, thus minimizing the ripples in the transmission spectrum (see section 5.5).

The line was made of 145 mm long, 1 μm wide and 140 nm thick NbN. It is worth mentioning that to fabricate Design 2, we had to push the process to the limits of the (rather advanced) microfabrication facilities available at MC2, Chalmers. The gap in the fractal design is just 1 μm , while the perimeter is > 6 m. Despite the fact that MC2 Clean Room has Class 100-300 (ISO 5), during different fabrication steps dust particles² ended up on the sample. These dust particles masked the metal area by not letting it to get etched. Therefore 2 out of 2 chips on one 2'' wafer turned out to be shorted after single e-beam/etch cycle.

A method that solved this problem, was the following: after sputtering the NbN on top of a 2'' sapphire wafer, the fractal design was patterned twice with e-beam lithography, both exposures with two different field lines (using alignment marks) and then after each exposure was etched in RIE plasma with NF_3 gas. This was to make sure that the un-etched metal, masked by a dust particle, got definitely etched during the second e-beam/etch cycle. Before the resist removal,

¹In e-beam a large pattern is divided into smaller patterns with field lines. Stitching errors arise due to not precise stage movement from one field to the other, thus leaving an unexposed section in-between the field lines.

²Flakes from sputter target, resist dust particles, etch residues, etc.

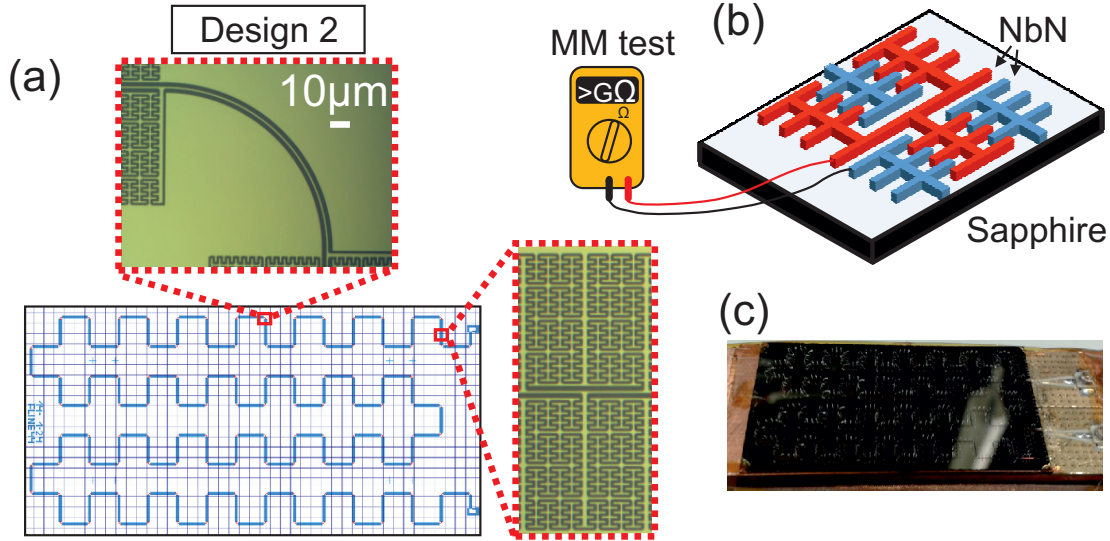


Figure 5.3: Design 2. (a) The chip design of a meander-shaped line. Top inset: each 90° turn is a CPW arc segment. Right inset: each straight segment consists of 90 fractal units shown in right. (b) A sketch of a segment of a fractal NbN central line (in red) and a NbN ground plane (in blue) on a sapphire substrate. The multimeter test indicates that the line is not shorted. (c) Photograph of the device, mounted on a copper sample stage. Numerous wire-bonds aimed to reduce ground plane resonances.

the chips were tested for shorts with a multimeter at room temperature¹. This double exposure/etch approach worked quite satisfactorily, resulting in a yield of 3 unshorted chips out of total 4.

As what concerns the dispersion engineering, practically, varying the CPW central line width modulates the local impedance by no more than 30%. In Refs. [24, 25, 106], 30% was found to be insufficient to compensate for nonlinearity: a substantial gain was only achieved with a Pump tuned close to the second band gap. A fractal design, in principle, allows for much stronger perturbation: an arc segment without fractal capacitors (see Fig. 5.3 (a), top inset) has per unit length C reduced ~ 10 times ($\sim 300\%$ perturbation of the characteristic impedance). Unfortunately, we have realized that any continuity break in a fractal pattern, such as sharp 90° turns, strongly coupled to spurious resonances (see section 5.5 for measurement details), which didn't abate even after heavily bonding across

¹For this very reason we used sapphire substrates, as Si doesn't allow a short detection due to its room temperature conductivity. This choice was compromised by the trickiness of sapphire dicing.

5. Kinetic Inductance Traveling Wave Parametric Amplifier

the line (Fig. 5.3 (c)). Therefore, for the next designs we decided to revert back to dispersion engineering by modulating the strip width.

This sample also was measured in a He⁴ gas-flow cryostat at 2.3 K and the results are presented in section 5.5.

Design 3 With Design 2 we have obtained a line, which had an impedance essentially matching to 50 Ω . The next challenge was to get rid of spurious ground plane resonances that mess up the transmission spectrum. Being a common problem in microwave designs, spurious resonances appear to be especially noxious for standard CPW-based TWPA designs, where the central line is many wavelengths long and the meander- (or spiral-) fragmented ground plane harbors a high density resonance spectrum.

Decreasing the TL length and making the shape as simple as possible, without abrupt turns, would help in somewhat reducing the coupling to ground plane resonances. To achieve this, we had to slow down the propagation velocity by an extra factor of 3 and shrink the line length down to ~ 10 cm (Fig. 5.4 (a)). Therefore, we increased the fractal capacitor area. But at the same time, to maximize the line KI nonlinearity in order to balance the increased capacitance, we had to make the film thinner. However, adversely, the high per square inductance of the ground plane film downscaled the ground plane resonance spectrum, increasing its spectral density thus giving more spurious resonances within the operational bandwidth.

To substantially mitigate this problem, we have established a novel fabrication process, where the KI was deployed only where it was actually needed, i.e. for the KI-TWPA central strip, while all other design elements (fractal capacitors, tapers and the ground plane) were implemented in a low-inductive film.

To illustrate the effect of these measures, we will compare two design versions: Design 3a in Fig. 5.4 (b) and Design 3b in Fig. 5.4 (c). Design 3a was made in a single 140 nm thick layer of NbN on a 2'' Si wafer. Similar to Design 2, it was exposed with e-beam and etched with NF₃ gas twice.

Alternatively, Design 3b was first defined in a 80 – 20 – 100 – 10 nm thick, low inductive NbN-Al-Nb-NbN multilayer sandwich on a 2'' Si wafer. After the first e-beam, top Nb/NbN and bottom NbN were etched with NF₃ gas, while

5. Kinetic Inductance Traveling Wave Parametric Amplifier

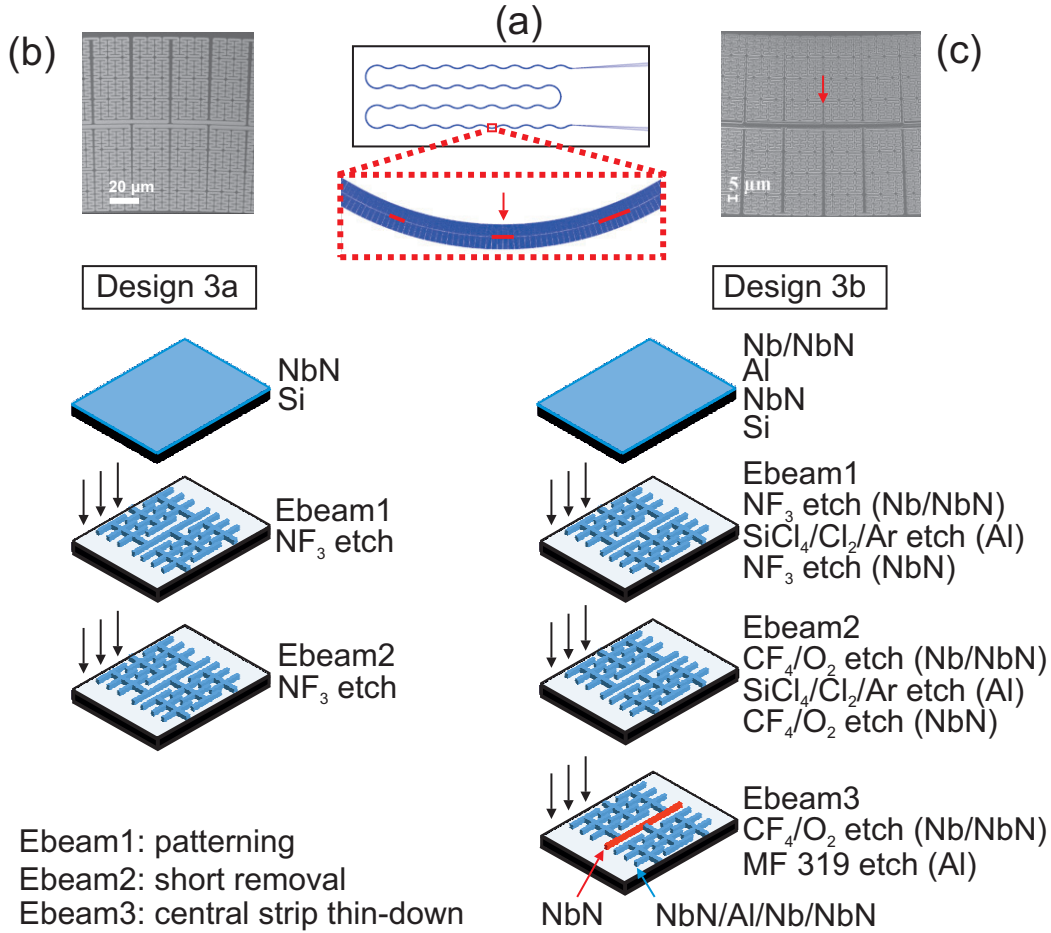


Figure 5.4: Design 3. (a) Sketch of the KI-TWPA amplifier chip with dimensions of 13 by 40 mm². Inset: zoom-in on an arc segment, the red lines show the positions of dispersion engineering elements. (b) SEM image of a basic unit fractal in Design 3a. The fabrication sequence comprising two e-beam/etch steps for a single NbN layer. (c) SEM image of a basic unit fractal in Design 3b. The multilayer fabrication sequence comprising three e-beam/etch steps.

intermediate Al¹ was etched with SiCl₄/Cl₂/Ar mixture. To get rid of shorts in the fractal structure, the e-beam/etch cycle was also done twice. During the second round, bottom NbN and top Nb/NbN were etched with CF₄/O₂ mixture instead of NF₃. In the end, the need-to-be highly inductive central strip only was exposed and thinned down to a base NbN layer with CF₄/O₂ gas mixture. The remaining Al layer on the central line was removed in a wet etch solution MF319. As a result, we have combined design elements with and without KI in the same device. See Appendix B for more fabrication details.

¹Thin Al layer served as an etch-stop in the Al/NbN interface.

5. Kinetic Inductance Traveling Wave Parametric Amplifier

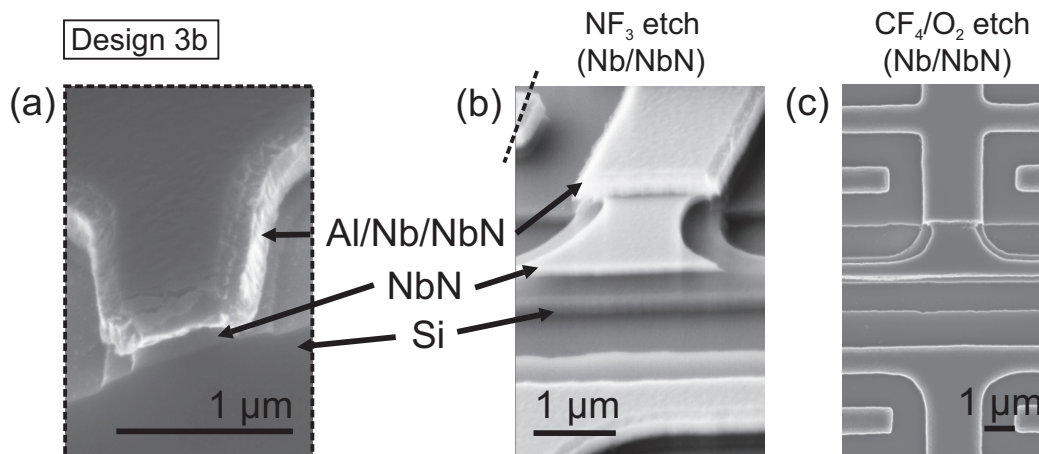


Figure 5.5: SEM images of Design 3b. (a) Cross-section of the cleaved line along the black dashed line in (b). (b) A section of fractal CPW line, etched with NF_3 . (c) A section of fractal CPW line, etched with CF_4/O_2 gases.

The reason why we couldn't use NF_3 gas in all three e-beam/etch cycles was the isotropy of etching process (see Fig. 5.5 (a)). After the first e-beam step, the NF_3 gas isotropically etched bottom NbN of the central line from both sides. If, in the next round NF_3 was used again for etching top Nb/NbN, then the bottom NbN in the central line would be completely etched from sides and after thinning down the central line to a single NbN film, the result would look like in Fig. 5.5 (b). Switching to anisotropic CF_4/O_2 was crucial for the line edge quality and the final device performance (Fig. 5.5 (c)). Because the etching was more controllable and the line was much more uniform in case of Si, we didn't use sapphire for this design, which was compromised by the inconvenience of short detection only possible after cooling down the sample.

Finally, we turn to the issue of shorts in Design 3b. With a thick multilayer and an increased fractal perimeter ($\sim 6.4 \text{ m}$), it turned out to be much more difficult to get rid of shorts even with double e-beam exposure/etching. All possible precautions taken like sputtering after a cleaned source, filtering the resist and precleaning the pipette, etc., the structures were still shorted. Eliminating these shorts was rather tedious and time consuming job. First of all, because a multimeter test could not be done on Si at room temperature, the whole fractal line had to be carefully inspected under OM (Fig. 5.6 (a-c), top). Then the detected suspicious spots were located under SEM (Fig. 5.6 (a-c), bottom), and

5. Kinetic Inductance Traveling Wave Parametric Amplifier

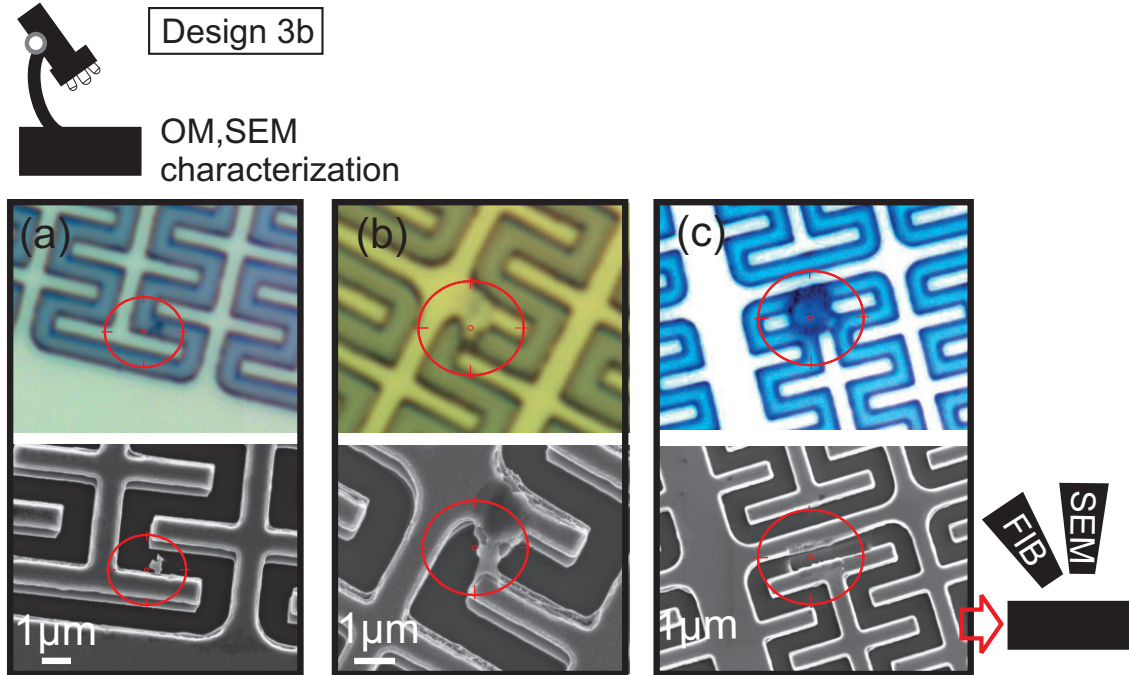


Figure 5.6: (a) OM (top), SEM (bottom) images of a defect almost shorting the fractal design. (b) OM (top), SEM (bottom) images of a short in a fractal design. (c) OM (top), SEM (bottom) images of a short that was removed with an ion milling.

finally focused ion milled in a combined FIB-SEM system (Fig. 5.6 (c), bottom). In the end, 2-3 shorts per chip were subject to ion milling.

For clarity we shall mention, that there is a big difference between two types of the above mentioned fabrication defects: the weak spots and the shorts. Any defect, partially reducing the central line width, results in a weak spot. In contrast, shorts should completely block the gap around the central line, which is less likely. On the other hand, weak spots are crucial only on the central line, shorts are disastrous anywhere in the fractal design. While the chance of having weak spots reduces with a shorter line, the chance of having shorts increases due to the increased fractal perimeter. Finally, while weak spots are difficult to detect and not possible to fix, shorts are detectable and fixable. All these pros and contras taken into account, practically, its favorable to trade the reduced chance of having a weak spot in the shorter central line with an increased chance of having a line-to-ground short.

As explained earlier, an attempt to introduce dispersion engineering by inter-

5. Kinetic Inductance Traveling Wave Parametric Amplifier

leaving fractal and non-fractal sections resulted in an increased coupling of the line to spurious resonances. So for Design 3b, we have decided to revert back to dispersion engineering by line width modulation, in order to minimize coupling to spurious resonances (see Fig. 5.4 (a), inset). The red lines mark the positions of dispersion engineering elements: the shortest $\sim 78 \mu\text{m}$, intermediate $\sim 104 \mu\text{m}$ and the longest $\sim 208 \mu\text{m}$ long (all $\sim 1.5 \mu\text{m}$ wide), defining the width of stop bands. The whole line consists of repeated unit arc sections with a length of $l_1 = 1560 \mu\text{m}$.

The Lift-Off process

In contrast to the etching process, lift-off aimed to avoid shorts by 'inverting' the process. While in the etching process the etched gaps between metal structures in the fractal design were blocked by shorts, in lift-off, the gaps would be filled with a mask $\text{Si}_3\text{N}_4/\text{Al}$, which would protect them from getting shorted by dust particles coming from sputtering (see Fig. 5.7 (a,b)).

The lift-off mask was prepared in the following way: 320 nm Si_3N_4 was deposited on 2" Si and sapphire wafers, followed by the evaporation of 120 nm Al. After defining the fractal pattern with e-beam lithography, Al was etched with $\text{SiCl}_4/\text{Cl}_2/\text{Ar}$ mixture. Next, after stripping away the resist with O_2 , Si_3N_4 was etched first with CF_4/O_2 and the last few nanometers with isotropic NF_3 gas, to induce an undercut in Si_3N_4 . Further on, the wafer was dipped in a 2% HydroFluoric acid (HF) bath, followed by the sputtering of 80/20/100/10 nm of NbN/Au/Nb/NbN multilayer. Finally, the wafer was dipped in a Buffered Oxide Etch (BOE) to lift-off $\text{Si}_3\text{N}_4/\text{Al}$ and release the gaps in the fractal design, where shorts used to happen in the etching process (Fig. 5.7 (c,d)).

We found that the result of the lift-off process also suffered from dust particles, this time coming most probably from the BOE bath. While the initial goal of protecting the gaps had worked, the actual fractal area became fragile. The resulting pattern had many areas with no metal at all, creating broken links in the superconducting line. The reason was presumably the following: a dust particle, masking a certain area, was covered by the sputtered multilayer. During lift-off the particle got removed, together with the multilayer on top, thus leaving

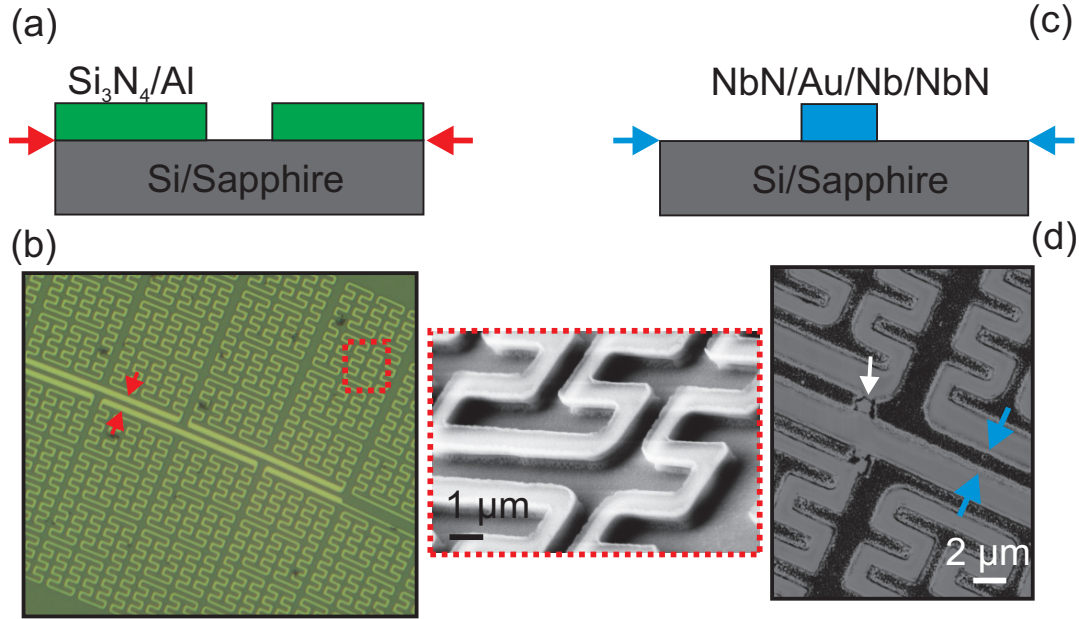


Figure 5.7: (a) The sketch of the cross-section of $\text{Si}_3\text{N}_4/\text{Al}$ lift-off mask with an opening for the central strip in (b). (b) OM image of the lift-off mask. Inset: zoom into the area highlighted in (b) with a red frame, showing the SEM image of the undercut in Si_3N_4 . (c) The sketch of the cross-section across the central strip in (d) after sputtering and lift-off. (d) The fractal pattern after multilayer sputtering and $\text{Si}_3\text{N}_4/\text{Al}$ lift-off. Metal parts are seen as dark areas; light-grey areas correspond to the gaps separating metal structures. The resulting central line is open due to a fabrication defect. The broken link is pointed with a white arrow.

an unwanted open spot behind (see Fig. 5.7 (d)). That is why, the processed chips showed no trace of conductance. To increase the lift-off quality and avoid dust particles in the BOE bath, it worth trying to do the lift-off in a separate teflon container with BOE solution and not in the common bath.

Trenches in a substrate

To enable fault-free wafer scale designs with micrometer structures and high yield device production, there is a common technique for eliminating dust inclusions by planarization. The CMP damascene process permits to manufacture metallic structures with a controllable thickness down to 3 nm and a width down to 15 nm. Also, the resulting structures have vertical sidewalls [107].

Accordingly, we tried to complement our workflow with the CMP process.

5. Kinetic Inductance Traveling Wave Parametric Amplifier

To pursue this major technological advance, first the whole structure had to be buried in trenches in the substrate. Different techniques had been tried to develop trenches in the substrate. The main task was to find a way of producing trenches with high aspect ratio ($1 \mu\text{m}$ wide : 300 nm deep), with vertical walls and a uniform floor.

The prepared wafers were sent to Canada for the CMP process, within a collaboration with a group in University of Sherbrooke. Unfortunately, the process turn-around time was too long to yield in measurable devices that can be reported in this thesis.

5.4.2 Measurements

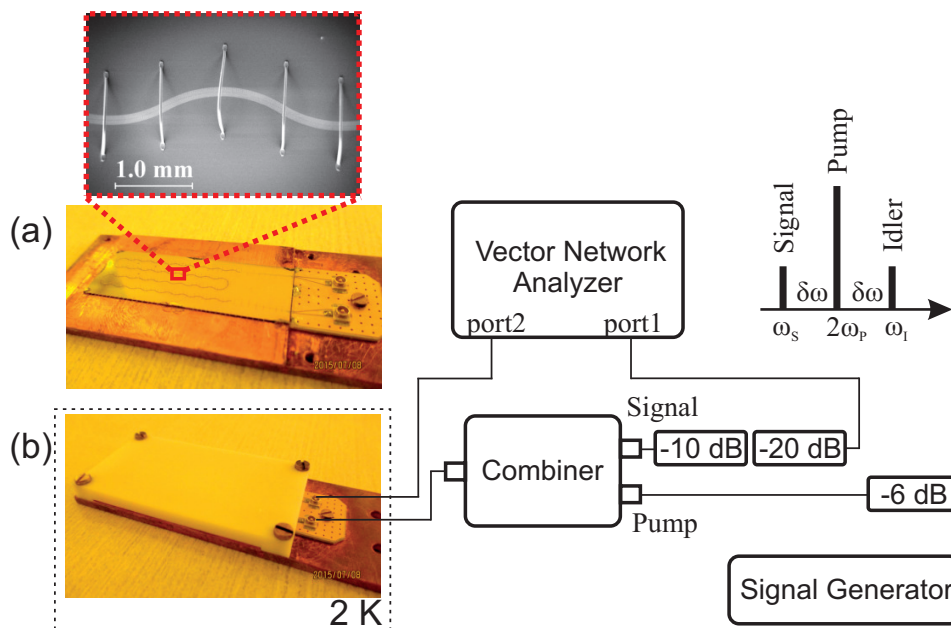


Figure 5.8: KI-TWPA gain measurement setup. (a) The chip with design 3 mounted on a copper plate and bonded heavily, as shown in inset. (b) The gain measurement setup of the KI-TWPA chip, closed with a teflon cover. Measurements were done at 2 K in a He gas-flow cryostat.

KI-TWPA chip was glued on a copper plate and many bonds were added across the line and around the chip perimeter, also the input/output terminals were bonded to 50Ω lines on a PCB (Fig. 5.8 (a)). The chip was protected with a teflon cover, mounted on a dip-stick (Fig. 5.8 (b)) and dipped in a He gas-flow

5. Kinetic Inductance Traveling Wave Parametric Amplifier

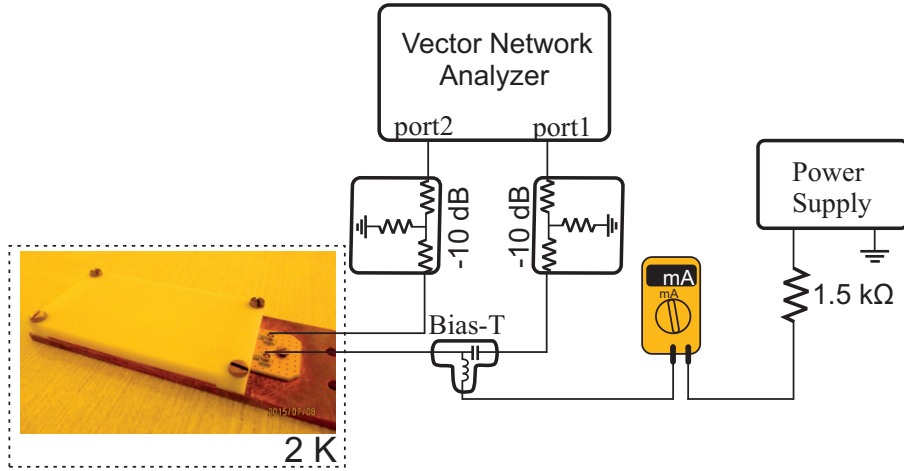


Figure 5.9: DC measurement setup of KI-TWPA chip at 2 K in a He gas-flow cryostat. DC bias was applied to sample input through a Bias-T. At room temperature sample input and output were attenuated with -10 dB. Sample S_{21} amplitude and phase were measured with VNA.

cryostat. The measurements were performed at approximately 2 K.

For gain measurements, the strong Pump tone from a Signal Generator was combined with a weak Signal tone coming from VNA and was sent to the amplifier input. The amplifier output was sent to VNA and device S_{21} transmission amplitude and phase were measured.

To characterize the line nonlinearity, the sample was dc biased through a Bias-T (Fig. 5.9). Chip input and output were attenuated with -10 dB attenuators placed at room temperature. The S_{21} phase curves were recorded as a function of dc current bias.

5.5 Results

Now we will motivate the steps which eventually lead us to our final design and will present the results of the design evolution. First, we verified that we can produce NbN lines of high quality that can be pumped into a nonlinear regime without breaking superconductivity. To this end we have fabricated lumped element resonators with 140 nm NbN film and have demonstrated that we can get a considerable resonance frequency shift at high excitation amplitudes (Fig. 5.10).

5. Kinetic Inductance Traveling Wave Parametric Amplifier

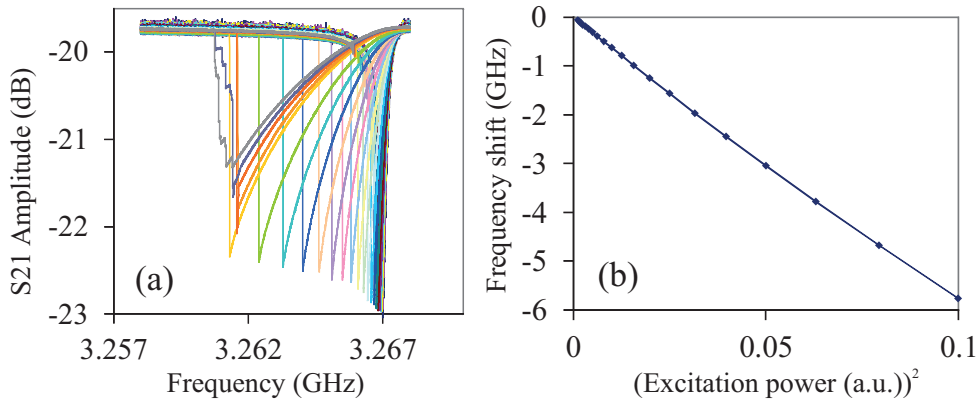


Figure 5.10: (a) S_{21} amplitude of a line loaded with lumped element resonator, defined in a 140 nm NbN film. Different plots correspond to different excitation powers with 1 dBm increment. Frequency was swept from high to low values due to Duffing type resonance lineshape. (b) Resonance frequency shift Δf , extracted from (a), versus excitation power squared P^2 . As expected $\Delta f \sim P^2$.

Design 1 After assuring the high quality of our films, we have turned to Design 1 - a standard CPW line shaped as a meander, similar to the one in the original work in Ref. [24]. The measurement results are presented in Fig. 5.11 (a-b). We get an average gain of around 7 dB, but with 0.5 m long line, which translates into per unit length gain similar to that in [24]. However, similar to the original work, there are 10 dB large ripples on the transmission due to impedance mismatch caused reflections in the line (Inset in (a)). As a result, the gain is frequency dependent, bouncing from 0 dB to 20 dB. Apart from the ripples, there are also non-periodic spikes in the spectrum due to coupling to ground plane resonances. For this reason, it is not possible to clearly locate the dispersion engineered stop bands (see Fig. 5.11 (a)).

Design 2 The motivation for Design 2 was to reduce the line impedance in order to match it with in/out terminal 50 Ω impedances. Thanks to the increased fractal capacitance, we managed to reduce the line high impedance and eliminate ripples up to 2 GHz. To fit 145 mm long line on a 2'' wafer, we have implemented the fractal line with 90° turns. Additionally, the turning arcs with no-fractal sections were made to provide dispersion engineering, as explained earlier.

The resulting transmission was found to be flat at low frequencies, as shown

5. Kinetic Inductance Traveling Wave Parametric Amplifier

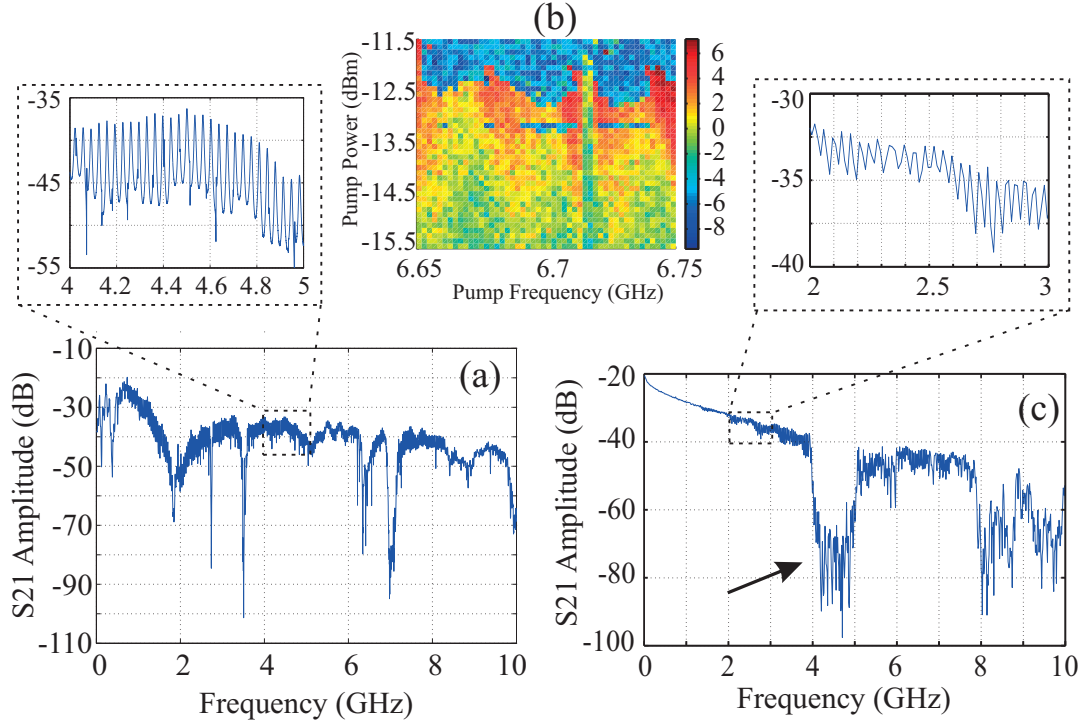


Figure 5.11: (a) Design 1: 140 nm thick and 0.5 m long NbN line. Transmission S_{21} versus frequency. Inset: zoom-in on ripples. (b) The gain averaged over a Signal frequency window of 6.34 – 6.35 GHz versus Pump power/frequency for Design 1. The period of gain modulation is the same as for transmission ripples in the Inset. (c) Design 2: prototype KI-TWPA built on a 145 mm long line with 337 rad electrical length at 4 GHz. Device transmission S_{21} . The arrow points at the dispersion stop band with a spiky floor. Inset: zoom-in on residual ripples above 2 GHz.

in Fig. 5.11 (c). However, judging from the residual ripples (Inset in (c)), one can tell that the line is not completely impedance matched yet. It would not be a big problem to boost the fractal capacitance even further to get a perfect impedance match, but this design revealed another serious problem. While the dispersion band centered around 4.5 GHz is more or less clear now, the band around 8.5 GHz is poorly defined. Also both bands have spiky floors (Fig. 5.11 (c)), which is far from the shape of the expected band from simulations (Fig. 2.10). This is a result of abrupt 90° turns in our design. Any continuity break strongly couples to spurious resonances and has a detrimental effect on the dispersion bands.

An attempt to run the amplifier with a Pump frequency tuned close to the first dispersion band resulted in a very low gain (< 2 dB) because at 4 GHz the

5. Kinetic Inductance Traveling Wave Parametric Amplifier

electrical length of the line was too short (337 rad) to get significant nonlinear phase shift $\Delta\theta$. A higher electrical length at the second dispersion band, in principle, should have provided some gain, would the band be properly defined.

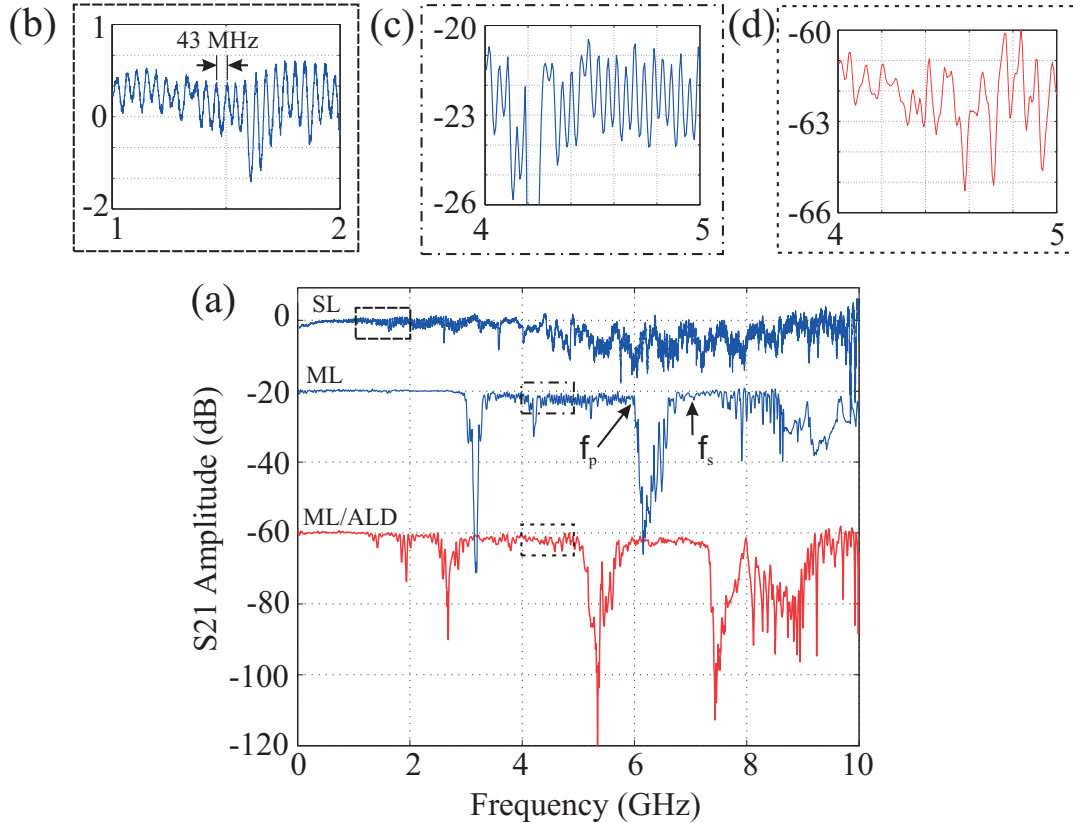


Figure 5.12: Design 3: 114 mm long fractal line, design as in Fig. 5.4. (a) Transmission S_{21} versus frequency. 'SL'-Design 3a, 'ML'-Design 3b, 'ML/ALD'-Design 3b after ALD oxide deposition. (b) Zoom-in on (a), 'SL'. (c) Zoom-in on (a), 'ML'. (d) Zoom-in on (a), 'ML/ALD'.

Design 3 With Design 3 our aim was to extend the ripple-free region to higher frequencies by boosting the fractal capacitance and achieving line impedance close to 50Ω in order to get the line matched to in/out terminals. We have achieved this after few design-fabrication iterations (as its hard to know beforehand the value of KI), which guided us towards the right amount of fractal capacitance for balancing the high KI of the line. Also, we aimed at suppressing the ground plane resonances. As explained earlier, an attempt to implement dispersion engineering by removing sections of fractal pattern in Design 2 resulted in strong

5. Kinetic Inductance Traveling Wave Parametric Amplifier

coupling to ground plane resonances. In order to minimize line coupling to spurious resonances, we decided to revert back to dispersion engineering by line width modulation.

The S_{21} spectrum of the line fabricated with a single NbN layer (Design 3a) is shown in Fig. 5.12 (a), labeled as 'SL'. From average ripple amplitude of ~ 1.5 dB (Fig. 5.12 (b)), we can estimate $\sim 70 \Omega$ line impedance in the following way:

$$\begin{aligned} 20\log(S_{21}) &= 1.5 \text{ dB}, S_{21} = 1.19, \\ S_{21} = 1 + S_{11} &= 1 + \frac{Z - 50}{Z + 50} = 1.19, \\ Z &= 73 \Omega. \end{aligned} \tag{5.1}$$

Although the line is close to being impedance matched, the spectrum is full of aperiodic features. Here we have realized that as soon as the ripples due to line edge reflections were eliminated, the next design challenge was to get rid of ground plane resonances. This issue was addressed with the multilayer fabrication technology (Design 3b).

As discussed in section 5.4.1, paragraph Design 3, to upshift the spurious ground plane resonance spectrum, we fabricated the ground plane (also the fractal capacitors and the tapers) as a low-inductive film in Design 3b (Fig. 5.4 (c)). The S_{21} spectrum of the line with impedance of $\sim 70 \Omega$, fabricated with a multilayer technology, is shown in Fig. 5.12 (a), labeled as 'ML'. With the multilayer technique it becomes easier to simulate/predict the behavior of fractal elements and the tapers due to the absence of kinetic inductance. Most importantly, it becomes possible to remove the aperiodic spikes from the operation range of the amplifier. Hence, the transmission is much cleaner up to 8 GHz with well-defined first and second band gaps, that are narrow and sharp as expected. Alas, the third band expected at 9.5 GHz is still not well-defined. This we relate to residual ground plane resonances that still couple to KI-TWPA line at high frequencies. The poorly defined $3f$ highest band is quite alarming, because it aims to block shock waves generated by the $3f_P$ harmonic of the strong Pump tone [108]. If measures are not taken, then the growth of shock waves will destroy the superconductivity in the line.

As explained earlier, because it is difficult to predict the exact value of KI

5. Kinetic Inductance Traveling Wave Parametric Amplifier

in advance, a few design/fabrication iterations were needed to reach the desired line impedance. In particular, Design 3b appeared to have an impedance of $\sim 70 \Omega$. Instead of committing to another design iteration, we tried to tune the line impedance to exactly 50Ω by depositing ~ 200 nm of ALD Al_2O_3 oxide on top of the sample to slightly increase the capacitance. The resulting S_{21} spectrum is almost ripple-free (the red plot in Fig. 5.12 (a), labeled as 'ML/ALD' (multilayer with ALD)). Due to the increased capacitance and reduced propagation velocity (from $\nu_p = 0.033c$ to $0.023c$), the bands have moved to lower frequencies and the highest band is more clear now. As can be seen in Fig. 5.12 (a), some residual features are still present even for the multilayer design. We attribute these to either coupling to some box or spurious ground plane resonances linked to large chip size and increased transverse dimensions of the fractal design ($\sim 120 \mu\text{m}$), remaining as a subject for further investigation.

5.5.1 Kinetic inductance nonlinearity and parametric gain

As mentioned earlier, we assumed an amplifier line with L_k kinetic inductance dominating over its L_m geometrical inductance. In the calculation presented in Appendix C, we arrive at $L_k \approx 7L_m$.

Having this in mind, the nonlinear properties of our KI-TWPA line in Design 3b were tested by tuning the KI with a dc bias current. The resulting plot is demonstrated in Fig. 5.13 (a). The plot is fitted to a parabola $\Delta\theta = aI^2$ with a fitting coefficient $a = 2.45 \text{ mA}^{-2}$ extracted from the fit (see section 2.3.4). With the electrical length $\theta \approx 427$ rad, known from Eq. (2.67), we get that the nonlinearity parameter $I_* = \sqrt{\theta/2a} = 9.3 \text{ mA}$ from Eq. (2.68). The achieved maximum nonlinearity in our KI-TWPA line $\Delta\theta/\theta \sim 1 \%$ is higher than that of 0.7% achieved in the original work [24]. The critical current of our line is 1.3 mA , which is comparable to numbers in literature [109] and confirms the high quality and uniformity of the line.

Similar to Refs. [24, 25, 106], in our case also the dispersive shift close to the first band was found to be insufficient to compensate for the line nonlinearity. Therefore, we pumped at ~ 6 GHz and measured parametric gain for Signal frequency range of $(7-7.2)$ GHz (Fig. 5.13 (b)). With a line as short as ~ 10 cm,

5. Kinetic Inductance Traveling Wave Parametric Amplifier

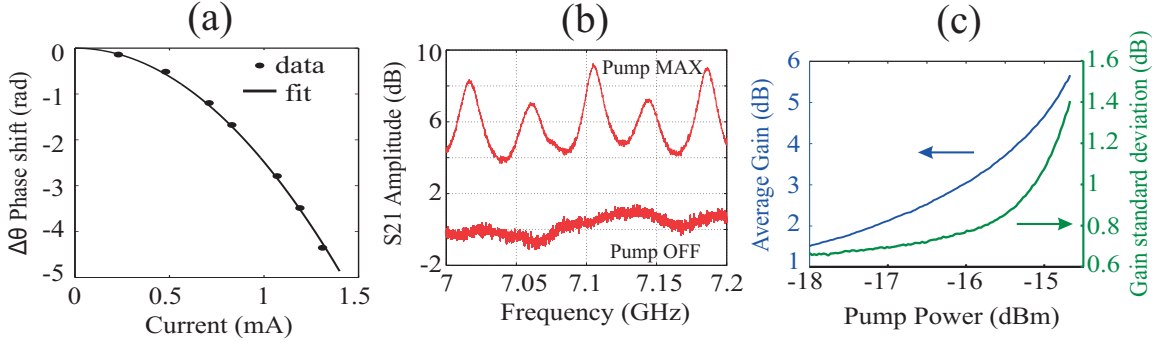


Figure 5.13: Design 3b, 'ML'. (a) Nonlinear phase shift measured at 5.9 GHz as a function of dc bias. (b) Device transmission at zero Pump power (bottom) and maximum Pump power just before the breakdown of superconductivity (top). Average gain is ~ 6 dB, maximum Pump power is -14.7 dBm. (c) Average gain (in blue) and gain standard deviation (in green) versus Pump power.

we have achieved an average gain of ~ 6 dB. This is to be compared against the 10 dB gain in [24] with 0.8 m long line. Though we have achieved a per unit length gain (0.5 dB/cm) higher than ever reported, it is still below the number expected from the measured line nonlinearity (~ 1 dB/cm). Indeed, looking back to the gain equation $G_s = \frac{1}{4}e^{2\Delta\theta}$ and inserting the nonlinear phase shift of the Signal $2\Delta\theta = 4.5$ rad, we arrive at $10\log(G_s) = 13$ dB gain, which is almost a factor of five more in power gain than 6 dB. Below we will describe possible reasons for this discrepancy.

We see that when the Pump power approaches the maximum, just 1 dB below the superconducting to normal transition power (-14.7 dBm), ripples start to develop on the originally flat transmission, as shown in Fig. 5.13 (c)¹. Notably, the ripple amplitude is moderate, ~ 3 dB large as compared to more than 10 dB ripples in [24]. Still, even moderate ripples result in standing wave formation and premature breakdown of superconductivity, thus limiting the maximum Pump power and the gain. Its unclear why on initially ripple-free transmission ripples start to develop with increasing Pump powers. We speculate that this unexpected behavior can be attributed to three likely gain limiting factors: first, at high powers the line enters an extremely nonlinear regime, which can not be

¹The gain standard deviation was calculated as $\sigma = \sqrt{\frac{1}{n} \sum_{i=1}^n (G_i - \bar{G})^2}$, where G_i is the gain at a frequency f_i , \bar{G} is the average gain and n is the number of frequency points.

5. Kinetic Inductance Traveling Wave Parametric Amplifier

treated anymore within the framework of a simplified model for the exponential gain, given by Eq. (2.64). Second, the Pump tone gets partially reflected on the dominant weak spot (the weakest point) in the line. As a proof, we have found that when measuring from opposite in/out directions, the gain varies by $(2-3)$ dB as a function of Pump frequency. This is presumably because the effect of pumping is different when the weak spot is positioned slightly asymmetrically with respect to line in/out terminals. $(2-3)$ dB amplitude variation is a characteristic number hinting how much the gain can be potentially improved with a perfectly homogeneous line, giving a number around 10 dB for the maximum gain. This number would be on the same page as the gain value calculated from the exponential gain equation. We conclude that for a maximum gain the line homogeneity (thus the short length) is crucial. Finally, the third factor is the following: the coupled-mode theory considers three modes: Pump, Signal, and Idler. In our case we supply only Pump and Signal to the amplifier input. The Idler builds up via amplified vacuum fluctuations at the Idler frequency. It takes some time (i.e. some portion of the line) for the Idler to rise, and only after that the coupled-mode theory applies. As a result, the effective line length used in formulas coming from coupled-mode theory is somewhat shorter than the physical length, thus accounting for the gain discrepancy.

5.6 Summary & Outlook

In summary, with our slow propagation KI-TWPA line we managed to reduce the wave propagation velocity down to 3% of the speed of light and demonstrate a parametric gain with suppressed ripples. Our per unit length parametric gain is ~ 0.5 dB/cm, which considerably exceeds that in [24] (~ 0.1 dB/cm) and in [25] (~ 0.05 dB/cm). The most important achievement is that we have obtained the mentioned gain with only ~ 10 cm long line, almost seven times shorter than the line in [24] and twenty times shorter than the line in [25]. Up to date such an amplifier arguably stands the closest to a practical (industrial grade) quantum-limited amplifier operating at temperatures of ~ 2 K.

We claim that there are few factors contributing to the achievable nonlinearity, maximum Pump power and frequency independent gain. The elimination of

5. Kinetic Inductance Traveling Wave Parametric Amplifier

impedance mismatch caused standing waves is the first in this list. Balancing the high KI of the line with increased fractal capacitance results in transmission spectrum free of Fabry-Perót type ripples. The short length of the line (still long enough to have sufficient gain), obtained via reduced propagation velocity, comes next in this list. We have demonstrated that a short line is more robust, homogeneous and less prone to fabrication-induced weak spots. The third factor is the high quality and uniformity of the high aspect ratio line, which was a separate challenge to overcome with the multilayer fabrication technology. Line uniformity and quality have directly transformed into high KI nonlinearity, larger than that in [24], even with such a short line. Last, but not the least the significantly suppressed ground plane resonances must be mentioned that was achieved thanks to the versatile multilayer technique. Our results of notably cleaner transmission spectra and dispersion engineered bands with sharp and narrow floors further support this point.

In what follows, we will conclude with a summary of prospective ways to further improve the amplifier performance.

- **Ways to increase the parametric gain** So far we have demonstrated that with our ~ 10 cm long fractal KI-TWPA line ~ 10 dB parametric gain is feasible. However, for cascading with commercially available semiconductor amplifiers, 16 dB gain is required. We see the following directions for boosting the gain of KI-TWPA.
 - ***A more profound Dispersion engineering*** The positive curvature of the gain vs. Pump power plot (Fig. 5.13 (c)) indicates that a stronger dispersive shift should boost the gain even further. One could take advantage of the multilayer technology and implement line impedance perturbation by combining central strip sections with and without kinetic inductance. Deploying kinetic inductance as a design parameter, it is possible to arrange 2-3 fold steps in line impedance; simulations show that the resulting dispersion should be more than adequate.
 - ***Longer line*** Another obvious way to get a higher gain is to make the line longer. With a fractal design, this will not be easy, as the longer

5. Kinetic Inductance Traveling Wave Parametric Amplifier

fractal line will have more fabrication defects (weak spots and shorts), degrading device yield. This calls for better clean room conditions.

- **High device yield** To obtain longer line we need to keep the yield of wafer-scale designs with micrometer structures at the acceptable level (currently $\sim 60\%$), device processing must be further mastered. That includes, most importantly, the exclusion of custom FIB treatment of shorts from the workflow. Possible spin-off fault-tolerant directions, discussed in Section 5.4.1, are the lift-off and CMP processes. Also, the outsourcing of a lithography mask for the fractal design must be considered.
- **Noise characterization** As soon as the parametric gain is boosted up to 16 dB, TWA noise characterization should be performed to demonstrate that the noise level is indeed approaching the quantum limit.
- **Ways for cleaning up ground plane resonances** To reduce the spurious resonances due to large transverse dimensions of the fractal design with a meander shape, one should consider implementing a 6'' wafer, which could fit a straight fractal design.

Also, $1\mu m$ design rule could be reduced to $0.5\mu m$. This means that the whole design will downscale twice. Assuming the leading coupling term to be dipole, downscaling the design size twice should suppress residual resonances by 6 dB (as dipole coupling is proportional to the size squared and twice smaller size will translate into a four times smaller coupling). To afford such an advancement in fabrication workflow, without shorts degrading the device yield, a higher class clean room environment will be necessary.

An alternative direction is to develop a fractal-free KI-TWPA. This approach is further discussed in the next section 5.7.

To conclude, fractal slow propagation lines potentially can be used for on-demand engineering of propagation velocity and impedance via combined high and low kinetic inductance elements in the same microwave circuit. Hard to implement via conventional CPW TL's, this will become possible via a fractal TL fabricated with a multilayer technology. Such an on-demand engineering can be applied

in step-impedance filters, as well as devices, that need long electrical lengths: parametric amplifiers and phase shifters.

In addition to the NSMM and ESR techniques, a great variety of fundamental and applied research fields will immediately benefit from a quantum-limited amplifier, just to list a few: Microwave Kinetic Inductance Detectors (MKIDs) for astrophysics [110], photon detectors [111], and the whole emerging field of quantum computing and cryptography [7].

5.7 The quest for an alternative to the coplanar design

In the experiments described above, introducing an increased fractal capacitance in the CPW design, we have succeeded in achieving various goals set in front of us. We have learnt also that in case of the KI-TWPA, the fractal design unfortunately has intrinsic drawbacks, limiting the maximum achievable gain and device performance. First, due to a long perimeter and micrometer wide gaps in the superconductor, the fractal design is prone to fabrication shorts. Such shorts may happen during any fabrication step and a single short is enough to make the whole device useless. Second, due to its large transverse dimensions ($\sim 120 \mu\text{m}$), fractal line couples to ground plane resonances that overlap with the device transmission spectrum. Although sparse, such resonances are not tolerable for many practical applications and need to be suppressed. An alternative way of reducing the propagation velocity, that would help in overcoming these drawbacks, is the microstrip line.

The interest in microstrip lines was large back in 1960's. The reason was the discovery made by Pippard [112]: it was possible to slow down the wave due to the high kinetic inductance of superconducting thin film TL. This finding was followed by many trials of implementing superconducting microstrip lines for delay line-based signal processing applications [112, 113]. The main motivation behind these trials was the simplicity, low cost and improved reliability of signal processing functions due to the miniaturization of the signal carrying line. Whilst the primary interest was in the slowest, but loss-less microstrip lines, unfortunately

5. Kinetic Inductance Traveling Wave Parametric Amplifier

none of the trials led to microstrip lines with low enough dielectric loss. Hence, due to poor quality factors and the lack of systematic study of the loss characteristics, microstrip designs were not used in the fields of c-QED and quantum computing.

Later in 2000's, the possibility to use microstrip lines for kinetic inductance detector applications inspired new experiments [114]. Except the conventional way of producing a microstrip line (Fig. 2.5), one could instead have all three layers on the same side of the substrate. To achieve increased capacitance this way, the intermediate dielectric layer needed to be thin film. Notably, the resulting device was even more compact as compared to CPWs, due to the reduced dielectric thickness (for a 50Ω line ~ 25 nm thick as compared to $2 - 10 \mu\text{m}$ gap in CPW). Furthermore, the high kinetic inductance of the superconductor translated into the improved sensitivity of the detector [115]. However, the quality of deposited thin film dielectric seemed to be still inferior to the quality of bulk sapphire, commonly used in CPW designs.

For the development of a fractal-free KI-TWPA, this kind of modified microstrip design seemed to be the right route towards achieving increased capacitance. Except the low-loss thin film dielectric, we needed also to find out how much of KI nonlinearity the microstrip line could deliver. In order to check both, the easiest way would be to make a tunable microstrip resonator. The Q-factor of such a resonator would characterize the dielectric quality. On the other hand, the obtainable frequency shift would serve as a measure of line nonlinearity.

Frequency tuning was another functionality, that made CPW resonators attractive for experiments with photon storage and release [116], dynamic coupling of quantum bits [117], etc. While a common approach to make the frequency of CPW resonator tunable was to combine it with a SQUID, such an approach suffered from losses due to the SQUID and required sub-1 K temperatures [118]. Another approach was to tune the frequency with a magnetic field, via the kinetic inductance intrinsic to the superconducting material. This kind of tuning was possible with much higher CPW Q-factors, but with limited tuning range as compared to the previous approach (3 MHz versus 700 MHz) [119]. Instead of using magnetic field, the frequency (via kinetic inductance) could be controlled also with a current bias. The first implementation of this idea, however, resulted

in a much slower tuning than that achievable with SQUIDs (1 ns) [52].

Clearly, the development of a tunable microstrip resonator was a challenging trade-off between the Q-factor, the range and the time of frequency tuning.

5.8 Challenges to be addressed in Tunable Microstrip Resonators

- Development of microstrip resonators with deposited oxide as the thin film dielectric layer.
- Loss characterization of microstrip resonators.
- Incorporation of low radiative dc bias lines into the resonator design.
- Realization of fast and wide-range frequency tunability.

5.9 Slow propagation microstrip lines

To cope with the Q-factor/tuning range/tuning time trade-off and to avoid the disturbing issues introduced with the fractal design, we went for the slow propagation microstrip line design shown in Fig. 5.14. To achieve increased capacitance, the thickness of the intermediate dielectric film must be well below micrometer (~ 25 nm for a 50Ω line). Therefore, all three layers of the microstrip (top conductor, thin film dielectric, ground conductor) must be on the same side of the substrate (sapphire).

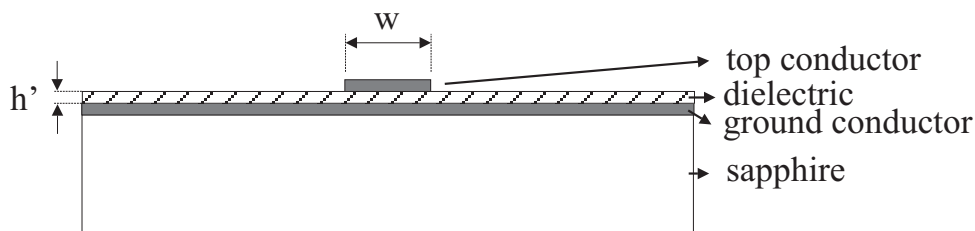


Figure 5.14: Microstrip transmission line with top, bottom conductors and intermediate thin film dielectric layer on the same side of sapphire (w is the width of top conductor, h' is the thickness of thin film dielectric).

5. Kinetic Inductance Traveling Wave Parametric Amplifier

More specifically, our actions were initially based on the following presumptions.

- To obtain a high-Q thin film dielectric, atomically deposited ALD aluminum oxide was chosen. The choice of ALD aluminum oxide was motivated by comparatively low loss tangents of 2.7×10^{-5} , reported in literature [120]. The high quality ALD oxide was expected to be the best candidate for the development of a low-loss microstrip resonator, given that one could develop a perfected fabrication process to make sure the absence of pinholes and defects in the ALD oxide.
- To this point it was clear that the design would be much more simple and flexible as compared to CPW designs and thus would enable the integration of dc bias lines for tuning the resonator frequency. Whether after the introduction of bias lines it would really be possible to tune the frequency while keeping the Q-factor not deteriorated by radiation losses, was still questionable.
- The increased capacitance reduces the line propagation velocity, significantly shortening the TL length ($\lambda = v_p/f$). This kind of slow propagation line, as compared to conventional CPW lines, would facilitate the future development of more compact KI-TWPAs.
- If the deposited dielectric layer is thin enough, the increased capacitance could balance the high KI of the KI-TWPA line, solving the impedance mismatch issue.

5.10 Experimental Techniques

5.10.1 Microstrip resonator design concepts

To characterize the losses in the resonator, the simplest possible design #1 was made as a reference (Fig. 5.15 (a)). Design #1 comprises a $\lambda/2$ microstrip resonator capacitively coupled to a CPW feedline at its voltage antinode.

5. Kinetic Inductance Traveling Wave Parametric Amplifier

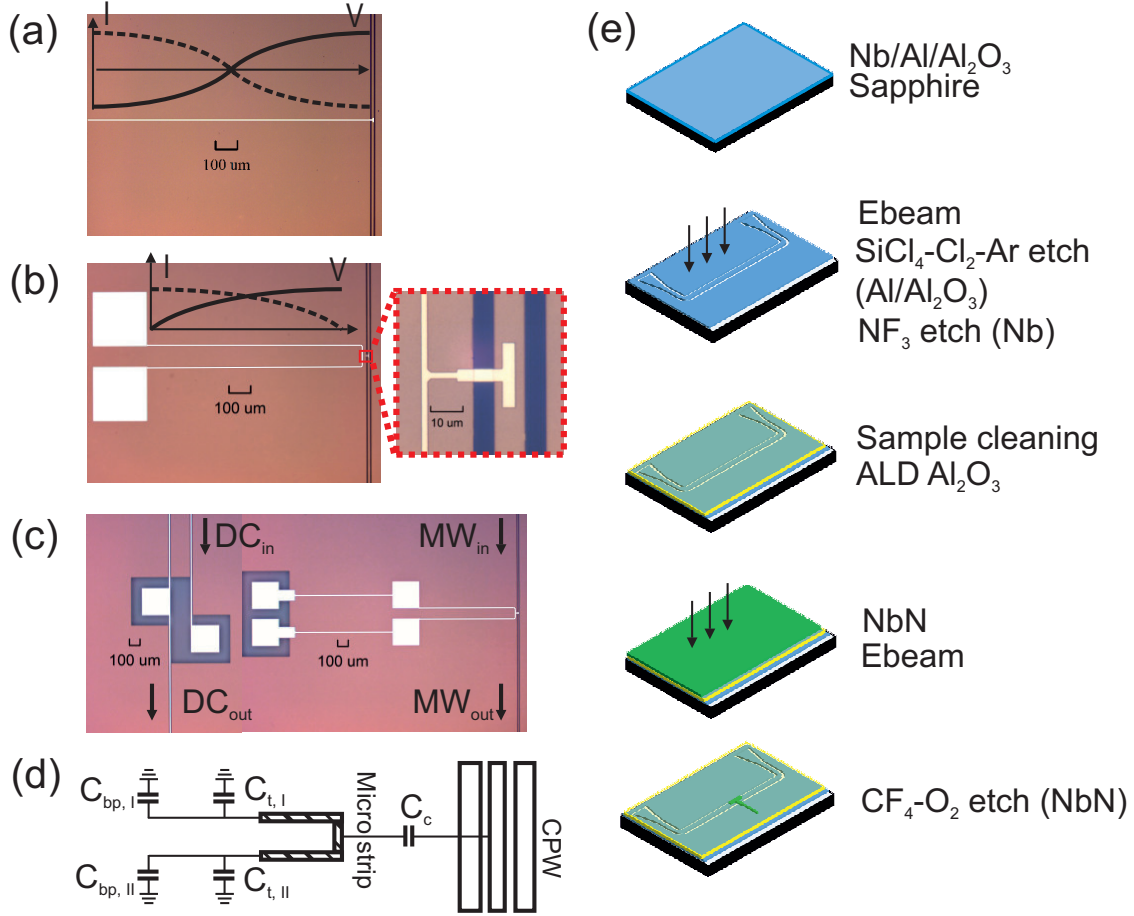


Figure 5.15: (a) The simplest design #1, created for loss characterization, is a $\lambda/2$ resonator capacitively coupled to CPW feedline. The voltage and current modes are sketched above. (b) Design #2 is a folded $\lambda/2$ resonator with shunt to ground capacitive terminations. The voltage and current modes are sketched for a single $\lambda/4$ prong of the resonator. (c) Design #3, with bonding pads coupled to the shunt capacitors. The dc bias lines for frequency tuning, to be bonded to resonator pads, are located on the most left. (d) The schematic representation of the resonator in (c). (e) Fabrication step sequence for producing microstrip resonators.

In the next design generation (#2), we terminated both ends of the resonator with large shunt capacitors to check if this would cause any reduction in Q-factor due to dielectric losses in capacitors (Fig. 5.15 (b)). The second design #2 is also a $\lambda/2$ microstrip resonator, but with the capacitive terminations at its voltage nodes. The resonator is capacitively coupled to CPW feedline at its middle point and can be represented as two $\lambda/4$ microstrip sections connected in series. As this $\lambda/2$ resonator is coupled in the middle point, only the symmetric modes will

5. Kinetic Inductance Traveling Wave Parametric Amplifier

be excited, so the excitation spectrum will be the same as for $\lambda/4$ resonator. For the first design all the modes must be observable.

Finally, the last design version (#3) served in testing the KI nonlinearity (Fig. 5.15 (c)). To this end, design (#3) had additional bonding pads in parallel with shunt-to-ground capacitive terminations, to enable the dc bias tuning of the resonator frequency. The shunt capacitors provide short to ground at microwave frequencies, while allowing the dc tuning of KI. Effectively, the capacitors behave as low-pass filters, transmissive for a dc control. The schematic representation of design #3 is sketched in Fig. 5.15 (d). To avoid shorts through the ALD oxide, a window was opened in the ground plane conductor, so that the top conductor of bonding pads could directly be deposited on sapphire. The microstrip line in design #3 is 2 μm wide and 2280 μm long.

5.10.2 Microfabrication of Microstrip Lines

We have fabricated and measured three different devices corresponding to designs illustrated in Fig. 5.15 (a-c) respectively. Microstrip resonators have been implemented with Nb/Al/Al₂O₃/NbN structure on a 2" sapphire wafer (Fig. 5.15 (e)). Nb acts as the ground plane conductor of the microstrip line and NbN as the top conductor. The thin Al layer on top of Nb initiates a high-quality oxide in the following step. Finally, the Al₂O₃ is the thin film dielectric deposited with ALD.

First Ti/Au (10/140 nm) alignment marks were made on the wafer. Next, Nb/Al (50/10 nm) was sputtered over the wafer in a near-UHV sputter system. For the uniformity of the films, sputtering was done with a rotating sample stage. Right after the chamber was filled with Oxygen, while keeping the Argon flow shut and the sample was left in the oxidized chamber for 10 min at 170°C, resulting in an estimated thickness of Al₂O₃ to be about ~ 5 nm. After e-beam patterning of the Nb/Al/Al₂O₃ layer, the developed regions of the wafer were etched in RIE plasma system: first Al/Al₂O₃ with SiCl₄/Cl₂/Ar gas mixture for 1 m 40 s and then Nb with NF₃ gas for 1 m 10 s. After etching, the resist was removed with 65°C Remover for 20 min and O₂ ashing. For having a high quality dielectric, we deposited 50 nm of ALD aluminum oxide. On top of ALD Al₂O₃, 50 nm of

5. Kinetic Inductance Traveling Wave Parametric Amplifier

NbN was sputtered. After e-beam patterning of NbN layer, the developed and opened-up areas were etched in a preconditioned chamber with CF_4/O_2 mixture for 2 m 30 s. The chips were diced away and cleaned in a 65°C Remover for 20 min. See Appendix B for more fabrication details.

5.10.3 Measurements

Devices #1, #3 were measured in a He^3 cryostat at 300 mK, and device #2 was measured in a He^4 gas-flow cryostat at ~ 2 K. The cryogenic 300 mK setup is illustrated in Fig. 5.16. The sample was glued on a PCB and mounted inside a copper box. The microwave probe line was attenuated by ~ 72 dB to suppress high temperature radiation on the way towards the sample. A twisted pair (thermalized through a low-pass filter $10 \Omega \times 10 \mu\text{F}$) was used for dc biasing the sample. The signal transmitted through the sample was first amplified with a cryogenic HEMT amplifier, amplified again at room temperature and then feeded to VNA. All the expected resonance harmonics were observed with high reproducibility.

We have measured the S_{21} transmission through resonators. To extract the Q-factor of capacitively coupled microstrip resonators, we used expressions, similar to the ones derived earlier in section 2.2.2 for inductively coupled resonators. The resonance lineshape was fitted to a Lorentzian (see chapter 2, section 2.2.2),

$$S_{21} = 1 + S_{21,bckg} - \frac{(1 - S_{21,min})}{1 + 2jQ_t \frac{\Delta\omega}{\omega_0}}, \quad (5.2)$$

where $S_{21,bckg}$ is a complex parameter accounting for an asymmetrical resonance lineshape due to background transmission. This term becomes particularly noticeable when tunable resonator frequency matches the frequency of some ground plane resonance on a chip.

5. Kinetic Inductance Traveling Wave Parametric Amplifier

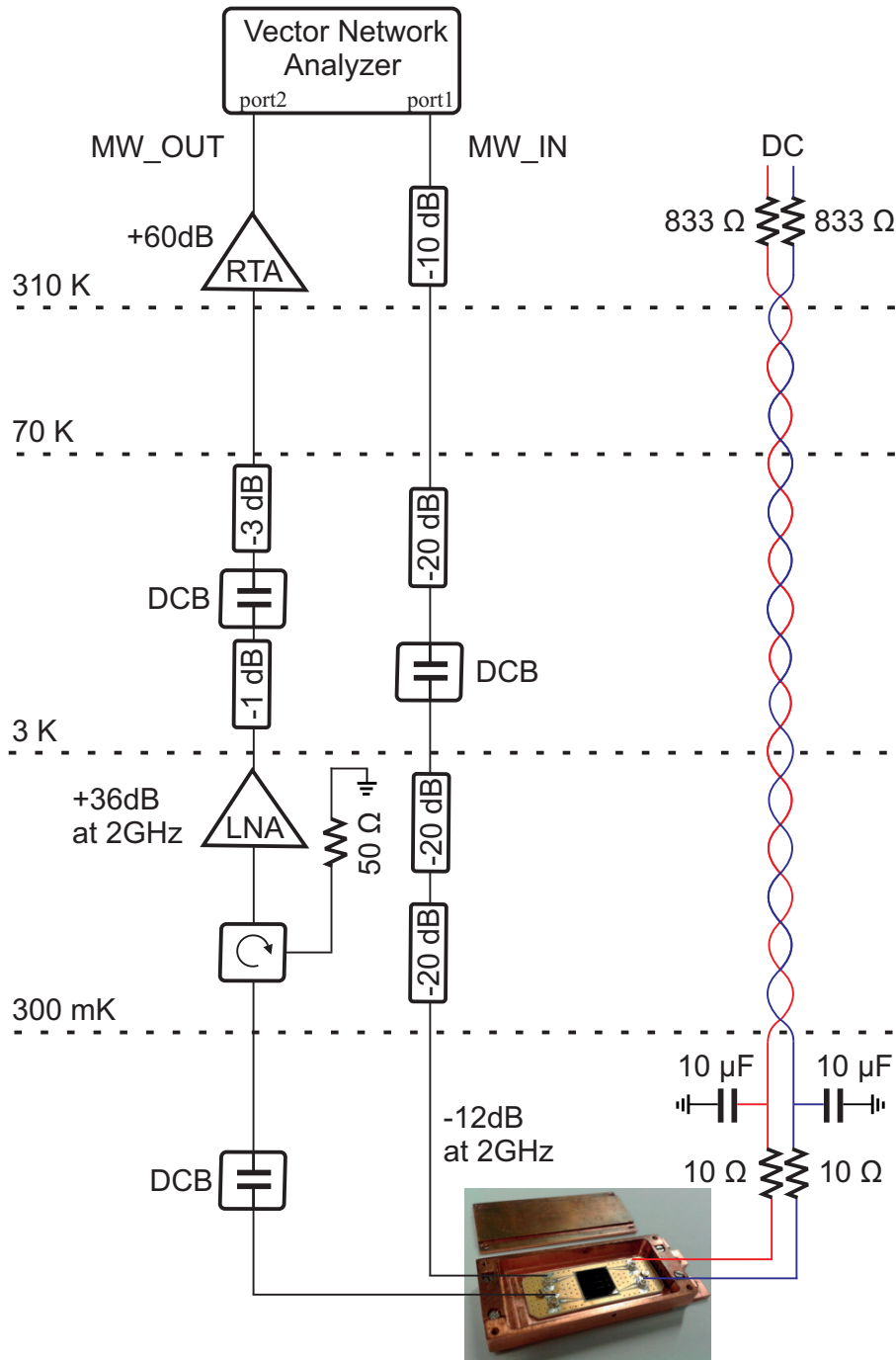


Figure 5.16: The microwave and dc measurement setup. The microwaves are sent through coaxial cables, which are attenuated to suppress radiation and provide thermalization. In the microwave output line, the circulator aims to isolate the sample from backward radiation coming from the amplifier. For dc measurements, resistive wires, combined with low-pass filters, have been used to reduce the heat conduction. At room temperature the sample was current biased through 833 Ω resistors.

5.11 Results

Thanks to our technological advance in growing high quality ALD oxide films, we have obtained microstrip resonators with high internal Q-factors of $\sim 10^4$ at single photon powers, validating the low loss tangent of the deposited dielectric (Design #1). The Q-factors are even better at increased powers, reaching the numbers of the order of $> 10^5$ for around 10 – 50 photons in the resonator, comparable to numbers reported in literature for ALD oxide [120]. The device yield is essentially 100%.

Design #2 demonstrates that the dielectric losses in the shunt capacitors are rather small, as the internal Q-factor stays around $\sim 7 \cdot 10^3$ at 2 K.

Design #3 is simple, yet versatile and allows to obtain the extra functionality of frequency tuning, maintaining internal Q-factor of $\sim 6 \cdot 10^3$. We relate this moderate decrease in Q to some power leaking into dc bias lines, possibly via increased coupling of the resonator to spurious ground plane resonances.

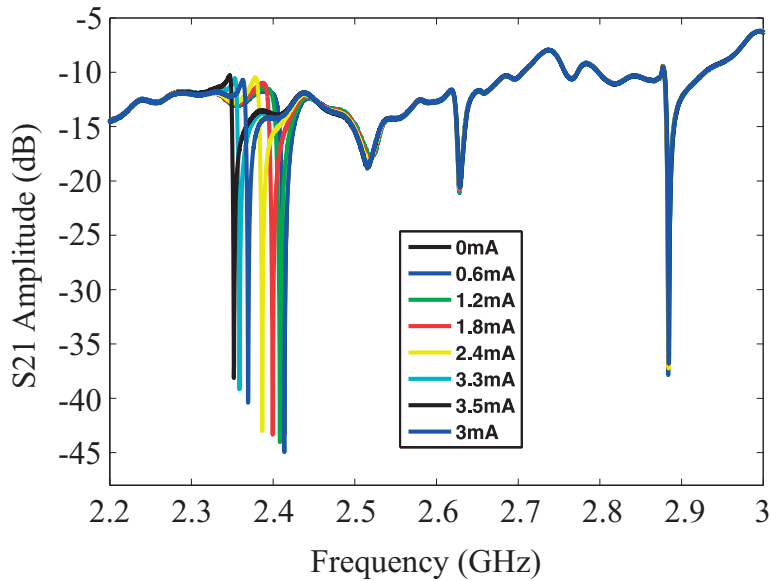


Figure 5.17: Design #3. S_{21} transmission spectrum of 3 microstrip resonators on the same chip. The resonators have resonance frequencies 2.4, 2.65, 2.9 GHz. Only the left most resonator (2.4 GHz) is connected to dc bias lines. Different colors correspond to different dc current biases in the range of (0 – 3) mA, $T=0.3$ K, excitation power = -107 dBm.

5. Kinetic Inductance Traveling Wave Parametric Amplifier

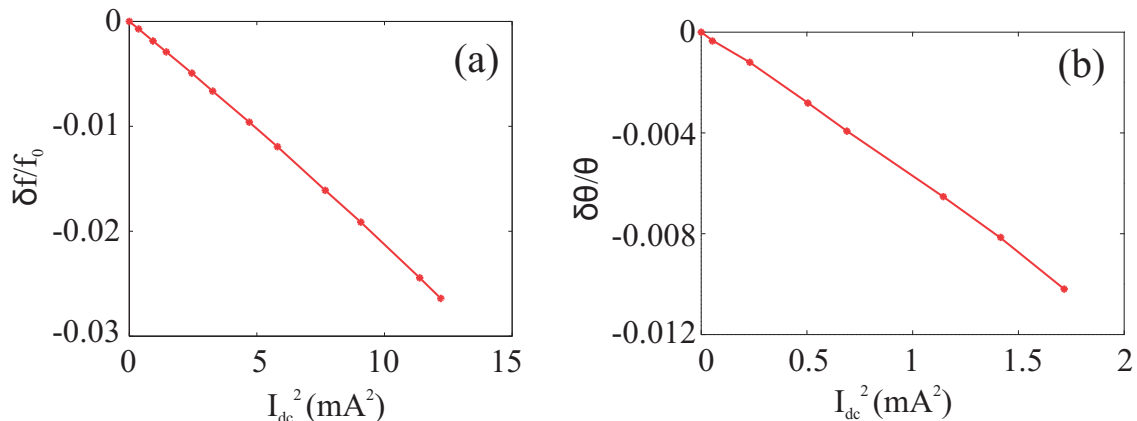


Figure 5.18: (a) The KI nonlinearity of microstrip resonator as a function of dc current squared. (b) The KI nonlinearity of ~ 10 cm long fractal KI-TWPA line as a function of dc current squared.

To test frequency tunability, on a chip containing three resonators with slightly different frequencies, the one with 2.4 GHz resonance frequency was connected to dc bias lines. The S_{21} spectrum, revealing three resonances at frequencies 2.4, 2.65, 2.9 GHz, is shown in Fig. 5.17. As expected, only the resonator with a frequency of 2.4 GHz responded to the dc control, while resonance frequencies of the other two (non-bonded) resonators were not affected.

The dc control of line KI results in a quadratic dependence of resonance frequency on dc current, as expected from KI nonlinearity (Fig. 5.18 (a)). The tunable microstrip resonator exhibits a maximum KI nonlinearity of $\delta f/f_0 = 3\%$, greater than that of 1% in our fractal KI-TWPA (Fig. 5.18 (b)) and 0.8% in the original prototype TWPA [24]. Moreover, the wave propagation velocity of this microstrip resonator ($\nu_p = 2L_{tot}f = 2 \times 2.3$ mm \times 2.4 GHz $= 0.038c$) is of the same order as in fractal KI-TWPA ($\nu_p = 2L_{tot}f = 2 \times 114$ mm \times 43 MHz $= 0.033c$), i.e. ~ 3 times slower than in conventional CPW lines. With the shunt capacitors acting as non-dissipative low-pass filters, we estimate the tuning time of the microstrip resonator to be of the order of $Z_r C_t = 3$ ns, where $Z_r = 26 \Omega$ is the resonator impedance and $C_t = 110$ pF the terminal capacitance¹. 3 ns tuning time is on the same page as that in case of CPW/SQUID approach (1 ns).

Finally, we fabricated a ~ 10 cm long microstrip line to test its operation as

¹For ALD dielectric thickness of 50 nm, dielectric constant of 10, terminal capacitor area of $250 \times 250 \mu\text{m}^2$ and vacuum permittivity of $8.9 \cdot 10^{-12}$ F/m, $C_t = 110$ pF.

5. Kinetic Inductance Traveling Wave Parametric Amplifier

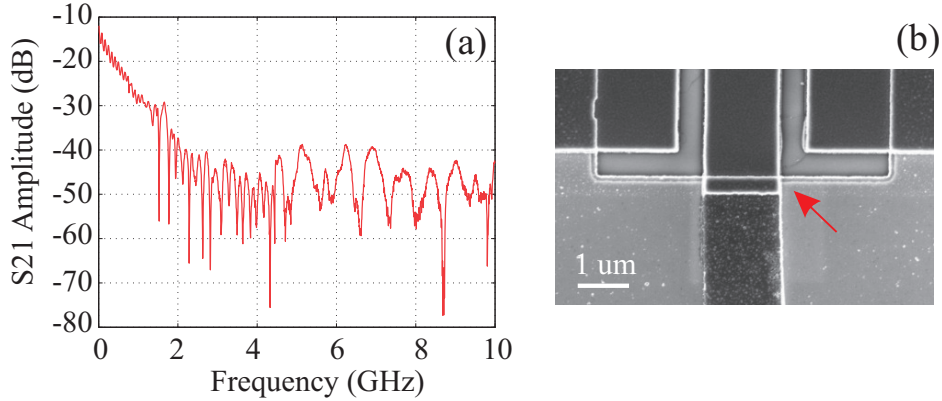


Figure 5.19: (a) S_{21} transmission for a ~ 10 cm long microstrip line. (b) Microstrip top conductor-to-CPW taper connection junction. The taper consists of Nb/Al/Al₂O₃/NbN/Al/Nb/NbN (100/10/12.8/20/20/100/10 nm) from bottom to top. The microstrip line consists of Nb/Al/Al₂O₃/NbN (100/10/12.8/20 nm) from bottom to top. T=2.3 K.

KI-TWPA. The S_{21} transmission spectrum is demonstrated in Fig. 5.19 (a). We observed a significant device attenuation (50 dB at 4 GHz), in spite of the fact that device was neither shorted, nor open circuit. We relate such attenuation to the CPW-microstrip coupling interface quality (Fig. 5.19 (b), the step is pointed with an arrow).

Our speculation regarding CPW-to-microstrip junction quality is supported by our experience with earlier microstrip designs. When we made a resonator with a Nb ground plane conductor thicker than NbN top conductor (Nb (100 nm), Al (10 nm), Al₂O₃ (10 nm), NbN (20 nm)), we observed that the external Q-factors and thus the resonator couplings were not reproducible. This issue was improved after switching to Nb, NbN with equal thicknesses - (Nb (50 nm), Al (10 nm), Al₂O₃ (55 nm), NbN (50 nm)). We attribute this to local defects in the area, where CPW line is converted into microstrip (Fig. 5.20 (a)). The large step in layer thicknesses could cause breaking of the superconducting strip or introduce shorts in the ALD oxide itself (Fig. 5.20 (b), pointed with red arrows). An ideal CPW-to-microstrip transition should contain no steps. A trick to improve this can be introducing a very narrow cut in the CPW central-to-ground gap (sketched in Fig. 5.20 (c)). The cut should be just narrow enough to be filled with the ALD oxide (~ 50 nm). The subsequent NbN layer will then be much smoother in the transition area. Note, that such a small cut will not induce much radiation in

5. Kinetic Inductance Traveling Wave Parametric Amplifier

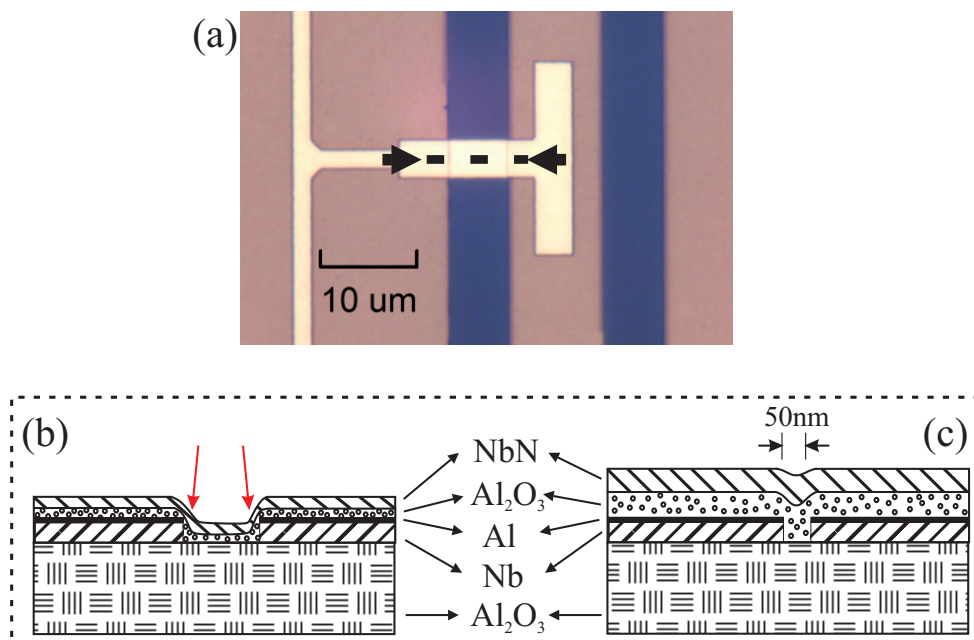


Figure 5.20: (a) Zoom-in on the microstrip-to-CPW coupling area. (b) Cross-section across the dashed line in (a). The gap between the CPW central line and the ground plane is filled with Nb (100 nm), Al (10 nm), Al_2O_3 (10 nm), NbN (20 nm). The red arrows point at the steps in the structure. (c) The cross-section of the CPW gap with 50 nm wide cut in Nb layer. Thicknesses of the layers are Nb (50 nm), Al (10 nm), Al_2O_3 (55 nm), NbN (50 nm). The surface of NbN is almost flat. Sketch is not to scale.

the ground plane conductor of the microstrip line. Thus, in the implementation of a microstrip-based KI-TWPA the major challenge remains the coupling of the microstrip top conductor to CPW tapers. Apart from the attenuation, there are also periodic ripples in the spectrum, as the line is not perfectly impedance matched with in/out tapers. These ripples can be easily eliminated by impedance matching the microstrip line to in/out terminal 50Ω impedances via tuning, for example, the oxide thickness. On top of ripples, there are non-periodic features, which we relate to coupling to spurious ground plane resonances. The elimination of ground plane resonance-caused spikes is a more serious issue and remains as an open question for future investigation.

5.12 Summary & Outlook

The purposed first ever tunable microstrip resonators provide a unique combination of substantial tunability range (3%), fast tuning time (3 ns) and high Q s on par (at single photon powers) or superior (with > 50 photons in the resonator) to the standard CPW/SQUID tunable design. Though there exist tunable resonators in literature with higher Q s, faster response and wider tuning range, none of them so far provides a balanced combination of all the parameters. While the reported Q s are already enough for many c-QED applications, we expect that the Q -factors can be further improved by switching to deposited thin film hydrogen rich amorphous silicon (a-Si:H) oxide with a reported loss tangent of $\sim 2 \cdot 10^{-5}$ (at low powers) [121]. Radiation losses can be reduced by introducing more effective superconducting filter after the terminal capacitors to isolate the microwaves.

Fractallizing the ground conductor of the microstrip resonator can make it resilient to 400 mT magnetic fields (Paper II). Moreover, it was demonstrated in a recent work in literature that a single 100 nm wide superconducting strip can tolerate parallel fields up to 6 T at 0.3 K [98]. We therefore propose that similar resilience should be achievable for a double strip (a signal strip on top of a ground strip) design. The disadvantage of a single strip design, reported in [98], is the excessive radiation losses (due to unbalanced dipole), which should be eliminated in a double strip design.

And last but not the least, the reported tunable microstrip resonators may potentially serve as a test-bed for a microstrip line to be implemented as the core element of KI-TWPA. We demonstrate that the tunable microstrip resonators have KI nonlinearity sufficient for parametric gain with a much more compact line as compared to standard CPW or even fractal-based designs. Our data suggest that the implementation of microstrip-based KI-TWPA should be feasible. However, many potential hindrances are standing on the way to reach this goal, such as coupling the line to in/out CPW terminals, decoupling from ground plane resonances and so forth.

5. Kinetic Inductance Traveling Wave Parametric Amplifier

Chapter 6

Conclusions

In c-QED and quantum computing experiments, quantum systems interact with microwaves that have a wavelength on the order of a centimeter. In this thesis, we have developed superconducting transmission lines with a microwave propagation velocity reduced by almost two orders of magnitude, as compared to propagation in vacuum. The corresponding wavelength is reduced accordingly, which makes it possible to build microwave elements (resonators, filters) much closer in size to active elements like transistors (few μm) and transmon qubits ($\sim 100 \mu\text{m}$). Particularly, we have presented how NSMM, ESR and KI-TWPA techniques benefit from design elements with reduced propagation velocity. With all the potentials reported in this thesis, slow propagation superconducting lines prove to be an important key on the way towards quantum technology.

Paper I: To make NSMM truly a non-invasive tool for interrogating quantum mechanical states of spurious (TLFs) and engineered (qubits) quantum systems, the NSMM should operate the microwave sensor close to the fundamental limit of single quanta of energy stored on average per cycle in the probe. As the microwave sensor for the microscope, we have developed a novel miniaturized resonator design based on a millimeter long slow propagation quasi-fractal line and we were able to place the resonator directly on a quartz tuning-fork. As a result, we reported NSMM operation with very low microwave probe powers, opening prospects for the coherent characterization of single TLF.

My contributions: AA participated in the development of fabrication process, helped with the fabrication and preparation of final samples. AA was involved in

6. Conclusions

the discussions of the results and in writing the manuscript.

Paper II: We have demonstrated that due to miniaturization the squeezed microwave mode volume of planar resonators favors the coupling of electromagnetic field to spins, thus enhancing the ESR sensitivity. However, to maintain a high quality factor, the planar resonator should be superconducting, while all previously known superconducting resonators failed to operate at high magnetic fields, needed to bring Zeeman spins in resonance with microwaves. We suggested a universal approach for reducing magnetic field induced losses in superconducting resonators by splitting microwave currents in between many parallel branches in a distributed thin film fractal network. The reported high-Qs at strong magnetic fields translate into high spin detection sensitivity. The possibility to study small number of spins opens out new horizons towards single spin ESR.

My contributions: AA contributed to sample fabrication and measurements. AA participated in the discussions of the results and in writing the manuscript.

Paper III: Working on NSMM and ESR projects, we realized that an ultimate sensitivity of a single spin/TLF can only be approached with a quantum-limited amplifier in the microwave readout. Inspired by a prototype KI-TWPA, based on a kinetic inductance nonlinearity intrinsic to a superconductor, earlier demonstrated by a group from Jet Propulsion Laboratory (JPL), we have entered the challenging race for the practical implementation of KI-TWPA. Our intention was to build a KI-TWPA based on a fractal slow propagation line to substantially reduce the length of the amplifier line. While working on this project, we have realized that the fractal design has stronger coupling to parasitic ground plane resonances due to its increased transverse dimensions as compared to a standard coplanar line. To cope with this problem, we have developed a custom multilayer fabrication technology, which allowed to combine high-KI (for an amplifier line) and non-KI elements (for the ground plane) in a single design. With non-KI ground plane, the spectral density of ground plane resonances was dramatically reduced. In a global context of microwave engineering, deploying KI as a design parameter opens a new design dimension and shall also favor the development of filters, diplexers etc.

My contributions: AA developed the fabrication process with some advice from SK and SdG and contributed to device design. AA fabricated the samples,

performed the measurements and analyzed the data with some assistance from AD. AA wrote the paper with support from AD.

Paper IV: In this paper, replacing the coplanar line in the original design from JPL with a slow propagation fractal line, we have succeeded in radically shortening the amplifier line from almost one meter (JPL) to ten centimeters. As a result, our amplifier is much less vulnerable to fabrication defects that were one of the factors limiting the gain in the original work by JPL. At the same time, increased line capacitance allowed for better impedance matching of the line, by compensating for its high kinetic inductance. The final amplifier demonstrated per unit length gain more than four times higher than ever reported, accelerating the progress of a practical KI-TWPA.

My contributions: AA developed the fabrication process with some advice from SK and SdG, contributed to device design and simulations. AA fabricated the samples, performed the measurements and analyzed the data with some assistance from AD. AA wrote the paper with support from AD.

Paper V: In parallel with fractal KI-TWPA, as a plan-B for the slow propagation line, we have explored a superconducting microstrip line. Instead of resorting to a fractal capacitor, we boost the per unit length capacitance by thinning down the dielectric layer in the microstrip. To keep the dissipation on par with coplanar line on silicon/sapphire substrates, we used ALD aluminum oxide as a thin film dielectric. We have shown that with a proper microstrip design and a perfected fabrication it is possible to reach high Q-factors, suggesting that the equivalent loss tangent of oxide material is good enough for building a parametric amplifier. To test the achievable kinetic inductance nonlinearity in the microstrip line for the implementation of KI-TWPA, we have produced a tunable microstrip resonator with a frequency controlled by a current bias and demonstrated a combination of high-Q, moderate tuning range and fast tuning time.

My contributions: AA developed the fabrication process with some advice from SK, contributed to device design. AA fabricated the final samples, performed the measurements and analyzed the data with some assistance from AD. AA wrote the paper with support from AD.

6. Conclusions

Appendix A

Derivation of inductively coupled resonant circuit parameters

In this appendix we will step-by-step derive the input impedance of an open-ended $\lambda/4$ resonator inductively coupled to a microwave feedline shown in Fig. 2.6 (a), its Q factors, as well as S_{21} transmission coefficient. The TL resonator behaves in this case as a series lumped-element circuit with an impedance defined in the following way[27]:

$$Z_r = R + j(\omega L - \frac{1}{\omega C}). \quad (\text{A.1})$$

At the resonance frequency the capacitive and inductive reactances balance out $\omega_0 L = 1/\omega_0 C$, and the resonant circuit impedance becomes purely real, thus we can introduce the resonance frequency and a characteristic impedance such as, $\omega_0 = \sqrt{1/LC}$, $Z_0 = \sqrt{L/C}$, then we can rewrite Z_r :

$$Z_r = R + j(\frac{\omega\omega_0 L}{\omega_0} - \frac{\omega_0}{\omega\omega_0 C}) = R + jZ_0(\frac{\omega}{\omega_0} - \frac{\omega_0}{\omega}). \quad (\text{A.2})$$

Inserting $Q_i = Z_0/R$, we will get:

$$Z_r = R(1 + jQ_i(\frac{\omega}{\omega_0} - \frac{\omega_0}{\omega})). \quad (\text{A.3})$$

We can make an approximation that $\omega = \omega_0 + \Delta\omega$, where $\Delta\omega/\omega_0$ is very small near the resonance frequency and $1/(1+x) = 1-x$ [122], thus

$$Z_r = R(1 + 2jQ_i\frac{\Delta\omega}{\omega_0}). \quad (\text{A.4})$$

A: Derivation of inductively coupled resonant circuit parameters

For the inductively coupled resonator circuit the input impedance will be [36]:

$$Z_{in} = j\omega L_0 + \frac{\omega^2 M^2}{Z_r}, \quad (\text{A.5})$$

where L_0 is the inductance of the coupling loop and M is the mutual inductance between the resonator coupling TL section and the TL. In this analysis, near resonance frequency the first term in Eq. (A.5) can be neglected, reducing it to

$$Z_{in} \approx \frac{\omega_0^2 M^2}{R(1 + 2jQ_i \frac{\Delta\omega}{\omega_0})}. \quad (\text{A.6})$$

At resonance frequency $\Delta\omega = 0$ and Eq. (A.6) will be simply $Z_{in} \approx \omega_0^2 M^2 / R = \omega_0^2 M^2 Q_i / Z_0$.

The ratio of internal to external Q-factors for a resonator coupled to the TL, is defined as:

$$\frac{Q_i}{Q_e} = \frac{P_e}{P_i} = \frac{V^2}{2I^2 R Z_0} = \frac{\omega_0^2 M^2}{2R Z_0}, \quad (\text{A.7})$$

with

$$Q_e = \frac{2LZ_0}{\omega_0 M^2}. \quad (\text{A.8})$$

In case of series impedance Z_{in} with TL Z_0 , S_{21} transmission coefficient is [37]

$$S_{21} = \frac{2}{2 + \frac{Z_{in}}{Z_0}}. \quad (\text{A.9})$$

After inserting Eq. (A.6) into (A.9) and rearranging [38],

$$S_{21} = \frac{S_{21,min} + 2jQ_{tot} \frac{\Delta\omega}{\omega_0}}{1 + 2jQ_{tot} \frac{\Delta\omega}{\omega_0}}, \quad (\text{A.10})$$

where Q_{tot} is the total (loaded) Q-factor, $S_{21} = S_{21,min}$ at $\omega = \omega_0$ and is defined as

$$S_{21,min} = \frac{Q_{tot}}{Q_i} = \frac{Q_e}{Q_i + Q_e}. \quad (\text{A.11})$$

Appendix B

Fabrication Recipes

Slow propagation lines for KI-TWPA

1) Initial patterning

- Clean the native oxide from 2" Si wafers in 2% HF bath for 30 s, rinse in water bath and blow dry.
- Immediately load the substrates into DCA metal sputter system (1144). In order to avoid flakes from the sputtering source, it's better to sputter right after the source has been cleaned. Sputter 80/20/100/10 nm of NbN/Al/Nb/NbN with rotating sample stage, base pressure below 2×10^{-8} Torr. The recipe must have the following parameters: target DC power: Nb/NbN 200 W, Al 50 W, Ar flow 60 sccm, N₂ flow 6.5 sccm, process pressure: NbN 6.7 microbar, Nb 8 microbar, Al 6.7 microbar, rates: Al 15 nm/min, NbN 27 nm/min, Nb 40 nm/min. Do sample stage cooling for all layers except the bottom NbN.
- Spin-coat resist UV5-0.8 4000 rpm for 1 min; softbake at 130 °C on hot plate for 2 min. Its preferable to clean the pipette with water/Isopropanol (IPA)/Acetone beforehand.
- Expose with e-beam system (100 kV, JEOL JBX-9300FS), 35 nA current. The pattern must be exposed with two different field lines, each with half a base dose, to avoid stitching errors. Postbake at 130 °C on hot plate for 1.30 min. Develop the resist with Microposit MF24A for 50 s and rinse with water.

B: Fabrication Recipes

- In the chamber 2 of plasma etch-RIE system (404), etch top Nb/NbN with NF_3 gas for ~ 50 s (50 sccm, radio frequency (RF) forward power 30 W, inductively coupled plasma (ICP) power 200 W). Follow the etching process with a laser interferometer to manually stop etching after the signal change on Al interface. Move the wafer to chamber 1 and etch Al with $\text{SiCl}_4/\text{Cl}_2/\text{Ar}$ gas mixture for ~ 50 s (10/10/10 sccm, RF power 60 W, ICP power 0 W) and then move back to chamber 2 to etch bottom NbN with NF_3 gas for ~ 50 s.
- Clean the resist in the Plasma BatchTop (419) with 100 W O_2 plasma (strip3m_a).

2) Removing of shorts

- Spin-coat resist ARP 6200.13 (Allresist GmbH) 4000 rpm for 1 min; soft-bake at 160°C on hot plate for 5 min. Do this twice to end up with 800 nm thick resist.
- Expose with e-beam system (100 kV, JEOL JBX-9300FS), 35 nA current using mark alignment. Develop the resist in Oxylene for ~ 1 min and dip in IPA, blow dry.
- In plasma etch-RIE system (404) run preconditioning recipe for chamber 2 (chamber pressure 80 mTorr, step1: O_2 - 50 sccm, RF forward power 100 W, ICP power 500 W, step2: CF_4/O_2 - 50/10 sccm, RF forward power 100 W, ICP power 700 W, step3: O_2 - 50 sccm, RF forward power 20 W, ICP power 500 W). Etch top Nb/NbN with CF_4/O_2 gas mixture for 1 min30 s (60/3 sccm, RF forward power 30 W, ICP power 200 W), track the etching with a laser interferometer and manually stop after reaching the Al interface. Move the wafer to chamber 1 and etch Al with $\text{SiCl}_4/\text{Cl}_2/\text{Ar}$ gas mixture for ~ 50 s (10/10/10 sccm, RF power 60 W, ICP power 0 W) and then move back to chamber 2 to etch bottom NbN with CF_4/O_2 gas mixture for 50 s.
- Clean the resist in the Plasma BatchTop (419) with 100 W O_2 plasma (strip3m_a). Do additional cleaning with 65°C mr-Rem 400 Remover (or 1165, MicropositTM Remover 1165, DOW chemical company) for 20 min.

3) Thinning down the central strip

- Spin-coat 400 nm thick resist ARP 6200.13 (Allresist GmbH) 4000 rpm for 1 min; softbake at 160°C on hot plate for 5 min.

- Expose with e-beam system (100 kV, JEOL JBX-9300FS), 35 nA current using mark alignment. Develop the resist in Oxylene for ~ 1 min and dip in IPA, blow dry.
- In plasma etch-RIE system (404) run preconditioning recipe for chamber 2. Etch top Nb/NbN with CF_4/O_2 gas mixture for 1 min30 s (60/3 sccm, RF forward power 30 W, ICP power 200 W), track the etching with a laser interferometer and manually stop after reaching the Al interface.
- Remove Al with MicropositTM MF319 Developer (DOW chemical company) for 2 min and then rinse the wafer in water, blow dry.
- Clean the resist in the Plasma BatchTop (419) with 100 W O_2 plasma (strip3m_a).
- On the wafer top-side spin-coat resist S1813 (Microresist GmbH) 3000 rpm for 1 min; softbake at 130°C on hot plate for 2 min. Dice the wafer into chips from top-side and clean the resist with 65°C mr-Rem 400 Remover (or 1165, MicropositTM Remover 1165, DOW chemical company) for 20 min or in Acetone, combined with 3 min of ultrasonic bath (50% power).
- Carefully inspect the whole chip under OM, and then in SEM for shorts. Remove the shorts with FIB/SEM system (DualBeam Versa (404)), ion beam current 7 pA, avoid exposing the sample to ion beam for a long time.

Microstrip Resonators

1) Alignment marks

- Spin-coat resist Copolymer MMA8.5EL10 3000 rpm (~ 450 nm) for 90 s on a 2" sapphire wafer; bake at 130°C on hot plate for 5 min.
- Spin-coat PMMA A2 (Microlithography Chemicals Corp. (MCC)) 3000 rpm (~ 70 nm) for 90 s; bake at 130°C on hot plate for 5 min.
- Evaporate 20 nm of Al.
- Expose with e-beam system (100 kV, JEOL JBX-9300FS), 35 nA current. Remove Al in a wet etch solution MF319 Developer (DOW chemical company) for 2 min and then rinse the wafer in water. Develop the resist with IPA:H₂O 10:1 mixture for ~ 110 s.
- Run ash10s in the Plasma BatchTop (419). Evaporate 10 nm Ti and 140 nm Au. Lift-off in a 65°C mr-Rem 400 Remover for 20 min.

B: Fabrication Recipes

2) Patterning of the ground plane

- Sputter 50/10 nm of Nb/Al in a DCA Metal system with rotating sample stage (base pressure below 2×10^{-8} Torr, Ar flow 60 sccm, target DC power Nb 200 W, Al 50 W, process pressure: Nb 8 microbar, Al 6.7 microbar, rates: Nb 50 nm/min, Al 15 nm/min). In between Nb and Al deposition turn the heater on. Start filling the chamber with O₂ and leave the sample to oxidize for 10 min at 170°C (pressure: > 4 Torr, rate: ~ 0.5 nm/min).
- Spin-coat resist UV5-0.8 (Microresist GmBH) 4000 rpm for 1 min; softbake at 130°C on hot plate for 2 min.
- Expose with e-beam system (100 kV, JEOL JBX-9300FS), 35 nA current using mark alignment. Right after exposure post-bake at 130°C on hot plate for 1.30 min. Develop the resist with Microposit MF24A for 45 s and rinse with water.
- Run O₂ ash10s in Plasma BatchTop (419) and in Plasma etch-RIE system (404) etch Al/Al₂O₃ with SiCl₄/Cl₂/Ar gas mixture for 1 m 40 s (10/10/10-sccm, RF power 80 W, ICP power 0 W, chamber pressure 3 mTorr) and then Nb with NF₃ gas for 1 m 10 s (50 sccm, RF power 30 W, ICP power 200 W, chamber pressure 20 mTorr).
- Clean the resist in the Plasma BatchTop (419) with O₂ strip3m_a and then with 65°C mr-Rem 400 Remover for 20 min.

3) Patterning of the top conductor

- Run O₂ ash7 process in Plasma BatchTop (419), 10 sccm, Power 50 W, Pressure 500 mT, 3 min.
- Deposit 50 nm of ALD Al₂O₃ (580 cycles, rate: $0.85 \text{ \AA}/\text{cycle}$, thermal oxide at 300°C, base pressure 10^{-6} mbar) in a preconditioned chamber (recipe 2:Al₂O₃ 300°C - thermal).
- Sputter 50 nm of NbN in a DCA Metal system with rotating sample stage at 200°C.
- Run O₂ ash7 process in Plasma BatchTop (419).
- Spin-coat resist maN2403 (Microresist GmBH) 1500 rpm for 1 min; soft-bake at 90°C on hot plate for 1 min.

- Expose with e-beam system (100 kV, JEOL JBX-9300FS), 35 nA current using mark alignment. The pattern must be converted in Beamer with multipass=2. Develop the resist with Microposit MFCD26 for 55 s and gently rinse with water.
- Etch NbN in Plasma etch-RIE system (404) in a preconditioned chamber (same as for KI-TWPA) with CF_4/O_2 mixture for 2 m 30 s (60/3 sccm, RF power 30 W, ICP power 200 W, chamber pressure 20 mTorr).
- Clean the resist in the Plasma BatchTop (419) with O_2 strip3m_a and then with 65°C mr-Rem 400 Remover for 20 min.
- On the wafer top-side spin-coat resist S1813 (Microresist GmBH) 3000 rpm for 1 min; softbake at 130°C on hot plate for 2 min. Dice the wafer into chips from the back-side and clean the resist in mr-Rem 400 Remover or in Acetone, combined with 3 min of sonication (50% power).

B: Fabrication Recipes

Appendix C

Calculation of kinetic to geometrical inductance ratio for KI-TWPA

To estimate how much L_k kinetic inductance of our line exceeds the L_m geometrical inductance, per unit length geometrical and total inductances are calculated for a $t = 80$ nm thick CPW line with central linewidth of $w = 1 \mu\text{m}$ and central-to-ground gaps of $g = 2 \mu\text{m}$. We choose a dielectric constant of sapphire $\varepsilon_r = 9.4$. First, similar to Ref. [123], the geometrical inductance for $t \leq g/2$ can be obtained:

$$L_m = \frac{\mu_0}{4F_0},$$
$$F_0 = \frac{K(k)}{K(k')} + p_{c0} * \left\{ \frac{t}{g} * (p_{c1} - \ln \frac{2t}{g}) + \left(\frac{t}{g}\right)^2 * \left(1 - \frac{3}{2}p_{c2} + p_{c2} * \ln \frac{2t}{g}\right) \right\}, \quad (\text{C.1})$$

where K is the complete elliptic integral, $k' = \sqrt{1 - k^2}$, $k = w/(w + 2g)$, $\mu_0 = 4\pi * 10^{-7}$ H/m is the vacuum permeability,

$$p_{c0} = \frac{b}{2aK(k')^2},$$
$$p_{c1} = 1 + \ln\left(\frac{8\pi a}{a+b}\right) + \frac{a}{a+b} \ln \frac{b}{a},$$
$$p_{c2} = p_{c1} - 2\frac{a}{b}(K(k')^2), \quad (\text{C.2})$$

C: Calculation of kinetic to geometrical inductance ratio

where $a = w/2$, $b = w/2 + g$. From this calculation, we get per unit length geometrical inductance of $L_m = 600$ nH/m.

The total per unit length inductance can be calculated for the same CPW line according to Ref. [124].

$$L_s = \frac{\pi\mu_0}{4f_1(\frac{2a}{\Lambda})},$$
$$f_1(u) = \int_0^\infty \frac{(1 - e^{-ux})}{x(x^2 + 1)} dx, \quad (\text{C.3})$$

where $u = 2a/\Lambda$, $\Lambda = 2\lambda_L^2/t$ is the Perl length and $\lambda_L = 490$ nm is the London penetration depth. The resulting total inductance is $L_s = 4.4$ $\mu\text{H}/\text{m}$. From the total per unit length inductance estimation of our fractal line, we have obtained $L_s = 7.3$ $\mu\text{H}/\text{m}$ in Paper IV, which is of the same order as the number calculated above. The ratio of total to geometrical inductance becomes $L_s/L_m \sim 7.4$ meaning that $L_k \approx 7L_m$.

Acknowledgements

The most important journey in my life is close to an end and the time has come to look at the past five years and give credit to all the co-passengers whose guidance helped me to achieve the most rewarding goal, a PhD.

First, I would like to express my deepest gratitude to my main supervisor Andrey Danilov for his endless patience and consistent support while guiding me through the hurdles of science. His wisdom, vast knowledge, and criticism have taught me invaluable lessons. Thank you, Andrey, for the unique experience. I want to extend my sincere appreciation to my examiner and co-supervisor Sergey Kubatkin. His optimism and unwavering zeal towards science were infectious, motivating me to try even the most risky experiments without hesitation. Thank you, Sergey, for being a great spiritual leader throughout these years. I'm grateful to my co-supervisor Sebastian de Graaf for sharing his knowledge and experimental skills with me. Thanks to him, I stopped being scared of tools and instruments, especially of the Maglab balloon. Also, I'm thankful to the members of our small group: Samuel, Hans, Kyung, Mohab, Tom, Arseniy, Maria and Karin, for making me feel as a part of the team.

Next, I would like to acknowledge the coordinator of the Marie Curie Initial Training Action Q-NET project, Hervé Courtois for organizing trainings, annual group meetings and amazing dinners. Also, I thank Prof. Khaled Karrai in AttoCube, Munich and the Pico group in Aalto University, Finland for hosting me with educational secondments. During these memorable events, I got to know many bright people from all around the world.

A big thank you to the best office mates: Lars, for the professional technical support, Reza, for our warm talks, and Marco, for the computer support and for that day when I was single-eyed and he carried my bag all the way from Grenoble

to Gothenburg. All the very best for your PhD, guys.

During my research, a considerable amount of time was spent fabricating samples and I'm grateful to the angels of the clean room: Bengt, Henrik, Mats, Ulf and the others, for recharging our energy drained by tool and process failures. My special thanks to Jan for keeping our Helium dewars full (also to all those people who gave a hand while transferring heavy dewars) and to Deborah, Maria, Marie, Susannah for expert administrative skills.

I thank the members of EMP group for all the scientific seminars, meetings, feedback, fruitful discussions and fika, specifically, Alexei, André, Arsalan, August, Bala, Ben, Dag, David, Floriana, Ida-Maria, Jonas, Leonid, Maria, Maxim, Michaël, Minshu, Niclas, Per, Philip, Pier Paolo, Riccardo, Saroj, Simon, Sophie, Thilo, Thomas, Tord and all others. Thank you, Alexey Pavolotsky, Parisa Aghdam and Vladimir Drakinsky for useful suggestions and technical support. I also thank Prof. Serge Charlebois from University of Sherbrooke, Canada for our collaboration.

Sometimes, lunch time was the only bright spot during the day. Thank you Sumedh, Tom, Maria Salatino and later, Angelo, Luca, Anna, Gunta, Yevgeniy for our lunch gatherings, when all the work related issues were vented out and it was very relieving (complaining helps a PhD student to stay sane!!!).

My special appreciation goes to Sebastian, Sumedh and Angelo for proofreading this thesis.

I owe a great deal of gratitude to all my friends who made Gothenburg feel like home away from home. Thank you, Sona, Rini, Nona, Vahag, Gayane, Eduar, Vard, Misak, Haykush, Yervand, Ulrika for the wonderful company. Warm thanks to my friends in Armenia for our fun times together: Sona, Arev, Anahit S., Anahit G., Ani, Lilit H., Satenik and SYL group.

I'm forever indebted to my family and relatives for their unconditional love, care and for 'keeping track' of my remaining time in PhD. Words can't sufficiently express how grateful I am to Ajay for his support and motivation. I have been lucky to have him by my side for always keeping me shining and moving forward.

Astghik Adamyan

Gothenburg, June 2016

Bibliography

- [1] R. P. Feynman. There's plenty of room at the bottom. *Journal of Microelectromechanical Systems.*, 1:60, 1992.
- [2] S. M. Lindsay. *Introduction to Nanoscience*. Oxford University Press, 2010.
- [3] L. van Hove. Von Neumann's contributions to quantum theory. *Bulletin of the American Mathematical Society*, 64:95, 1958.
- [4] G. Binnig, H. Rohrer, C. Gerber, and E. Weibel. Surface studies by scanning tunneling microscopy. *Physical Review Letters.*, 49:57, 1982.
- [5] G. Binnig, C. F. Quate, and C. Gerber. Atomic force microscope. *Physical Review Letters.*, 56:930, 1986.
- [6] M. A. McCord and M. J. Rooks. *Handbook of Microlithography, Micromachining and Microfabrication*. SPIE, 2000.
- [7] A. Wallraff and et al. Strong coupling of a single photon to a superconducting qubit using circuit quantum electrodynamics. *Nature.*, 431:162, 2004.
- [8] A. Blais, R-S. Huang, A. Wallraff, S. M. Girvin, and R. J. Schoelkopf. Cavity quantum electrodynamics for superconducting electrical circuits: An architecture for quantum computation. *Physical Review A.*, 69:062320, 2004.
- [9] D. I. Schuster, A. A. Houck, J. A. Schreier, A. Wallraff, J. M. Gambetta, A. Blais, L. Frunzio, J. Majer, B. Johnson, M. H. Devoret, S. M. Girvin, and R. J. Schoelkopf. Resolving photon number states in a superconducting circuit. *Nature.*, 445:515, 2007.
- [10] M. Göppl, A. Fragner, M. Baur, R. Bianchetti, S. Filipp, J. M. Fink, P. J. Leek, G. Puebla, L. Steffen, and A. Wallraff. Coplanar waveguide resonators for circuit quantum electrodynamics. *Journal of Applied Physics*, 104:113904, 2008.
- [11] M. Veldhorst, C. H. Yang, J. C. Hwang, W. Huang, J. P. Dehollain, J. T. Muhonen, S. Simmons, A. Laucht, F. E. Hudson, K. M. Itoh, A. Morello, and A. S. Dzurak. A two-qubit logic gate in silicon. *Nature*, 526:410, 2015.
- [12] D. J. Reilly, J. M. Taylor, J. R. Petta, C. M. Marcus, M. P. Hanson, and A. C. Gossard. Suppressing Spin Qubit Dephasing by Nuclear State Preparation. *Science*, 321:817, 2008.

BIBLIOGRAPHY

- [13] M. Mariantoni, H. Wang, T. Yamamoto, M. Neeley, C. B. Radoslaw, Y. Chen, M. Lenander, E. Lucero, A. D. O’Connell, D. Sank, M. Weides, J. Wenner, Y. Yin, J. Zhao, A. N. Korotkov, A. N. Cleland, and J. M. Martinis. Implementing the Quantum von Neumann Architecture with Superconducting Circuits. *Science*, 61:410, 2011.
- [14] Y. Nakamura, Y. A. Pashkin, and J. S. Tsai. Coherent control of macroscopic quantum states in a single-Cooper-pair box. *Nature.*, 398:786, 1999.
- [15] J. N. Eckstein and J. Levy. Materials issues for quantum computation. *MRS Bulletin.*, 38:783, 2013.
- [16] B. T. Rosner. High-frequency near-field microscopy. *Review of Scientific Instruments.*, 73:2505, 2002.
- [17] K. Saeedi and et al. Room-temperature quantum bit storage exceeding 39 minutes using ionized donors in silicon-28. *Science.*, 342:830, 2013.
- [18] Y. Kubo, F. R. Ong, P. Bertet, D. Vion, V. Jacques, D. Zheng, A. Dréau, J. F. Roch, A. Auffeves, F. Jelezko, J. Wrachtrup, M. F. Barthe, P. Bergonzo, and D. Esteve. Strong Coupling of a Spin Ensemble to a Superconducting Resonator. *Physical Review Letters*, 105:140502, 2010.
- [19] J. A. Weil and J. R. Bolton. *Electron Paramagnetic Resonance: Elementary Theory and practical applications*. Second Edition. Wiley, 2007.
- [20] Y. Twig, E. Dikarov, W. D. Hutchison, and A. Blank. High sensitivity pulsed electron spin resonance spectroscopy with induction detection. *Review of Scientific Instruments.*, 82:076105, 2011.
- [21] T. C. White, J. Y. Mutus, I. C. Hoi, R. Barends, B. Campbell, Y. Chen, Z. Chen, B. Chiaro, A. Dunsworth, E. Jeffrey, J. Kelly, A. Megrant, C. Neill, P. J. J. O’Malley, P. Roushan, D. Sank, A. Vainsencher, J. Wenner, S. Chaudhuri, J. Gao, and J. M. Martinis. Traveling wave parametric amplifier with Josephson junctions using minimal resonator phase matching. *Applied Physics Letters*, 106:242601, 2015.
- [22] R. Movshovich, B. Yurke, P. G. Kaminsky, A. D. Smith, A. H. Silver, R. W. Simon, and M. V. Schneider. Observation of Zero-Point Noise Squeezing via a Josephson-Parametric Amplifier. *Physical Review Letters*, 65:1419–1422, 1990.
- [23] R. W. Landauer. *Patent 3,111,628, United State Patent Office, N. Y.*, page 5, 1963.
- [24] H. B. Eom, P. K. Day, H. G. LeDuc, and J. Zmuidzinas. A wideband, low-noise superconducting amplifier with high dynamic range. *Nature Physics*, 8:623–627, 2012.
- [25] C. Bockstiegel, J. Gao, M. R. Vissers, M. Sandberg, S. Chaudhuri, A. Sanders, L. R. Vale, K. D. Irwin, and D. P. Pappas. Development of a Broadband NbTiN Traveling Wave Parametric Amplifier for MKID Readout. *Journal of Low Temperature Physics*, 176:476–482, 2014.
- [26] R. Collin. *Foundations for Microwave Engineering*. 2nd Edition. IEEE Press Classic Reissue, 2001.

BIBLIOGRAPHY

- [27] C. G. Montgomery, R. H. Dicke, and E. M. Purcell. *Principles of Microwave Circuits*. IET Electromagnetic Waves Series 25. McGraw-Hill Book Company, 1987.
- [28] Hernandez G. *Fabry-Perót Interferometers*. Cambridge University Press, 1986.
- [29] Wikipedia. <http://en.wikipedia.org/wiki/fabry>
- [30] Shive J. N. <https://www.youtube.com/watch?v=DovunOxlY1k>, 1959.
- [31] S. Gibilisco. *Teach Yourself Electricity and Electronics*. 5th Edition. McGraw-Hill Education, 2011.
- [32] B. Mazin. *Microwave Kinetic Inductance Detectors*. PhD Thesis, California Institute of Technology, 2004.
- [33] R. J. Schoelkopf and S. M. Girvin. Wiring up quantum systems. *Nature*, 451:664–9, 2008.
- [34] M. Sandberg. *Fast-tunable resonators and quantum electrical circuits*. PhD Thesis, Chalmers University of Technology, 2009.
- [35] D. I. Schuster, A. P. Sears, E. Ginossar, L. DiCarlo, L. Frunzio, J. J. L. Morton, H. Wu, G. A. D. Briggs, B. B. Buckley, D. D. Awschalom, and R. J. Schoelkopf. High-Cooperativity Coupling of Electron-Spin Ensembles to Superconducting Cavities. *Physical Review Letters*, 105:140501, 2010.
- [36] Banos A. RI Report No 630, Nov. 3, 1944.
- [37] D. M. Pozar. *Microwave Engineering*. 2nd Edition. John Wiley and Sons, Inc., 1998.
- [38] M. S. Khalil, M. J. A. Stoutimore, F. C. Wellstood, and K. D. Osborn. An analysis method for asymmetric resonator transmission applied to superconducting devices. *Journal of Applied Physics*, 111:054510, 2012.
- [39] R. Barends, H. L. Hortensius, T. Zijlstra, J. J. A. Baselmans, S. J. C. Yates, J. R. Gao, and T. M. Klapwijk. Noise in NbTiN, Al, and Ta Superconducting Resonators on Silicon and Sapphire Substrates. *IEEE Transactions on Applied Superconductivity*, 19:936, 2009.
- [40] Antenna Fundamentals. <http://www.cv.nrao.edu/course/ast534/antennatheory.html>.
- [41] W. D. Oliver and P. B. Welander. Materials in Superconducting Quantum Bits. *MRS Bulletin*, 38:816–25, 2013.
- [42] J. M. Martinis, K. B. Cooper, R. McDermott, M. Steffen, M. Ansmann, K. D. Osborn, K. Cicak, O. Seongshik, D. P. Pappas, R. W. Simmonds, and C. C. Yu. Decoherence in Josephson Qubits from Dielectric Loss. *Physical Review Letters*, 95:210503, 2005.
- [43] A. Bruno, G. de Lange, S. Asaad, K. L. van der Enden, N. K. Langford, and L. DiCarlo. Reducing intrinsic loss in superconducting resonators by surface treatment and deep etching of silicon substrates. *Applied Physics Letters*, 106:182601, 2015.
- [44] J. R. Waldram. *Superconductivity of metals and cuprates*. CRC Press, 1996.

BIBLIOGRAPHY

- [45] A. A. Abrikosov. The magnetic properties of superconducting alloys. *J. Phys. Chem. Solids.*, 2:199, 1957.
- [46] S. De Graaf. *Fractal superconducting resonators for the interrogation of two-level systems*. PhD Thesis, Chalmers University of Technology, 2014.
- [47] M. Tinkham. *Introduction to Superconductivity*. McGraw-Hill Book Co., 1996.
- [48] R. Córdoba, T. I. Baturina, J. A. Sesé, Y. Mironov, J. M. De Teresa, M. R. Ibarra, D. A. Nasimov, A. K. Gutakovskii, A. V. Latyshev, I. Guillamón, H. Suderow, S. Vieira, M. R. Baklanov, J. J. Palacios, and V. M. Vinokur. Magnetic field-induced dissipation-free state in superconducting nanostructures. *Nature Communications.*, 4:1, 2013.
- [49] G. Grimaldi, A. Leo, A. Nigro, A. V. Silhanek, N. Verellen, V. V. Moshchalkov, M. V. Milosević, A. Casaburi, R. Cristiano, and S. Pace. Controlling flux flow dissipation by changing flux pinning in superconducting films. *Applied Physics Letters.*, 100:202601, 2012.
- [50] D. I. Schuster. *Circuit Quantum Electrodynamics*. PhD Thesis, Yale University, 2007.
- [51] S. Doyle. *Lumped Element Kinetic Inductance Detectors*. PhD Thesis, University of Cardiff, 2008.
- [52] M. R. Vissers, J. Hubmayr, M. Sandberg, S. Chaudhuri, C. Bockstiegel, and J. Gao. Frequency-tunable superconducting resonators via nonlinear kinetic inductance. *Applied Physics Letters*, 107:062601, 2015.
- [53] D. C. Mattis and J. Bardeen. Theory of anomalous skin effect in normal and superconducting metals. *Physical Review.*, 111:412, 1958.
- [54] A. J. Annunziata, D. F. Santavicca, L. Frunzio, G. Catelani, M. J. Rooks, A. Frydman, and D. E. Prober. Tunable superconducting nanoinductors. *Nanotechnology.*, 21:445202, 2010.
- [55] S. K. Yip and J. A. Sauls. Nonlinear Meissner effect in CuO superconductors. *Physical Review Letters*, 69:2264, 1992.
- [56] A. J. Annunziata. *Single-Photon Detection, Kinetic Inductance, and Non-Equilibrium Dynamics in Niobium and Niobium Nitride Superconducting Nanowires*. PhD Thesis, Yale University, 2010.
- [57] M. W Pospieszalski. Extremely Low-Noise Amplification with Cryogenic FETs and HFETs: 1970-2004. *IEEE Microwave Magazine*, 3:62, 2005.
- [58] Zhi Tong, Carl Lundström, Peter A. Andrekson, Magnus Karlsson, and Adonis Bogris. Ultralow Noise, Broadband Phase-Sensitive Optical Amplifiers, and Their Applications. *IEEE Journal on Selected Topics in Quantum Electronics*, 18:1016–1032, 2012.
- [59] C. Lundström. *Phase-Sensitive Fiber Optic Parametric Amplifiers and Their Applications in Optical Communication*. PhD Thesis, Chalmers University of Technology, 2012.
- [60] G. P. Agrawal. *Nonlinear Fiber Optics, 4th Edition*. Academic Press, 2007.

- [61] J. Hansryd, P. A. Andrekson, M. Westlund, J. Li, and P. O. Hedekvist. Fiber-based optical parametric amplifiers and their applications. *IEEE Journal on Selected Topics in Quantum Electronics*, 8:506–520, 2002.
- [62] R. Stolen and J. Bjorkholm. Parametric amplification and frequency conversion in optical fibers. *IEEE Journal of Quantum Electronics*, 18:1062–1072, 1982.
- [63] W. H. Bragg and W. L. Bragg. The reflection of x-rays by crystals. *Proc. R. Soc. Lond.*, 88:428, 1913.
- [64] H. P. Myers. *Introductory Solid State Physics*. Taylor and Francis, 2002.
- [65] H. Kroemer. *Quantum Mechanics*. Prentice Hall, 1994.
- [66] R. L. Kronig and W. G. Penney. Quantum Mechanics of Electrons in Crystal Lattices. *Proc. R. Soc. Lond. A*, 130:499, 1931.
- [67] S. C. Barden, J. B. Williams, J. a. Arns, and W. S. Colburn. Tunable gratings: Imaging the universe in 3-d with volume-phase holographic gratings (review). *ASP Conference Series.*, 195:552, 2000.
- [68] P. Ferraro and G. D. Natale. On the possible use of optical fiber Bragg gratings as strain sensors for geodynamical monitoring. *Optics and Lasers in Engineering.*, 37:115, 2002.
- [69] J. R. Dunphy. US patent 5399854. Embedded optical sensor capable of strain and temperature measurement using a single diffraction grating., 1995.
- [70] A. Imtiaz and S. M. Anlage. A novel STM-assisted microware microscope with capacitance and loss imaging capability. *Ultramicroscopy.*, 94:209, 2003.
- [71] L. Liu, Y. J. Feng, L. Y. Wu, and P. H. Wu. Local microwave characterization of metal films using a scanning microwave near-field microscope. *Solid State Communications.*, 119:133, 2001.
- [72] C. Gao and X. D. Xiang. Quantitative microwave near-field microscopy of dielectric properties. *Review of Scientific Instruments.*, 69:3846, 1998.
- [73] S. V. Kalinin and A. Gruverman. *Scanning Probe Microscopy: Electrical and Electromechanical Phenomena at the Nanoscale*. Volume 1, pg. 207. Springer-Verlag, NY, 2007.
- [74] A. Imtiaz, S. M. Anlage, J. D. Barry, and J. Melngailis. Nanometer-scale material contrast imaging with a near-field microwave microscope. *Applied Physics Letters.*, 90:143106, 2007.
- [75] M. Tabib-Azar and Y. Wang. Design and Fabrication of Scanning Near-Field Microwave Probes Compatible With Atomic Force Microscopy to Image Embedded Nanostructures. *IEEE Trans. Microwave Theory Tech.*, 52:971, 2004.
- [76] F. J. Giessibl. Atomic resolution on Si (111)-(7x7) by noncontact atomic force microscopy with a force sensor based on a quartz tuning fork. *Applied Physics Letters*, 76:1470, 2000.

BIBLIOGRAPHY

- [77] S. E. de Graaf, A. V. Danilov, and S. E. Kubatkin. Coherent interaction with two-level fluctuators using near field scanning microwave microscopy. *Scientific Reports.*, 5:17176, 2015.
- [78] S. M. Anlage, B. J. Feenstra, and M. Tabib-Azar. *Near-field microwave microscopy of materials properties*. In Microwave Superconductivity (ed. by Weinstick, H. and Nisenoff, M.). Kluwer, Amsterdam, 2001.
- [79] W. Kundhikanjana, K. Lai, M. A. Kelly, and Z-X. Shen. Cryogenic microwave imaging of metal-insulator transition in doped silicon. *Review of Scientific Instruments.*, 82:033705, 2011.
- [80] H. Göttlich, R. W. Stark, J. D. Pedarnig, and W. M. Heckl. Noncontact scanning force microscopy based on a modified tuning fork sensor. *Review of Scientific Instruments.*, 71: 3104, 2000.
- [81] T. Lindström, J. Burnett, M. Oxborrow, and A. Y. Tzalenchuk. Pound-locking for characterization of superconducting microresonators. *Review of Scientific Instruments*, 82: 104706, 2011.
- [82] S. E. de Graaf, J. Leppakangas, A. Adamyan, A. V. Danilov, T. Lindström, M. Fogelström, T. Bauch, G. Johansson, and S. E. Kubatkin. Charge qubit coupled to an intense microwave electromagnetic field in a superconducting Nb device: evidence for photon-assisted quasiparticle tunneling. *Physical Review Letters*, 111:137002, 2013.
- [83] H. Wu and et al. Storage of multiple coherent microwave excitations in an electron spin ensemble. *Physical Review Letters.*, 105:140503, 2010.
- [84] M. R. Brustolon. *Electron Paramagnetic Resonance: A practitioner's toolkit*. IET Electromagnetic Waves Series 25. Wiley, 2009.
- [85] D. Bothner, T. Gaber, M. Kemmler, D. Koelle, R. Kleiner, S. Wunsch, and M. Siegel. Magnetic hysteresis effects in superconducting coplanar microwave resonators. *Physical Review B.*, 86:014517, 2012.
- [86] M. Devoret, S. Girvin, and R. Schoelkopf. Circuit-QED: how strong can the coupling between a Josephson junction atom and a transmission line resonator be?. *Ann. Phys.*, 16:767, 2007.
- [87] L. Shtirberg and et al. High-sensitivity Q-band electron spin resonance imaging system with submicron resolution. *Rev. Sci. Instrum.*, 82:043708, 2011.
- [88] K. Sandner and et al. Strong magnetic coupling of an inhomogeneous nitrogen-vacancy ensemble to a cavity. *Physical Review A.*, 85:053806, 2012.
- [89] X. Zhu and et al. Coherent coupling of a superconducting flux qubit to an electron spin ensemble in diamond. *Nature.*, 478:221, 2011.
- [90] I. Wisby and et al. Coupling of a locally implanted rare-earth ion ensemble to a superconducting microresonator. *Applied Physics Letters.*, 105:102601, 2014.

-
- [91] A. V. Kuznetsov, D. V. Eremenko, and V. N. Trofimov. Onset of flux penetration into a thin superconducting film strip. *Physical Review B*, 59:1507, 1999.
- [92] D. Bothner, T. Gaber, M. Kemmler, D. Koelle, and R. Kleiner. Improving the performance of superconducting microwave resonators in magnetic fields. *Applied Physics Letters*, 98:102504, 2011.
- [93] S. E. de Graaf, A. V. Danilov, and S. E. Kubatkin. Accurate Real-time monitoring of quality factor and center frequency of superconducting resonators. *IEEE Transactions on Applied Superconductivity*, 24:1500605, 2014.
- [94] G. F. Warrick, D. L. Greedon, M. Goryachev, K. Benmessai, and M. E. Tobar. Ultrasensitive microwave spectroscopy of paramagnetic impurities in sapphire crystals at millikelvin temperatures. *Physical Review B*, 88:224426, 2013.
- [95] J. He. *Electron Spin Resonance on Si/SiGe quantum dots*. PhD Thesis. Princeton University, 2012.
- [96] J. Clarke and F. K. Wilhelm. Superconducting quantum bits. *Nature*, 453:1031, 2008.
- [97] J. H. Quateman. *Physical Review B*, 34:1948, 1986.
- [98] N. Samkharadze, A. Brunoe, P. Scarlino, G. Zheng, D. P. DiVincenzo, L. DiCarlo, and L. M. K. Vanderspyren. *Physical Review Applied*, 5:044004, 2016.
- [99] W. H. Louisell, A. Yariv, and A. E. Siegman. Quantum Fluctuations and Noise in Parametric Processes. I. *Physical Review*, 124:1646, 1961.
- [100] R. Slavik and et al. All-optical phase and amplitude regenerator for next-generation telecommunications systems. *Nature Photonics.*, 4:690, 2010.
- [101] H. Zimmer. Parametric amplification of microwaves in superconducting josephson tunnel junctions. *Applied Physics Letters*, 10:193, 1967.
- [102] C. Macklin, K. O'Brien, D. Hover, M.E. Schwartz, V. Bolkovsky, X. Zhang, W. D. Oliver, and I. Siddiqi. A near-quantum-limited Josephson traveling-wave parametric amplifier. *Science*, 350:307, 2015.
- [103] O. Yaakobi, L. Friedland, C. Macklin, and I. Siddiqi. Parametric amplification in Josephson junction embedded transmission lines. *Physical Review B*, 87:144301, 2013.
- [104] J. Y. Mutus, T. C. White, R. Barends, Yu Chen, Z. Chen, B. Chiaro, A. Dunsworth, E. Jeffrey, J. Kelly, A. Megrant, C. Neill, P. J. J. O'Malley, P. Roushan, D. Sank, A. Vainsencher, J. Wenner, K. M. Sundqvist, A. N. Cleland, and J. M. Martinis. Strong environmental coupling in a Josephson parametric amplifier. *Applied Physics Letters*, 104:263513, 2014.
- [105] B. Yurke, M. L. Roukes, R. Movshovich, and A. N. Pargellis. A low-noise series-array Josephson junction parametric amplifier. *Applied Physics Letters*, 69:3078, 1996.
- [106] J. Gao, M. Vissers, M. Sandberg, S. Chaudhuri, C. Bockstiegel, C. Abeles, K. Irwin, and D. Pappas. Kinetic Inductance Traveling-wave Parametric Amplifier for Qubit and Detector Readout. (*Abstract Q38.00012*), *APS March Meeting*, page 1, 2014.

BIBLIOGRAPHY

- [107] M. Guilmain, F. Dellenbach, C. Nauenheim, D. Drouin, and S. Ecoffey. A damascene platform for controlled ultra-thin nanowire fabrication. *Nanotechnology*, 24:245305, 2013.
- [108] R. Landauer. Shock waves in nonlinear transmission lines and their effect on parametric amplification. *IBM Journal of Research and Development*, 4:391, 1960.
- [109] K. Ilin, D. Henrich, Y. Luck, Y. Liang, M. Siegel, and D. Y. Vodolazov. *Physical Review B*, 89:184511, 2014.
- [110] Golwala S. Instrumentation for CCAT, www.ccatobservatory.org, 2011.
- [111] P. K. Day, H. G. LeDuc, B. A. Mazin, A. Vayonakis, and J. Zmuidzinas. A broadband superconducting detector suitable for use in large arrays. *Nature*, 425:817, 2003.
- [112] A. B. Pippard. *Proc. R. Soc. A*, 191:370, 1947.
- [113] J. M. Pond, J. H. Claassen, and W. L. Carter. Kinetic Inductance microstrip delay lines. *IEEE Transactions on magnetics*, 23:903, 1987.
- [114] J. Zmuidzinas. *Annu. Rev. Condens. Matter Phys.*, 3:169, 2012.
- [115] B. A. Mazin, D. Sank, S. McHugh, E. A. Lucero, A. Merrill, J. Gao, D. Pappas, D. Moore, and J. Zmuidzinas. Thin film dielectric microstrip kinetic inductance detectors. *Applied Physics Letters*, 96:102504, 2010.
- [116] M. Pierre, I. M. Svensson, S. R. Sathyamoorthy, G. Johansson, and P. Delsing. *Applied Physics Letters*, 104:232604, 2014.
- [117] M. Sandberg, F. Persson, I. C. Hoi, C. M. Wilson, and P. Delsing. *Physica Scripta*, T137:014018, 2009.
- [118] Z. L. Wang, Y. P. Zhong, L. J. He, H. Wang, J. M. Martinis, and A. N. Cleland. *Applied Physics Letters*, 102:163503, 2013.
- [119] J. E. Healey, T. Lindström, M. S. Colclough, C. M. Muirhead, and A. Ya. Tzalenchuk. *Applied Physics Letters*, 93:043513, 2008.
- [120] J. Burnett, T. Lindström, M. Oxborrow, Y. Harada, Y. Sekine, P. Meeson, and A. Ya. Tzalenchuk. *Physical Review B*, 87:140501(R), 2013.
- [121] A. D. O'connell, M. Ansmann, R. C. Bialczak, M. Hofheinz, N. Katz, E. Lucero, C. McKenney, M. Neeley, H. Wang, E. M. Weig, A. N. Cleland, and J. M. Martinis. *Applied Physics Letters*, 92:112903, 2008.
- [122] D. Kajfez and P. Guillon. *Dielectric Resonators*. 2nd Edition. SciTech, 1998.
- [123] W. Heinrich. *IEEE Transactions on Microwave Theory and Techniques*, 41:45, 1993.
- [124] J. R. Clem. *Journal of Applied Physics*, 113:013910, 2013.